A Thesis Submitted for the Degree of PhD at the University of Warwick

Permanent WRAP URL:

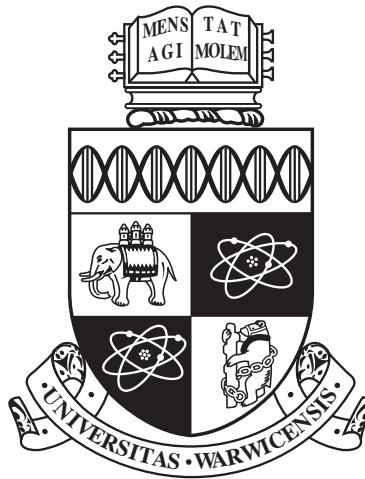**warwick.ac.uk/lib-publications**

Magnetic and thermal structuring and dynamics of solar coronal active regions

by

Chris Hornsey

Thesis

Submitted to the University of Warwick

for the degree of

Doctor of Philosophy

Physics Department

November 2015

THE UNIVERSITY OF
WARWICK

Contents

Acknowledgments

I would like to thank both my supervisors, Prof. Valery Nakariakov and Dr. Andrzej Fludra for their support and supervision throughout my PhD studies. Special thanks also goes to Dr. Thomas Wiegelmann and Dr. Adriaan Van Ballegooijen for use of their modelling software in chapters 5 and 6.

I would also like to thank my parents and my partner, Lucy, for their support and encouragement throughout my PhD.

This thesis was typeset with $\text{\LaTeX}\,2_\varepsilon$[1] by the author.

Declarations

This work is my own. It has been produce with the help of the following collaborations:

- Chapter 2. is an adaptation of Nakariakov et al. [2012], it was produced in collaboration with Prof. V Melnikov.

- Chapter 3. is an adaptation of Vasheghani Farahani et al. [2014], it was produced in collaboration with Dr. S Vasheghani Farahani, who developed the analytical approximation.

- The work in Chapters 4 and 5 was developed with the help of models developed by Dr. T Wiegelmann and Dr. A Van Ballegooijen

Abstract

This thesis is a study of the magnetic and thermal structuring and dynamics of the solar corona. The work presented here is primarily split into two sections: Initially a study of sausage oscillations of coronal structures in two geometries. Then the development of a static model of a coronal active region. Initially the basic concepts involved in studying the solar corona, in particular those relevant to this thesis, are introduced and explained.

In the second chapter sausage mode oscillations in a cylindrical geometry are studied in more detail. In particular a model of these oscillations is developed and used to study the behaviour of these oscillations over a wide range of wavelengths. The use of a wide range of wavelengths allows the resolution of a long-standing disagreement between results found in the long and short wavelength regions. The results of the model developed in chapter 2 are then compared with a novel analytical expansion of the dispersion relation. In chapter 3 the study is extended to the slab geometry, and this is compared to the results found in the cylindrical geometry.

The second section of work begins in chapter 4, we develop a model of a static active region, from magnetogram data taken by the Helioseismic and Magnetic Imager onboard the Solar Dynamics Observatory (SDO/HMI). This was done using a NLFF magnetic field extrapolation, and a 1-D hydrostatic model. The initial results of this modelling are also compared to EUV observations of these active regions. In chapter 5 the results and behaviour of this model is explored in more detail. In particular the behaviour of the hydrostatic model with a varying heating rate. Several individual loops are considered from the magnetic field model and studied in more depth. Various potential diagnostics for the coronal heating function are also considered.

Chapter 1

Introduction

1.1 Overview of the Sun

The Sun is the dominant body in our solar system. Its mass provides the central point about which, in the zeroth order approximation, the rest of the solar system orbits. It is also the essential source of energy in the solar system, this energy provides heat and light to its planets, including the Earth.

This energy is provided by an ongoing fusion process which occurs at the Sun's core. The fusion process is caused due to the intense temperatures and pressures forcing atomic nuclei together and releasing energy in the process. The transfer of the energy through the solar interior defines its structure.

The Sun's core extends to roughly 0.2 of the solar radius, R_s. The next $\sim 0.5R_s$ is known as the radiative zone. As the name suggests, the dominant energy transfer process in this region is radiation. However as the pressure in this region is still very large, individual photons are unable to travel very far before interacting with an electron and being re-emitted in another direction, leading to a lengthy "random walk" type process. This means it takes a very long time for an individual photon to traverse this region.

The boundary between the radiative zone and the convection zone, the outermost of the Sun's interior regions, is known as the tachocline. It is at this point that the Sun begins to rotate differentially; the core and radiative zones rotate as a solid body. This boundary is thought to be important in the generation of the solar magnetic field, acting as a dynamo.

Convection is the dominant energy transfer process in the convection zone, which makes up the remainder of the solar interior. Giant convective cells are formed in this region to transport the energy to the solar surface.

The visible surface is known as the photosphere, it is here that the vast majority of the Sun's visible light is emitted. Everything above the photosphere is generally considered to be the
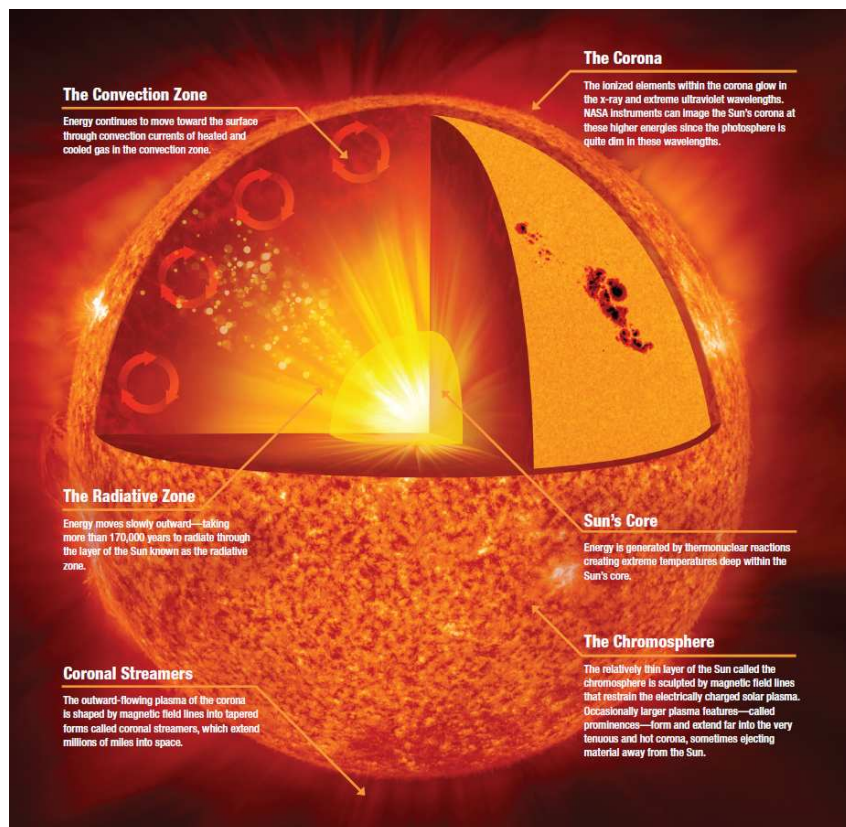
Figure 1.1: Schematic of the Sun, courtesy of NASA

solar atmosphere.

The lower part of the solar atmosphere is known as the chromosphere, and is characterised by a decrease in pressure, and increase in temperature. This leads to the transition region where there is a very rapid increase in temperature and decrease in pressure.

The corona makes up the bulk of the solar atmosphere, it is the region above the transition region. It is notable as it is significantly hotter than the underlying chromosphere and photosphere. The temperature varies from about 6000 K in the photosphere, before rising to $\sim$ 30000 K at the base of the transition region, followed by a rapid rise to $\sim$ 1 MK in the corona. The corona represents the main interest of this thesis, and as such will be discussed in much greater detail later.

The outermost layer of the solar atmosphere is the solar wind. This represents the stream of lower density plasma being emitted by the Sun in the radial direction. The exact mechanism by which it is driven is unknown, and represents one of the most important unanswered questions in solar physics.

1.2 Importance of solar physics

The Sun is essential to life on earth, and its study is very important. The Sun is crucial in several ways, most obviously that it provides the heat and light that make life on earth possible. Society has become ever more reliant on satellites for technology that is taken for granted everyday. These satellites exist in an environment that is very heavily controlled by the solar atmosphere.

Of particular risk are solar flares and coronal mass ejections (CMEs). As the name suggests these are an ejection of plasma and other accelerated particles from the corona. If this is directed towards the earth it can cause severe damage to satellite systems, and in extreme cases even damage electrical and pipeline systems on the earth's surface. An example of this is the 1859 Carrington event, a powerful solar flare directed towards Earth that damaged the few electrical systems across Europe and North America that existed at the time. They are considered to be of sufficient risk that the insurance underwriters Lloyds commissioned a report into the risks they posed [Hapgood and Thomson, 2010].

By studying solar physics, in particular the corona, we can gain a better understanding of the processes by which these events occur, and as such may be able to help predict them.
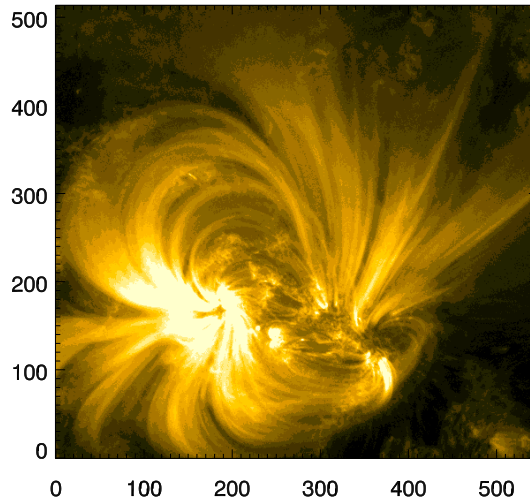
Figure 1.2: EUV image of a coronal active region captured by SDO/AIA in its 171 Å band. The active region is NOAA 11897 captured on 4th November 2013.

1.3 The corona

The corona was first observed during solar eclipses; it is not normally possible to observe it in the visible spectrum as the underlying photosphere is much brighter. However during an eclipse the moon blocks the light from the photosphere, leaving the more tenuous plasma of the corona visible (indeed this is how the corona was named from the Spanish word for "crown" as it gives the impression of a golden crown surrounding the moon).

When the corona was first studied it provided some confusion, as it is significantly hotter than the underlying photosphere. At first glance this does appear to be a very unusual result, and has led to one of the most important topics in solar physics: the coronal heating problem. The problem is essentially identifying the mechanism by which the corona is being heated. Over the years many theories have been suggested, and it remains a hot topic in solar physics to this day. [See Klimchuk, 2006; Walsh and Ireland, 2003; Narain and Ulmschneider, 1996, for reviews.]

As the corona was studied further, it was discovered that it is a highly structured environment. Fig. 1.2 shows an EUV image of the corona taken using the Atmospheric Imaging Assembly [Lemen et al., 2012] on board the Solar Dynamics Observatory; it is clear from images like this that the corona is dominated by brighter loop-like structures. These structures are caused by the relatively low magnetic field compared to the surround-

4

ing area, which combined with the low plasma β (which is the ratio of the gas and magnetic pressures in the plasma) keep the plasma confined to these structures. This causes the plasma's motion to be controlled by the variation of the magnetic field.

In terms of volume, however, these structures only take up a fraction of the corona. These regions are characterised by having "closed" magnetic fields, that is magnetic field lines which remain in the corona, as opposed to extending into the wider solar system. In these regions the magnetic field is closed to space on the outside, the magnetic field lines are instead connected to the photosphere at both ends. In the majority of the corona this is not the case, the magnetic field lines originate in the photosphere but extend off away from the Sun. These regions are know as the "open" corona, as the field lines here are open to outside. These regions are characterised by having a lower plasma density and it is therefore much more difficult to observe the processes which are occurring there.

These coronal loops appear so bright in the EUV images because the plasma they contain is denser than the surrounding corona. These structures contain the majority of the plasma in the corona, and are central to most of the processes occurring in the corona. Most of these structures are formed of loops of strong magnetic field which connect regions of opposite polarities. Their exact geometry is often very varied and has led to their sub-categorisation. A few of the more commonly observed structures are as follows:

Helmet streamers are large structures, the lower half of which consist of several large loops, and the upper half consists of a radially oriented stalk of plasma streaming outwards, giving the overall appearance of a helmet.

Coronal arcades occur where the regions of opposing polarity extend for a significant distance parallel to each other, this gives rise to a series of loops perpendicular to these regions of opposing polarity, but parallel to each other which often extending for a significant distance.

Sigmoids occur when the photospheric flows apply a shear to a dipole region, leading to a deformation of the coronal loops into large S-shapes.

Whilst not a static structure in the corona, solar flares and CMEs could both be considered to be important enough to be classified as coronal structures. Flares are a release of energy from an active region generally observed as a brightening of X-ray emission from the region. Flares are classified depending on the intensity of X-rays released, with X-class flares being the brightest. If a flare is of a significant magnitude it will sometimes have an associated CME; these CMEs involve large quantities of plasma being ejected from the corona at high velocity. However, the association of flares and CMEs remains a subject of intense debate.

There are many very important scientific questions regarding the corona that we do not fully understand. It is for this reason that studying the corona is vitally important. The following

is a list of some of these unanswered questions, as well as an explanation for their importance.

Firstly, as mentioned above arguably the most important unanswered question regarding the corona is the coronal heating problem. As previously stated the problem is essentially that the plasma in the corona is about three orders of magnitude hotter than that of the underlying photosphere, which appears to be somewhat counter-intuitive. Studies have considered the energy required to heat the corona to its observed temperatures [Withbroe and Noyes, 1977], have found that sufficient energy to heat the corona to the observed temperatures is being emitted from the photosphere; the problem is essentially the mechanism by which this energy is deposited in the corona. There are broadly two main groups of theories as to what this mechanism may be: AC or DC heating.

AC heating theories, as the name suggests, are those which suggest a heating rate that is variable over observed time-scales. These generally involve using waves generated in the photosphere and chromosphere travelling up towards the corona before interacting with the dense structures in the corona and depositing their energy in these structures. Some examples of AC heating mechanisms are described in: Hollweg [1987]; Ofman et al. [1995]; Inverarity and Priest [1995].

DC heating mechanisms are those which imply a heating rate which is either constant in time or varies on a time-scale much shorter than the conductive or radiative time-scales of the loops, thus the heating rate could be considered constant. The classic example of a DC heating rate is Parker's nanoflare theory [Parker, 1983, 1988]. This theory states that the constant motion of the photosphere causes the field lines to become braided, and eventually so tangled that they untangle themselves through a process known as magnetic reconnection. This magnetic reconnection process involves breaking old field lines and forming new ones, as well as releasing some of the energy stored in the field.

Some evidence for the nanoflares theory is provided by considering statistics of observed flares. These small scale heating events are known as nanoflares, as they are thought to operate on broadly the same principle as the flares observed in the solar corona. If the statistics for the observed flares are studied [Hudson, 1991] there is a power law relationship between the amount of energy released and the frequency of flares of this strength; that is to say that less powerful flares are much more common than more powerful ones. Naturally there is a threshold flare magnitude below which observations are unable to distinguish between the background solar emission, however it is reasonable to assume that these small scale flares occur even if they are unable to be detected and can be considered to be Parker's nanoflares. The total energy released by these nanoflares is simply the product of the magnitude of the events and their frequency, both of which could be extrapolated from the observed flare statistics [Drake, 1971; Shimizu, 1995; Veronig et al., 2002; Yashiro et al., 2006]. Unfor-
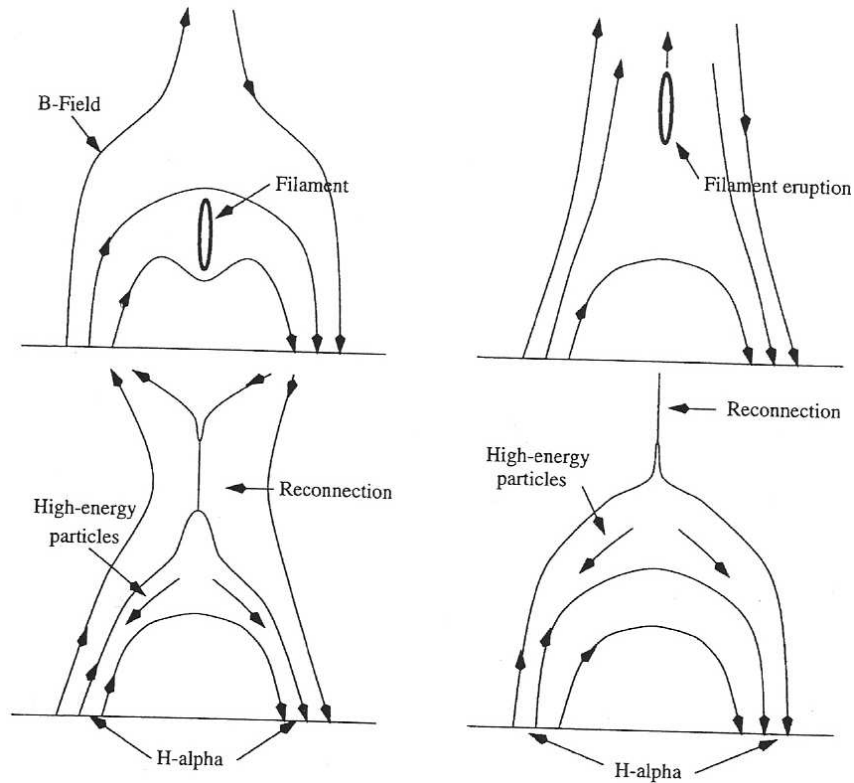
Figure 1.3: Diagram showing the various stages of the standard flare model. (From the University of Warwick PX420 Solar MHD lecture notes)

tunately there is not a consensus in the solar physics community as to whether or not this would provide sufficient energy to heat the corona to the observed temperatures, however it does not rule it out as a possibility either.

As previously mentioned flares could be considered to be more directly relevant to society than any other topic of research in the corona, as they have the potential to cause significant damage to both satellites in orbit around earth, as well as potentially damaging electronics on the earth's surface. As such the prediction of these events is a hugely important area of research, as well as understanding the process by which they occur and are triggered. There are many different flare models that have been proposed to explain these phenomena. However there is a model which is generally accepted as a good theoretical basis from which to start understanding the process by which flares occur. It is based on the work by Carmichael [1964]; Sturrock [1966]; Hirayama [1974]; Kopp and Pneuman [1976], and as such it is known as the CSHKP model, or it has also become known as the standard flare model.

Fig. 1.3 shows the stages through which a flare occurs. Initially a cool, dense filament is suspended above a magnetic neutral line by the coronal magnetic field. Magnetic energy builds up in this coronal field until it becomes unstable and erupts, launching the filament out of the corona, and opening the magnetic field lines which were suspending the filament upwards. As the magnetic field lines are stretched and brought together beneath the filament they undergo a process known as magnetic reconnection. This essentially causes the magnetic field lines to break and re-form as well as releasing a lot of energy. This energy is produced in the form of direct heating of the plasma in the reconnection site, causing soft X-ray emission. The heat is spread along the magnetic field lines due to thermal conduction, and the acceleration of nonthermal particles that also follow the field lines. The nonthermal particles going downward precipitate at the chromosphere producing the hard X-ray emission at the magnetic field lines' footpoints. The chromospheric heating causes the chromospheric plasma to evaporate up into the corona. This forms the hot, dense loops that are observed as flaring loops.

When dealing with the corona and its associated structures, it is useful to have a concept of some of the typical parameters involved. The plasma in the coronal portion of loops has a temperature of generally around 1 MK, but potentially varies up to 30 MK in flaring loops, with electron densities of roughly $10^8 - 10^{11}$ cm^{-3}. The length scale of these structures can also vary quite wildly, from tens of Mm up to hundreds. Some typical parameters in regions of open field lines are temperatures varying up to 1 MK, and electron densities varying from $\sim 10^9$ cm^{-3} in the lower corona to $\sim 10^6$ cm^{-3} in the upper corona.

1.4 Theoretical tools used in studying the corona

1.4.1 Magnetohydrodynamics

In order to model the processes and structures within the corona it is necessary to have a model to describe the behaviour of the plasma. The most suitable description of large-scale long-durational processes in fully ionised plasmas is magnetohydrodynamics (MHD). This plasma model essentially just treats the plasma as a fluid that interacts with (and is interacted by) the underlying and self-induced magnetic field. The underlying equations were developed as a combination of fluid dynamics equations and Maxwell's laws.

The derivation of the MHD equations makes several assumptions about the plasma, and as such means that MHD is only applicable under certain conditions; fortunately these conditions are almost always satisfied for the physical processes discussed in this thesis.

Firstly it is required for the characteristic time-scale for processes described to be much larger than both the ion gyro-period (that is the time it takes for an ion to orbit a magnetic

field line), and the inverse of the collision frequency (the mean time a particle travels between interacting with other particles).

Secondly the characteristic length scale described must be much longer than both the ion Larmor (that is the radius of the orbit an ion follows around a magnetic field line), and the mean free path distance (the mean distance a particle in the plasma travels between interacting with another particle). This combined with the first set of criteria essentially say that MHD is only suitable to describe processes in which the plasma can be treated as a fluid and no small scale plasma processes are taken into account.

Finally it is also required that particles are not travelling at relativistic velocities, as this is a non-relativistic theory. The basic MHD equations are as follows:

$$\frac{\partial \rho}{\partial t} + \nabla \cdot (\rho \mathbf{V}) = 0, \tag{1.1}$$

$$\rho \left[\frac{\partial \mathbf{V}}{\partial t} + (\mathbf{V} \cdot \nabla) \mathbf{V} \right] = -\nabla p + \mathbf{j} \times \mathbf{B}, \tag{1.2}$$

$$\frac{d}{dt} \left(\frac{p}{\rho^\gamma} \right) = 0, \tag{1.3}$$

$$\frac{\partial \mathbf{B}}{\partial t} = \nabla \times (\mathbf{V} \times \mathbf{B}), \tag{1.4}$$

$$\mathbf{j} = \frac{1}{\mu_0} \nabla \times \mathbf{B}, \tag{1.5}$$

$$\nabla \cdot \mathbf{B} = 0, \tag{1.6}$$

where, ρ is the plasma density, $\mathbf{V}$ is the fluid velocity, P is the plasma pressure, $\mathbf{j}$ is the current density, and $\mathbf{B}$ is the magnetic field. (1.1) is the condition of mass continuity, this ensures that no mass is created or destroyed in the model. (1.2) is the equation of motion from fluid mechanics, with an additional term on the RHS indicating the force exerted on the plasma by the magnetic field. Note that a term for gravitational force could be included on the RHS of this equation, however for most studies the gravitational force is much weaker than the others and as such is neglected. (1.3) is the energy equation; there are many ways of expressing this, the form shown is the simplest describing adiabatic processes. The parameter γ is the ratio of specific heats, and is generally simplified to $5/3$. (1.4) is the induction equation, describing how the magnetic field is affected by the motion of the plasma. (1.5) provides a definition for the current density, and is necessary for the equation of motion, which is required to close the set of equations. The parameter μ_0 is the permeability of free space. Finally, (1.6) is the solenoidal constraint, which ensures that there are no magnetic charges.

1.4.2   Magnetohydrostatics

Whilst the corona is in many senses dominated by very dynamic events, such as flares and CMEs, the majority of the corona is fairly static most of the time. As such many attempts to use static models to model coronal plasma have been made; these models are described as magnetohydrostatic.

The simplest static model that could be employed is simply to consider the corona as a gravitationally stratified atmosphere, in this case the pressure has a nearly exponential form:

$$p(h) = p_0 \exp\left(-\frac{h}{\lambda_p(T_e)(1 + \frac{h}{R_s})}\right), \tag{1.7}$$

where λ_p is the pressure scale height, it is defined as:

$$\lambda_p(T_e) = \frac{2k_B}{\mu m_H g_\odot} T_e. \tag{1.8}$$

Here, the distance is measured as h, the height above the photosphere. p_0 is the pressure at the photosphere, μ is the average molecular mass in the corona, $g_\odot$ is solar gravitational constant, R_s is the solar radius, k_B is Boltzmann's constant, m_H is the mass of a hydrogen nucleus, T_e is the electron temperature of the plasma.

This model is not specific for the corona. In order to use this model to study the corona, its implementation must be considered. A method of doing this is to treat the corona as a series of isothermal, but thermally isolated atmospheres all packed together. This is a reasonable model, as the plasma β in the corona is small, and as such magnetic forces dominate; moreover, in the absence of electrical resistivity, the plasma is "frozen in" to the magnetic field. As individual plasma ions can be thought of as staying restricted to their own field line, the thermal conductivity along any field line is high, but between field lines is low. This keeps the plasma on a field line all the same temperature, but each field line is thermally isolated from the others. If the coronal magnetic field is treated as being purely radial this gives a series of atmospheres, the pressure of which are all described by (1.7), but they will have differing values of λ_p, as they are all at different temperatures. It is then possible to model the emission from this plasma, and compare it to observations of the corona. Such a study was performed using Yohkoh/SXT soft X-ray data by Aschwanden and Acton [2001], and they found an empirical model for the temperature distribution that provided a good match to the quiet corona.

A similar approach can also be used to model more complex coronal structures, typically loops. A classic example of a hydrostatic loop model was developed by Rosner et al. [1978].

The basis for this model is the energy balance equation:

$$E_H + \mathbf{f} \cdot \mathbf{v} = \nabla \cdot \mathbf{F_c} - E_R + \nabla \left(\left(\frac{1}{2}\rho v^2 + U \right) \mathbf{v} + \rho \mathbf{v} \right), \qquad (1.9)$$

where E_H is the local heating rate, $\mathbf{f}$ is the total external force exerted on the plasma, mainly gravity, $\mathbf{v}$ is the plasma velocity, $\mathbf{F_c}$ is the energy flux due to thermal conduction [Spitzer, 1962], E_R is the energy lost due to radiation, ρ is the plasma density and U is the plasma thermal energy density. This equation describes all of the energy gains and losses at any point in the loop. In order for (1.9) to be any use in modelling a loop it must be integrated over the entire loop. Doing so gives:

$$\int_V (E_H + \mathbf{f} \cdot \mathbf{v}) d^3 r = - \int_V E_R d^3 r + L_{\text{footpoints}} + L_{\text{sides}}, \qquad (1.10)$$

where $L_{\text{footpoints}}$ and L_{sides} are the energy losses and gains across the footpoints or sides of the loop respectively. (1.10) therefore simply states that throughout the entire loop any heating applied and energy deposited by external forces must be balanced by radiation or the energy lost through the boundaries of the loop. This can then be further simplified by assuming that there is no energy transport through the sides of the loop, this is reasonable because, as before, the loop is thermally isolated from the rest of the corona. In addition, one can assume that the plasma is static. This just leaves the heating being balanced by radiation and energy transported through the footpoints.

As previously stated the coronal heating problem is a major topic of interest in the solar physics community, with many different heating mechanisms having been proposed. Each of these heating mechanisms implies a description of E_H, the heating rate. It is therefore not easy to find a definition for E_H from any theoretical basis. In order to progress with the analysis Rosner et al. [1978] simply assumed a constant E_H.

Next Rosner et al. [1978] modelled half of the loop, from footpoint to apex, and assumed it was symmetric. Then by considering the conductive flux at every point along the loop, with the boundary conditions that the flux disappears at the apex, and prescribing a photospheric temperature, Rosner et al. [1978] were able to obtain scaling laws relating the peak temperature, length, base pressure and heating rate:

$$T_{\text{max}} \sim 1400(p_0 L)^{\frac{1}{3}} \quad , \qquad (1.11)$$

$$E_{H0} = 0.95 \times 10^{-6} T_{\text{max}}^{\frac{7}{2}} L^{-2}, \qquad (1.12)$$

these are known as the RTV scaling laws. The loop's length and peak temperature can be estimated by observations, which would then allow an estimate to be made of the heating

rate and base pressure, which is assumed to be constant for the entire loop in this model. These laws do agree to some extent with observations of shorter soft X-ray loops, no doubt because the pressure is roughly constant in these shorter loops. Unfortunately when the scaling laws are applied to observations of longer EUV loops, such as those observed by the 171Å bandpass of SDO/AIA, it was found that the observed pressures at the apex of the loops were much higher than those derived with the use of the RTV scaling laws [Aschwanden et al., 2000].

It is therefore clear that the assumptions made by Rosner et al. [1978] are too restrictive to properly describe most loops in the corona, as such some of these assumptions must be relaxed. The most obvious starting point is to soften their assumption of a spatial uniform heating rate, E_H; whilst a spatial uniform heating rate does make performing the analysis to reach the scaling laws easier, it is not representative of the heating in the corona. An attempt to relax this assumption was performed by Serio et al. [1981], in their work they considered a heating rate of the form:

$$E_H = E_{H0} \exp\left(-\left(\frac{S}{S_H}\right)\right),$$
(1.13)

an exponential heating function, where E_{H0} is the heating rate at the base of the loop, S_H is the heating scale height and S is the distance along the loop. As with the derivation of the RTV scaling laws, it is assumed that the loop is symmetric, and only half of the loop is modelled at a time. Serio et al. [1981] also lifted the restriction of constant pressure along the loop. This led to a generalised version of the RTV scaling laws, introducing a factor that depended on the heating and pressure scale heights, S_H and λ_p. The updated scaling laws were found to be a more accurate model of observed EUV loops by Aschwanden et al. [2000].

An interesting consequence of this exponential heating rate proposed by Serio et al. [1981] is that as the heating scale height decreases, that is the heating becomes more focused in the footpoints of the loops, the location along the loop where the temperature is a maximum can move away from the apex of the loop. On the face of it this is perhaps not a surprising result: as less and less heating occurs at the apex of the loop, eventually a point further down the loop where more heating occurs will become hotter, assuming that any changes in the density profile are driven by varying the heating rate. The consequence of this is that loops where the peak temperature is not at the apex are unstable. This is due to the density of the plasma above the point of maximum temperature, (which is no longer the loop apex), becoming larger than the density of the plasma directly beneath it, which leads to the Rayleigh-Taylor instability. This gives the situation where the static loop model predicts that the loop cannot be static with the provided parameters. This instability was

studied by Winebarger et al. [2003].

More recent studies have extended this approach further and have been able to numerically solve the energy equation for an arbitrary heating rate, assuming a static solution exists. An example of this was made by Schrijver and van Ballegooijen [2005], which will be considered in more depth in chapter 5.

1.4.3 Modelling coronal magnetic fields

It is clear from observations that the magnetic field plays a large role in shaping the corona, and it is clear from the MHD equations that any attempt to mathematically model the corona will have to take into consideration the coronal magnetic field. Hence it would be very useful to have an understanding of the coronal magnetic field before any modelling is attempted. Unfortunately, whilst it is possible to measure the magnetic field strength in the photosphere by using Zeeman splitting of magnetically sensitive spectral lines, e.g. Fei 6173.3 Å as used by SDO/HMI [Scherrer et al., 2012], this technique does not, however, work in the corona. This is because these coronal emission lines are optically thin, thus it is not possible to know exactly where along the line-of-sight the measurement is taking place, as well as essentially having measurements from all points along the line-of-sight. Moreover, the lines experience huge nonthermal broadening which makes the Zeeman splitting unresolvable. One possible method to estimate the coronal magnetic field is to use the observed photospheric field as a boundary condition.

This leaves the problem set up essentially as follows: the magnetic field in the photosphere is known, and the magnetic field of the corona, (radially outwards from this boundary) is what is it be estimated. Using Maxwell's laws it is clear that this is insufficient information to find a solution for the coronal magnetic field, thus some assumptions must be made. The main assumption is that the corona is force-free, what this means is that the plasma in the corona is static and effectively feels no force. Consider (1.2); as previously stated the magnetic field is the most important parameter here and it only occurs in one term: $\mathbf{j} \times \mathbf{B}$, so let us consider the size of the other terms relative to this: if the pressure varies very little over the area considered then the ∇P term can be neglected. The velocity terms on the LHS can also be neglected, as considering typical coronal values for the parameters these terms are expected to be small compared to the $\mathbf{j} \times \mathbf{B}$ term. This just leaves:

$$\mathbf{j} \times \mathbf{B} = 0, \tag{1.14}$$

now, using the definition of the current density (1.5):

$$\frac{1}{\mu_0} \left(\nabla \times \mathbf{B} \right) \times \mathbf{B} = 0. \tag{1.15}$$
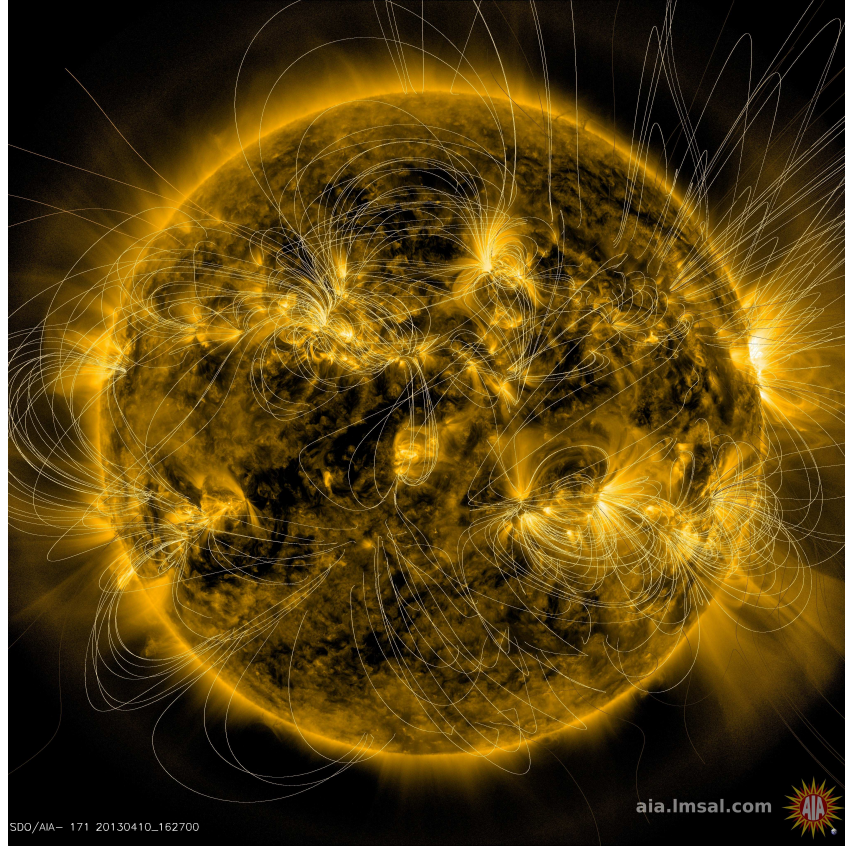
Figure 1.4: EUV image of the entire corona captured by SDO/AIA in its 171 Å band, with magnetic field lines calculated using a PFSS model overlayed. Image courtesy of NASA.

For this equation to hold $\nabla \times \mathbf{B}$ must be parallel to $\mathbf{B}$, that is to say:

$$\nabla \times \mathbf{B} = \alpha \mathbf{B}, \tag{1.16}$$

where α is an arbitrary constant. There are a few situations implied by this. Firstly $\alpha = 0$, in which case $\nabla \times \mathbf{B} = 0$, this implies that the magnetic field is potential. This is obviously the simplest scenario that provides a solution to (1.14), and as such is the easiest and fastest to compute. However this magnetic field arrangement is the most energetically efficient arrangement for the given boundary conditions, and as such it has no magnetic free energy to release. As all coronal heating theories involve the release of magnetic free energy from the coronal field, a potential field can obviously not be a completely accurate representation of the field.

Potential fields are however still widely used and provide a reasonable estimate for the topology of the field. They are for instance used in potential field source surface mod-

els (PFSS) whereby the coronal magnetic field is assumed to be completely radial above a certain height, providing an upper and lower boundary condition for the magnetic field [Schrijver and De Rosa, 2003]. These models can then be used to calculate the magnetic field in the Sun's entire corona see Fig. 1.4 for an example, also [Schrijver et al., 2004] for an example use of this kind of extrapolation.

A more complex type of force-free field to consider is one where α is a constant across the entire modelled region. This is known as a linear force-free field. It has the advantage over the potential field in that the field does contain some magnetic free energy, as well as being just as easy to compute, assuming the value of α is chosen. The problem is that it is not easy to determine the appropriate value of α, and as such it is generally not that much more useful than a potential field.

The remaining case is one in which α is only constant along any given field line, but is free to vary across fieldlines. This is known as a non-linear force-free field (NLFF field). NLFF fields can hold sufficient magnetic free energy [Gary et al., 1987], and are unique for a full set of vector magnetic field boundary conditions. As such they are very promising, however there are several issues that make determining them a challenge. Firstly they have a more stringent requirement on boundary conditions than potential fields. In order to uniquely determine an NLFF field, all three components of the magnetic field are required on the boundary, whereas potential fields only require a single component. These boundary conditions are required on all boundaries of the modelled region, which can also provide an obstacle, however there are methods to get around this, which will be discussed in more detail in chapter 5.

Even with all the required boundary conditions, whilst an NLFF field is uniquely determined, due to the non-linear nature of 1.14, it is not possible to analytically deduce the field from the boundary condition, hence some sort of iterative approach is required. There are several methods that have been suggested to calculate NLFF fields, Schrijver et al. [2006]; Metcalf et al. [2008] tested a variety of methods on both an established test field [Low and Lou, 1990] and a solar-like reference model [van Ballegooijen, 2004]

1.5 Coronal seismology

Coronal seismology is a relatively recent field of solar physics, which involves studying MHD oscillations in the corona, and using the parameters of these oscillations to deduce information about the structure of the corona [see De Moortel and Nakariakov, 2012; Banerjee et al., 2007; Nakariakov and Verwichte, 2005, for reviews].

Many oscillations have been observed in the corona e.g. Thompson et al. [1998]; Ofman et al. [1997]; De Moortel et al. [2000]. The most common type of oscillation observed

in EUV images, such as those from the Atmospheric Imaging Assembly (AIA) on board the Solar Dynamics Observatory (SDO), are transverse loop oscillations, e.g. Nakariakov et al. [1999]; White et al. [2012]. These generally occur when an impulsive event such as a flare occurs close to a loop or bundle of loops, which offsets the loop causing it to oscillate around its initial position. However many other types of oscillations have also been observed, such as quasi-periodic pulsations (QPPs) during flares, which will be described in more detail later on.

1.5.1 MHD oscillation theory

The theory behind coronal seismology is deeply rooted in MHD. First consider an equilibrium static uniform plasma; this gives the equilibrium conditions about which oscillations will take place, the equilibrium parameters are denoted by a subscript 0. They are: P_0, ρ_0, $\mathbf{B_0}$ and $\mathbf{V_0} = 0$, as we ignore equilibrium flows. It is clear that this equilibrium satisfies the MHD equations (1.1-1.6). To this equilibrium small perturbations are made, which are denoted by a subscript 1. This gives the following perturbed quantities:

$$P = P_0 + P_1(x, y, z, t),$$
$$\rho = \rho_0 + \rho_1(x, y, z, t),$$
$$\mathbf{B} = \mathbf{B_0} + \mathbf{B_1}(x, y, z, t),$$
$$\mathbf{V} = \mathbf{V_1}(x, y, z, t).$$

We then put these quantities into the MHD equations and discard all terms smaller than first order in terms of perturbed quantities. It is also assumed that any derivatives of equilibrium quantities are zero.

$$\frac{\partial \rho_1}{\partial t} + \nabla \cdot (\rho_0 \mathbf{V_1}) = 0, \tag{1.17}$$

$$\rho_0 \frac{\partial \mathbf{V_1}}{\partial t} = -\nabla P_1 + \frac{1}{\mu_0} \left(\nabla \times \mathbf{B_1} \right) \times \mathbf{B_0}, \tag{1.18}$$

$$\gamma P_0 \frac{\partial \rho_1}{\partial t} = \rho_0 \frac{\partial P_1}{\partial t}, \tag{1.19}$$

$$\frac{\partial \mathbf{B_1}}{\partial t} = \nabla \times \left(\mathbf{V_1} \times \mathbf{B_0} \right), \tag{1.20}$$

$$\nabla \cdot \mathbf{B_1} = 0. \tag{1.21}$$

Then, by taking (1.18), differentiating with respect to t, and using the other equations to eliminate P_1 and ρ_1 we obtain:

$$\rho_0 \frac{\partial^2 \mathbf{V_1}}{\partial t^2} = \gamma P_0 \nabla^2 \mathbf{V_1} + \frac{1}{\mu_0} \left[(\nabla \times (\nabla \times (\mathbf{V_1} \times \mathbf{B_0}))) \times \mathbf{B_0} \right]. \tag{1.22}$$

This is the basic equation for studying MHD oscillations. To progress, we assume perturbations that are of the form: $A_1(\mathbf{r}, t) = A_{1,0} \exp i(\omega t - \mathbf{k} \cdot \mathbf{r})$, where $A_{1,0}$ is a constant, ω is the frequency and $\mathbf{k} = k\hat{\mathbf{x}} + l\hat{\mathbf{y}} + m\hat{\mathbf{z}}$ is the wavevector. This Fourier decomposition has the advantage that temporal derivatives can be replaced by $i\omega$, and spatial derivatives by $-i\mathbf{k}$. Then substituting these into (1.22) we get:

$$\rho_0 \omega^2 \mathbf{V_1} = \gamma P_0 \mathbf{k}(\mathbf{k} \cdot \mathbf{V_1}) + \frac{1}{\mu_0}[(\mathbf{k} \times (\mathbf{k} \times (\mathbf{V_1} \times \mathbf{B_0}))) \times \mathbf{B_0}]. \tag{1.23}$$

The first mode to consider is an incompressible one, that is a mode where there are no pressure or density variations from (1.17) $\nabla \cdot \mathbf{V_1} = 0$ hence: $\mathbf{k} \cdot \mathbf{V_1} = 0$, as such the first term on the RHS of (1.23) is zero. By considering the two remaining terms it is clear that $\mathbf{V_1}$ and $\mathbf{B_0}$ are perpendicular, hence $\mathbf{V_1} \cdot \mathbf{B_0} = 0$. By using the following vector triple product rules:

$$\mathbf{A} \times (\mathbf{B} \times \mathbf{C}) = (\mathbf{A} \cdot \mathbf{C})\mathbf{B} - (\mathbf{A} \cdot \mathbf{B})\mathbf{C},$$
$$(\mathbf{A} \times \mathbf{B}) \times \mathbf{C} = (\mathbf{A} \cdot \mathbf{C})\mathbf{B} - (\mathbf{B} \cdot \mathbf{C})\mathbf{A},$$

and removing all the terms which are zero we get:

$$\rho_0 \omega^2 \mathbf{V_1} = \frac{(\mathbf{k} \cdot \mathbf{B_0})^2}{\mu_0} \mathbf{V_1}. \tag{1.24}$$

Rewriting $\mathbf{B_0}$ as $B_0\hat{\mathbf{B}}_0$, where $\hat{\mathbf{B}}_0$ is the unit vector in the direction of the magnetic field, and cancelling the $\mathbf{V_1}$ this becomes a dispersion relation:

$$\omega^2 = \frac{B_0^2}{\rho_0 \mu_0} (\mathbf{k} \cdot \hat{\mathbf{B}}_0)^2 \tag{1.25}$$

This describes transverse anisotropic oscillations which propagate preferentially in the direction of the magnetic field. These oscillations are known as Alfvén waves. The coefficient on the RHS of (1.25) gives the Alfvén speed: $C_A = \frac{B_0}{\sqrt{\rho_0 \mu_0}}$, which is an important plasma parameter.

Now to return to (1.23) to consider compressible modes of oscillation. As this is a vector equation it is simpler to consider components of these vectors, so as to deal with scalar equations. In the set-up of the problem there are only two directions that have been defined:

the direction of the magnetic field, which for simplicity we will assume is oriented along the z-axis, $\hat{\mathbf{B}}_0 = \hat{\mathbf{z}}$, and the direction of the wavevector, $\mathbf{k}$. To proceed we take the dot product of (1.23) first with $\hat{\mathbf{z}}$, and then $\mathbf{k}$. Firstly $\cdot\hat{\mathbf{z}}$ gives:

$$\omega^2 V_z = C_s^2 m(\mathbf{k} \cdot \mathbf{V_1}), \tag{1.26}$$

where $C_s^2 = \frac{\gamma P_0}{\rho_0}$ is the square of the sound speed, and m is the Z-component of the wavevector. Next, $\cdot\mathbf{k}$:

$$\omega^4(\mathbf{k} \cdot \mathbf{V_1}) = \frac{\gamma P_0}{\rho_0} K^2(\mathbf{k} \cdot \mathbf{V_1}) + \frac{B_0^2}{\rho_0 \mu_0} \mathbf{k} \cdot [(\mathbf{k} \times (\mathbf{k} \times (\mathbf{V_1} \times \hat{\mathbf{z}}))) \times \hat{\mathbf{z}}], \tag{1.27}$$

where $K^2 = \mathbf{k} \cdot \mathbf{k}$. Using the definitions of the Alfvén and sound speed, as well as the vector triple product rules, this simplifies to:

$$\omega^2(\mathbf{k} \cdot \mathbf{V_1}) = (C_s^2 + C_A^2)K^2(\mathbf{k} \cdot \mathbf{V_1}) - mK^2 C_A^2 V_z. \tag{1.28}$$

Now substituting V_z from (1.26) into the final term of (1.28) will give a common factor of $\mathbf{k} \cdot \mathbf{V_1}$ in all terms. The case where $\mathbf{k} \cdot \mathbf{V_1} = 0$ has already been considered, as it led to the dispersion relation for Alfvén waves. We therefore consider the case where $\mathbf{k} \cdot \mathbf{V_1} \neq 0$ this factor can then be cancelled leaving the following:

$$\omega^4 - K^2\omega^2(C_s^2 + C_A^2) + C_s^2 C_A^2 m^2 K^2 = 0. \tag{1.29}$$

This is quadratic in ω^2, so simply finding the roots gives us the dispersion relation for these oscillations:

$$\omega^2 = \frac{K^2}{2}\left[C_S^2 + C_A^2 \pm \sqrt{(C_s^2 + C_A^2)^2 - 4K^2 C_s^2 C_A^2 \cos^2(\theta)}\right], \tag{1.30}$$

where θ is the angle between the wavevector and the magnetic field, the parameter arises as $m^2 = K^2 \cos^2(\theta)$. This dispersion relation describes two modes of oscillation, depending on the choice of sign in the RHS. The large root denotes the fast magnetoacoustic mode, the smaller root the slow magnetoacoustic mode. As with the Alfvén waves, these waves are also anisotropic, due to the $\cos(\theta)$ term in the dispersion relation.

Fig. 1.5.1 shows the phase speed of all three MHD modes on a polar diagram, demonstrating how the phase speed varies with the angle between the wave vector and the magnetic field. Starting with $\theta = 0$, that is parallel to the magnetic field, the phase speed of the Alfvén mode is the Alfvén speed, the phase speed of the slow mode will always be equal to the smaller of C_A and C_s, in this case, C_s. The phase speed of the fast mode will

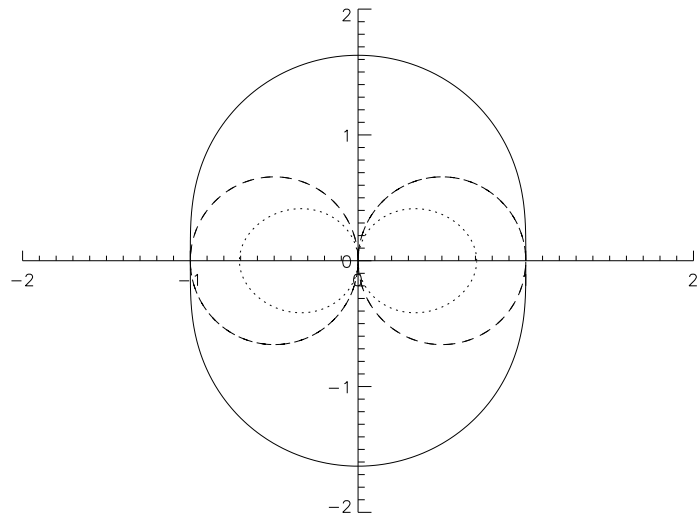Figure 1.5: Polar diagram showing the phase velocity for the three MHD modes of a uniform plasma. The magnetic field is oriented in the horizontal direction. The solid line represents the fast magnetoacoustic mode, the dotted line the slow magnetoacoustic mode and the dashed line the Alfvén mode. Here, C_A is normalised to 1, and $C_s = 0.7$. In this diagram the magnetic field is oriented in the x-direction
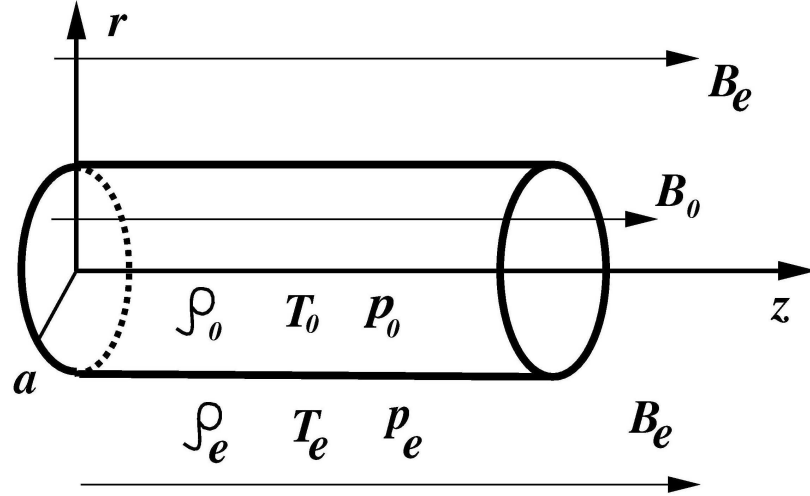
Figure 1.6: Diagram showing the magnetic cylinder as set up by Zaitsev and Stepanov [1975]. (From the University of Warwick PX420 Solar MHD lecture notes)

always be equal to the larger of the two, in this case, C_A. As θ increases to $\pi/2$ the Alfvén and slow mode's phase speeds decrease until they become 0 at $\theta = \pi/2$, whereas the fast mode's increases to $v_{ph} = \sqrt{C_s^2 + C_A^2}$.

1.5.2 Theoretical basis for coronal loop oscillations

The oscillations detailed in the previous section, whilst very nice analytically, are not very useful for modelling the corona. This is because the corona is clearly not a homogeneous environment, therefore not only is the starting equilibrium unrealistic it is also not possible to perform a Fourier transform in all directions.

A more realistic plasma geometry to model is that of a cylinder. Such analysis was performed by Zaitsev and Stepanov [1975]. They started by considering a plasma cylinder of infinite length embedded in a magnetic field aligned along the axis of the cylinder, as illustrated in Fig. 1.6. The equilibrium parameters in this set-up are as follows: inside the cylinder the pressure is P_0, the density is ρ_0 and the magnetic field is $\mathbf{B_0} = B_0\hat{\mathbf{z}}$. The exterior equilibrium parameters are: P_e, ρ_e and $\mathbf{B_e}$. As before, check that the equilibrium parameters satisfy the MHD equations; all are trivially satisfied aside from (1.2), which is satisfied so long as the interior and exterior magnetic and gas pressures balance, i.e:

$$P_0 + \frac{B_0^2}{2\mu_0} = P_e + \frac{B_e^2}{2\mu_0}. \tag{1.31}$$

A similar approach is then followed as in the homogeneous plasma: taking the MHD equations, applying small perturbations and linearising. The small perturbations are assumed to be of the form: $A_1(r, \theta, z, t) = A_1(r) \exp(i\omega t + im\theta + ikz)$ i.e. a Fourier transform is performed in all directions aside from the radial direction, as the equilibrium conditions are constant in all these directions. After some algebra (see. Zaitsev and Stepanov [1975] or Roberts [1981a,b]; Edwin and Roberts [1983] for details) the following wave equation for the radial component of the divergence of the velocity, i.e. $R(r)$ where: $\nabla \cdot \mathbf{V_1} = R(r) \exp(i\omega t + im\theta + ikz)$, is reached:

$$\frac{d^2R}{dr^2} + \frac{1}{r}\frac{dR}{dr} - \left(\kappa^2 + \frac{m^2}{r^2}\right)R = 0, \tag{1.32}$$

where

$$\kappa^2 = \frac{(k^2C_s^2 - \omega^2)(k^2C_A^2 - \omega^2)}{(C_s^2 + C_A^2)(k^2C_T^2 - \omega^2)}, \tag{1.33}$$

where C_T is the tube speed, and is defined as:

$$C_T = \frac{C_sC_A}{\sqrt{C_s^2 + C_A^2}}. \tag{1.34}$$

Note that for instance both κ and C_T will have different values outside and inside the cylinder. In keeping with convention, parameters of the external plasma are denoted by subscript e, and internal equilibrium parameters are denoted with a subscript 0.

Equation (1.32) is Bessel's equation, which can in many ways be considered the cylindrical analogue of the standard cartesian wave equation. For the cartesian wave equation there are two families of solutions, depending on the sign of the coefficient of the spatial derivative: either exponential ($\exp(x)$ and $\exp(-x)$), or sinusoidal ($\sin(x)$ and $\cos(x)$). As Bessel's equation is a cylindrical equivalent of this, its solutions can also be considered equivalents of these functions. If $\kappa^2 < 0$ then the solutions are the oscillatory functions: J_m and Y_m, known as Bessel functions of the first and second kind respectively. If $\kappa^2 > 0$ then the solutions are exponential: I_m is exponentially growing and K_m is exponentially decaying. These are known as the modified Bessel functions of the first and second kind respectively. A final important point to note about Bessel functions is that all of these functions have a subscript m denoting the order of the function; this is the same m from (1.32), as well as being the azimuthal wavenumber. If we keep r, t and z fixed, but vary θ, that is travelling around the cylinder, all quantities must be continuous at $\theta = 0, 2\pi$. In order to ensure this, m must be an integer.

These functions can therefore be used to describe the perturbations inside and outside the cylinder. In order to further restrict the solutions available, we must apply boundary con-

ditions. Starting with the cylinder's interior, we require that R is bounded at the cylinder's axis, $r = 0$, this means that inside the cylinder the solutions are as follows:

$$R(r) = A_0 \begin{Bmatrix} I_m(m_0 r) & , m_0^2 > 0 \\ J_m(n_0 r) & , n_0^2 = -m_0^2 > 0 \end{Bmatrix} (r < d). \tag{1.35}$$

The Bessel function chosen depends on whether m_0^2 is positive or negative. If m_0^2 is positive, there is no oscillatory behaviour inside the cylinder, and the Bessel I_m function is used. In the case where $m_0^2 > 0$, the only oscillatory behaviour exists on the boundary of the cylinder therefore these oscillations are known as surface modes. When $m_0^2 < 0$, the Bessel J_m function is used. This function involves oscillatory behaviour inside the cylinder, and as such these modes are known body modes.

The first requirement imposed on the solution in the exterior of the cylinder is that $R(r) \to 0$ as $r \to \infty$, which eliminates the Bessel I_m function. We also require that this oscillation be a standing wave of constant amplitude, hence the energy in the system must remain constant. The only input of energy is from the initial "push" of applying the perturbation at $t = 0$, therefore we only consider solutions where no energy escapes the cylinder. The Bessel J_m and Y_m functions describe oscillations, thus if either of these functions represent solutions to the exterior of the cylinder, where there is no radial boundary to constrain them they would transport energy away from the cylinder, essentially damping the cylinder's oscillation. Therefore the external solution must be:

$$R(r) = A_e K_n(m_e r), \quad r > d. \tag{1.36}$$

The final condition to be applied is that $R(r)$ should be continuous at the boundary $r = d$, that is that (1.35) and (1.36) should match at the boundary. This combined with the equilibrium pressure balance gives the following dispersion relations:

$$\rho_0(k^2 C_{A0}^2 - \omega^2) m_e \frac{K_m'(m_e d)}{K_m(m_e d)} = \rho_e(k^2 C_{Ae}^2 - \omega^2) m_0 \frac{I_m'(m_0 d)}{I_m(m_0 d)}, \tag{1.37}$$

for the surface modes, and:

$$\rho_0(k^2 C_{A0}^2 - \omega^2) m_e \frac{K_m'(m_e d)}{K_m(m_e d)} = \rho_e(k^2 C_{Ae}^2 - \omega^2) n_0 \frac{J_m'(n_0 d)}{J_m'(n_0 d)}, \tag{1.38}$$

for the body modes. These dispersion relations therefore describe the modes of oscillation, as well as restricting the values of ω and k that are allowed. The properties of these oscillations depend heavily on the relative values of the external and internal sound and Alfvén speeds. Edwin and Roberts [1983] considered a wide selection of possible scenar-
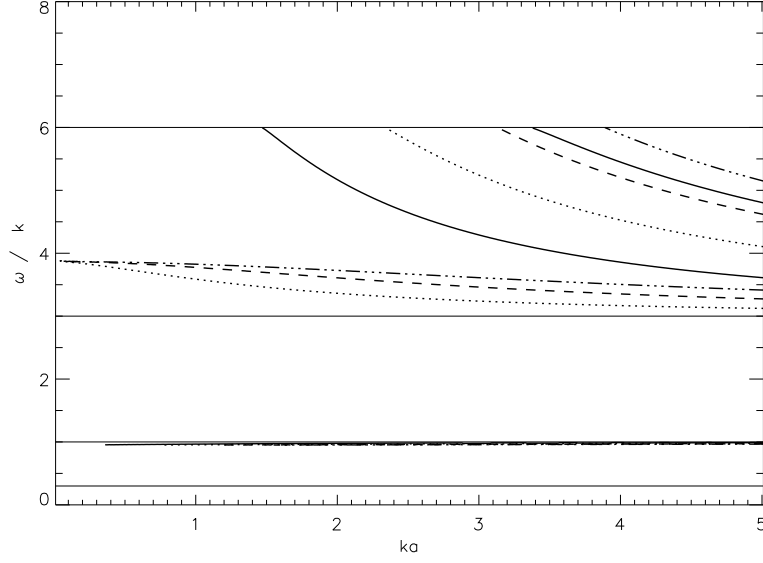
Figure 1.7: Dispersion plot for $C_{Ae} = 6$, $C_{A0} = 3$, $C_{s0} = 1$, $C_{se} = 0.3$, $m = 0, 1, 2, 3$, the solid line is $m = 0$, the dotted line $m = 1$, the dashed line $m = 2$, the dashed-dotted line $m = 3$ and the horizontal lines are the characteristic speeds of the system. Only the highest of the slow branches for each value of m is plotted.

ios of solar conditions, we will however restrict ourselves to a set of typical coronal values: $C_{Ae} > C_{A0} > C_{s0}, C_{se}$. We then use a numerical method (e.g. Newton-Raphson method) to find the roots to these dispersion relations, that is the values of ω, k and m for which a solution exists (restricting m to integer values as stated above). Fig. 1.7 is a dispersion plot showing the modes of the cylinder. It is plotted as the phase speed against the wavenumber to help visualise the regions where oscillations exist, note the horizontal solid lines on the plot represent the characteristic speeds of the cylinder: C_{se}, C_{s0}, C_{A0} and C_{Ae}. There are two distinct intervals of the phase speed which allow oscillations. Firstly $C_{se} < \omega/k < C_{s0}$: these modes are analogous to the slow magnetoacoustic modes of a uniform plasma; these modes exist purely in the range: $C_{T0} < \omega/k < C_{s0}$, here $C_{T0} = 0.949$. All of these modes exist for all values of k, and as such this is a very small range of phase speeds for all these modes to be plotted in, hence it is difficult to distinguish individual modes. In fact for each value of m there are an infinite number of modes, representing all of the harmonics, however in this plot only one mode for each value of m is plotted. The consequence of all of these modes being so close together is that it is difficult to distinguish individual modes, and in practice it would be impossible to only excite a single one of these slow modes without also exciting many other modes. These slow modes are therefore essentially treated all together, and are not ideal for further analysis.

Moving our attention to the other region of Fig. 1.7 where oscillations are allowed: $C_{A0} < \omega/k < C_{Ae}$. These are modified fast magnetoacoustic modes, here modes are sufficiently spread out that distinguishing individual modes is clearly possible, which suggests that it is also possible to excite single modes. The other feature of this region of the plot that differs from the slow modes is that not all of the modes exist for all values of k; some of the modes have "cut-off" values of k, that is values of k below which the mode does not exist under the assumptions made above.

In fact the $m = 0$ mode has no branches that exist for all values of k, which is a very important property of this mode. The $m = 0$ mode is known as the "sausage mode", because $m = 0$ describes axisymmetric behaviour, and the expansions and contractions of the tube along its length make it resemble a string of sausages. This mode will be discussed in much more detail in further chapters.

The $m \neq 0$ modes all have one branch that exists for all values of k, their fundamental mode, all of which have $\omega/k \to$ a single value as $k \to 0$. This is another characteristic speed of the cylinder, known as the kink speed, C_k and is defined as:

$$C_k = \sqrt{\frac{\rho_0 C_{A0}^2 + \rho_e C_{Ae}^2}{\rho_0 + \rho_e}}, \tag{1.39}$$

for the values used in Fig. 1.7 $C_k = 3.81$. The $m = 1$ mode represents purely a displacement of the cylinder, without deforming it, it is similar to a guitar string being plucked. As such it is known as the "kink mode" as it resembles a kink in the cylinder. The $m > 1$ modes are known as the "fluting modes", as for higher values of m the cylinder begins to resemble a fluted column. These modes represent a complex deformation of the cylinder, which are difficult to excite without also exciting the kink or sausage mode which would dominate, as such these modes generally not considered when analysing the modes of the cylinder.

The values for the ratios of sound and Alfvén speeds in Fig. 1.7 are not necessarily representative of the corona, where we would expect the sound speeds to be lower. However changing the specific values does not alter qualitative behaviour of these modes; the most important property is that $C_{Ae} > C_{A0} > C_{s0}, C_{se}$, so long as this holds the overall behaviour remains unchanged.

One limitation of this model that could be lifted is that the external solution to 1.32 is restricted to the Bessel K_m functions, so as there is no external wave transmitting energy away from the cylinder. If we allow for the Bessel Y_m function to be a solution outside of the cylinder, this expands the range of possible solutions; this was considered by Cally [1986]. The effect of having an external oscillating solution is that as energy is transported away the internal oscillation is effectively damped, though it is important to note that no actual damping occurs; the internal oscillation's energy is merely transferred to the external

oscillation. Hence the regions of the dispersion relation where the external solution is the Bessel K_m function will correspond to a complex value for ω. These solutions are known as leaky oscillations and occur on Fig. 1.7 for $\omega/k > C_{Ae}$, acting as continuations of the modes that have cutoff wavenumbers. This is particularly important for $m = 0$, the sausage mode, as it is the only value of m for which the fundamental mode has a cutoff wavenumber, thus for ks below this value the only sausage mode that exists is leaky.

Chapter 2

Sausage oscillations of a plasma cylinder

2.1 Introduction

This section is concerned with the study of an axisymmetric sausage mode oscillation of a plasma cylinder. The most likely observational signatures of sausage oscillations in the corona are the long period quasi-periodic pulsations (QPPs) in flaring loops. Nakariakov and Melnikov [2009] provide a recent review on the topic of QPPs. QPPs are observed as an oscillation in the intensity of radiation emitted during some flares. They have been observed in many bands such as microwave and hard X-ray emission, and have been observed as simultaneous in phase oscillations in both bands [e.g. Asai et al., 2001]. QPPs have been observed with a wide range of periods of oscillation varying from fractions of a second [Aschwanden, 1987; Fleishman et al., 2002; Tan, 2008] to several minutes [Foullon et al., 2005; Kislyakov et al., 2006]. The underlying mechanism that drives these oscillations is not fully understood, and several mechanisms have been suggested. Given the wide range of periods these oscillations display, it is reasonable to assume that different mechanisms could be responsible for different QPPs. Nakariakov and Melnikov [2009] suggest dividing the oscillations into two categories: the short ($P < 1$s) period oscillations and longer period oscillations. The shorter period oscillations are unlikely to be caused by MHD oscillations, and as such are of less interest to this study.

Sausage oscillations are an excellent candidate to explain some of these QPPs. The method by which sausage oscillations could produce a modulation of hard X-ray intensity was described by Zaitsev and Stepanov [1982]. A description of this mechanism is as follows: during the flare a 'kernel' of very hot plasma forms at the apex of the loop, which increases the gas pressure at this point causing the loop peak to expand, as well as reducing the mag-
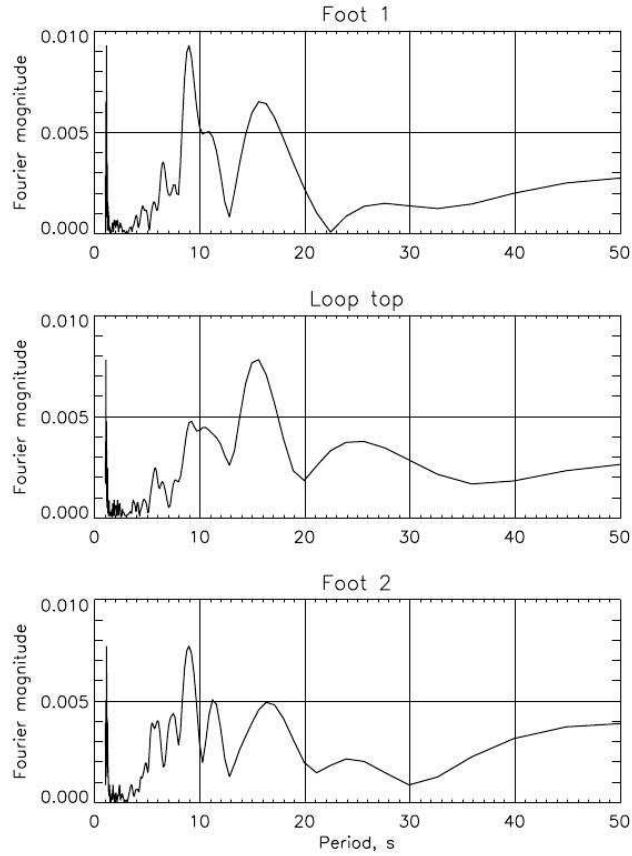
Figure 2.1: Fourier power spectra of the pulsations observed at three points along a loop by NoRH on the 12th January 2000. Figure from Nakariakov et al. [2003].

netic field strength there. This reduced magnetic field forms a magnetic trap holding the energetic electrons in place. Now if a sausage mode is excited in the loop this will cause a modulation in the magnetic field strength of the loop apex, which therefore leads to a modulation in the effectiveness of the magnetic trap. The trap therefore releases a modulated stream of electrons which travel down the loop towards the dense plasma in the footpoints. As the electrons crash into this plasma they are rapidly decelerated and release hard X-rays that are then observed, hence the sausage mode leads to a modulation in hard X-ray emission.

Sausage oscillations also provide a mechanism by which the microwave emission from a flare can be modulated. Microwave emission from a flare could be caused by the gyrosynchrotron mechanism. This is where mildly relativistic non-thermal electrons are caught by the background magnetic field. As these very high speed electrons orbit the magnetic field line, they emit broadband microwave radiation. The spectrum of these microwaves

is controlled by the electron's speed and magnetic field strength. As such modulating the magnetic field strength e.g. by a sausage mode, will also modulate the gyrosynchrotron emission. Such an observation was made by Nakariakov et al. [2003] who studied a flare on the solar limb on 12th of January 2000 using the Nobeyama Radioheliograph (NoRH) [Nakajima et al., 1994]. NoRH measures microwave intensities in the 17 and 34 GHz bands with a spatial resolution of 10"-5" and a temporal resolution of 0.1 s; the excellent temporal resolution is very useful in studying QPPs, which can have periods of a few seconds. Nakariakov et al. [2003] looked at the 17 GHz flux at three points along the loop: one point in each of the legs and a point at the top of the loop. For the timeseries of each of these points, the overall trend was removed and a Fourier spectrum of the remaining signal was then made, the spectra are shown in Fig. 2.1. There is a clear peak in all spectra at $14 - 17$ s which is most prominent at the apex, this is likely to be the fundamental sausage mode. There is a second peak at $8 - 11$ s, which is more prominent at the footpoints; it is therefore possible that this could be the second spatial harmonic of the sausage mode.

An excellent example of a detailed study of a QPP observed in both the microwave and X-ray bands is provided by Inglis et al. [2008], using data from NoRH as well as X-ray observations from the Hard X-ray Telescope on-board the Yohkoh satellite (Yohkoh/HXT). They found a good agreement between microwave and hard X-ray observations, which led to the conclusion that this QPP was caused by some form of MHD oscillation, of which the sausage mode is the most likely candidate.

QPPs have also been observed in the visible portion of the spectrum, as shown by Srivastava et al. [2008] who used Hα (6563 Å) observations from the 15 cm Solar Tower Telescope at Arybhatta Research Institute of Observational Sciences. They considered a flaring loop from 2nd May 2001 and studied the intensity from a point near the footpoint as well as at the apex. They found periodicity in the signal from both points, which they interpreted as being caused by the fundamental sausage mode.

Observations of QPPs have not just been limited to the Sun, for example Mathioudakis et al. [2003] studied an observation of a flare from RS CVn binary II Peg, a binary star system 130 light years from Earth. Using observations from the Stephanion observatory they found periodicity in the white light emission of 220 s, which could be explained by a sausage oscillation.

Very recently, periodic variations of the EUV emission were also interpreted in terms of sausage oscillations [Van Doorsselaere et al., 2011; Su et al., 2012]. In these interpretations it is important to consider the line-of-sight integration effect, as recently pointed out by Mossessian and Fleishman [2012] and Gruszecki et al. [2012]. In particular, for a line of sight perpendicular to the oscillating cylinder and for a spatial resolution of the order

of the diameter of the cylinder or poorer, the intensity perturbations produced by a sausage mode in the optically thin emission regime are negligible.

Theoretical modelling of sausage modes of coronal structures has a long history. Sausage modes are highly dispersive and their properties are dependent upon the longitudinal wavenumber (e.g., Zaitsev and Stepanov [1982]; Edwin and Roberts [1983]; Roberts et al. [1984]; Selwa et al. [2004]). Depending upon the ratio of the longitudinal wavelength (determined, e.g., in the case of standing waves by the length of the oscillating loop) to the radius of the plasma cylinder, the mode can be either trapped or leaky. Trapped modes experience total internal reflection at the cylinder surface and are evanescent outside the loop. The period of standing trapped sausage modes, i.e., in dense and thick flaring loops, grows with wavelength [Nakariakov et al., 2003; Aschwanden et al., 2004]. Sausage modes of longer wavelengths leak from the cylinder, forming a train of outwardly propagating fast magnetoacoustic waves outside the cylinder. This mechanism of wave leakage is intrinsic and different from the tunnelling caused by non-uniformity of the external medium (see, e.g., Verwichte et al. [2006]). The threshold value of the ratio of the longitudinal wavelength to the radius of the cylinder is defined by the ratio of the fast magnetoacoustic speeds inside and outside the cylinder [Zaitsev and Stepanov, 1982; Edwin and Roberts, 1983]. Such a behaviour was found to be weakly sensitive to the smoothness of the transverse profile of the fast speed [Pascoe et al., 2007a], fine structure in the form of multiple coaxial shells [Pascoe et al., 2007b], longitudinal variation of the cylinder cross-section [Pascoe et al., 2009b], and finite-β effects [Inglis et al., 2009].

However, sausage modes are still not entirely understood. In particular, the dependence of the time period on the longitudinal wavelength in the leaky regime, information crucial for the development of seismological techniques based upon this mode, is still debated. On the one hand, analysis of dispersion relations for linear sausage perturbations clearly showed that in the long-wavelength regime the period of leaky sausage modes is independent of wavelength [e.g. Zaitsev and Stepanov, 1982; Cally, 1986; Kopylova et al., 2002, 2007] and is determined by the ratio of the radius of the cylinder to the internal value of the fast speed. On the other hand, it was argued that the gradual increase in wavelength from a trapped regime value should lead to an increase in the period [Nakariakov et al., 2003; Aschwanden et al., 2004] for a fixed value of the radius of the cylinder. Moreover, numerical simulations of the initial-value problem demonstrated that the period of the mode grows with wavelength [e.g. Pascoe et al., 2007a; Inglis et al., 2009] in both trapped and leaky regimes. The situation is complicated by difficulties in searching analytically for the complex roots of the transcendental algebraic equations representing the dispersion relations [Ruderman and Roberts, 2006].

In this section we aim to resolve this long-standing discrepancy. We analyse an initial-

value problem, considering the evolution of an axially symmetric perturbation of a straight plasma cylinder embedded in a uniform magnetic field, as in the works of Pascoe et al. [2007a]; Inglis et al. [2009]; Gruszecki et al. [2012]. In contrast to Pascoe et al. [2007a]; Inglis et al. [2009], where a plane plasma slab was considered, we study sausage modes of a plasma cylinder. Moreover, we extend the range of the parameters of the problem, considering ratios of the length of the perturbed cylinder to its diameter up to 60 and ratios of the Alfvén speeds outside and inside the cylinder up to 20. In previous studies these parameters were considered up to 15 and 7, respectively [Inglis et al., 2009]. In addition, we study the dependence of the sausage mode period on the steepness of the transverse profile of the plasma in the cylinder. We consider a radially non-uniform plasma cylinder embedded in a uniform and straight magnetic field in the zero-β regime. We perform a parametric study of the sausage mode of this plasma equilibrium, varying the contrast of the Alfvén (fast magnetoacoustic) speed inside and outside the cylinder and the steepness of the plasma non-uniformity in the radial direction. We considered the transition from the short-wavelength trapped regime to the long-wavelength regime, investigating how the dependence of the period on the wavelength evolves to its independence.

2.2 Numerical model

Consider a smooth cylinder of zero-β plasma, stretched along a uniform magnetic field, B_0 directed in the z-direction. The density of the plasma ρ_0 decreases with radial coordinate, r. This is the standard setup for studying coronal loop oscillations, as described in section 1 (Fig. 1.6). Unlike the cylinder considered in section 1 the Alfvén speed is now continuous, increasing in the radial direction, and is modelled by the function:

$$C_A(r) = \frac{B_0}{\sqrt{\mu_0 \rho_0(r)}} = C_{A\infty} \left[1 - \delta \exp\left(-\frac{r^\alpha}{d^\alpha} \right) \right], \tag{2.1}$$

where $C_{A\infty}$ is the Alfvén speed at infinity, $0 < \delta < 1$ is the decrease in the Alfvén speed at the axis of the cylinder, as compared to $r \to \infty$. The index, $\alpha > 1$ dictates the steepness of the profile, d is the effective radius of the cylinder (as $\alpha \to \infty$ the case considered by Edwin and Roberts [1983] is recovered, and d is the cylinder's radius), and μ_0 is the permeability of free space. The Alfvén speed at the cylinder's axis is therefore: $C_{A0} = C_{A\infty}(1 - \delta)$. Thus by varying the parameters δ and α we change the contrast ratio $C_{A0}/C_{A\infty}$ and the steepness of the radial profile respectively. As the magnetic field is uniform and the gas pressure is taken to be negligible due to the zero-β approximation, the equilibrium total pressure is constant everywhere. Hence the parameter $\delta = 1 - C_{A0}/C_{A\infty}$ is connected with the contrast of the equilibrium plasma density ρ_0 at the cylinder's axis, and at infinity as
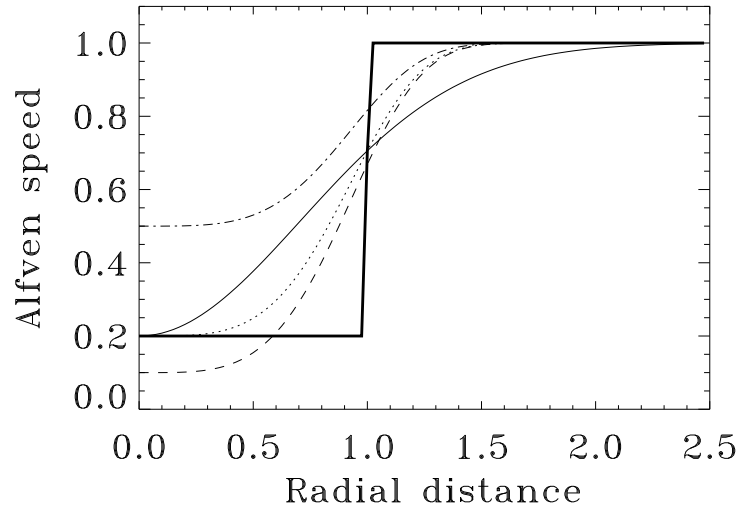
Figure 2.2: Examples of the radial profiles of the Alfvén speed in the plasma cylinder considered for different values of the parameters α and δ, which control the steepness and depth of the profile, respectively. The thick solid curve corresponds to $\alpha = \infty$, $\delta = 0.8$, the thin solid curve to $\alpha = 2$, $\delta = 0.8$, the dotted curve to $\alpha = 4$, $\delta = 0.8$, the dashed curve to $\alpha = 4$, $\delta = 0.9$, and the dot-dashed curve to $\alpha = 4$, $\delta = 0.5$. The Alfvén speed is normalised to its value at infinity and the radial distance is normalised to the effective radius of the cylinder.

$\delta = 1 - [\rho_0(\infty)/\rho_0(0)]^{1/2}$. It is important to note that as $\alpha \to \infty$ the step profile is recovered. Fig. 2.2 shows examples of several Alfvén speed profiles using this setup.

As previously we restrict ourselves to dissipationless processes, described by the ideal MHD equations:

$$\rho \left[\frac{\partial \mathbf{V}}{\partial t} + (\mathbf{V} \cdot \nabla)\mathbf{V} \right] = \mathbf{j} \times \mathbf{B},$$

$$\frac{\partial \mathbf{B}}{\partial t} = \nabla \times (\mathbf{V} \times \mathbf{B}),$$

$$\frac{\partial \rho}{\partial t} + \nabla \cdot (\rho \mathbf{V}) = 0,$$

where the vectors $\mathbf{V}$ and $\mathbf{B}$ are the plasma velocity and magnetic field, respectively, and ρ is the plasma density. In the momentum equation the $-\nabla P$ term has been dropped, as it is 0 in the zero-β approximation, which is a justifiable approximation for the study of sausage modes of coronal loops [Inglis et al., 2009].

It is natural to use a cylindrical coordinate system, with the z-axis coinciding with the axis of the cylinder and with ϕ and r the azimuthal and radial coordinates, respectively. Considering linear magetoacoustic perturbations of the cylindrical equilibrium given by (2.1); and taking perturbations to be independent of the azimuthal angle, ϕ, as we are only interested in the sausage mode oscillations, we obtain the following for the perturbed quantities:

$$\frac{\partial v_r}{\partial t} = \frac{B_0}{\mu_0 \rho_0} \left(\frac{\partial B_r}{\partial z} - \frac{\partial B_z}{\partial r} \right), \tag{2.2}$$

$$\frac{\partial B_r}{\partial t} = B_0 \frac{\partial v_r}{\partial z}, \tag{2.3}$$

$$\frac{\partial B_z}{\partial t} = -B_0 \left(\frac{\partial v_r}{\partial r} + \frac{v_r}{r} \right), \tag{2.4}$$

$$\mathbf{j} = \frac{1}{\mu_0} (\nabla \times \mathbf{B}), \tag{2.5}$$

where v_r is the radial component of the plasma velocity, and B_r and B_z are the radial and longitudinal components of the perturbed magnetic field. The quantities with index 0 are the equilibrium quantities.

Then taking the time derivative of (2.2) and substituting the longitudinal derivative of (2.3) and the radial derivative of (2.4), we obtain the fast magnetoacoustic wave equation,

$$\frac{\partial^2 v_r}{\partial t^2} = \frac{B_0^2}{\mu_0 \rho_0(r)} \left(\frac{\partial^2 v_r}{\partial z^2} + \frac{\partial^2 v_r}{\partial r^2} + \frac{1}{r} \frac{\partial v_r}{\partial r} + \frac{v_r}{r^2} \right), \tag{2.6}$$

for sausage perturbations of the field aligned plasma cylinder. Slow magnetoacoustic perturbations are absent from this equation, as we ignore finite-β effects.

As the equilibrium is uniform along the axis of the cylinder (in the z-direction) we can perform a Fourier transformation with respect to this coordinate, assuming that the perturbed physical quantities depend upon z as $\cos(k_z z)$. These assumptions correspond to considering standing modes with longitudinal wavelength $2\pi/k_z$. Thus, we obtain the wave equation for the fast magnetoacoustic perturbations harmonic in the longitudinal direction,

$$C_A^{-2}(r)\frac{\partial^2 v_r}{\partial t^2} + \left(k_z^2 + r^{-2}\right)v_r - \frac{\partial^2 v_r}{\partial r^2} - \frac{1}{r}\frac{\partial v_r}{\partial r} = 0. \tag{2.7}$$

Equation (2.7) contains explicit dependence upon only two coordinates, the time t and the radial coordinate r. In particular, (2.7) describes standing sausage waves of wavelength $2\pi/k_z$, as observed in flaring coronal loops.

Due to the radial dependence of the Alfvén speed in (2.7) this equation in general does not have analytical solutions, as such a numerical approach must be attempted. An initial value problem is solved with the initial condition:

$$V_r(r, t = 0) = A_0 r \exp(-r^2/d^2), \tag{2.8}$$

where A_0 is the amplitude of the initial pulse. This form of the initial perturbation has the same symmetry as the sausage mode as it is independent of the azimuthal angle, ϕ and the plasma velocity at the axis of the cylinder is zero. The width of the perturbation in the radial direction is taken to be sufficiently large to avoid excitation of higher radial harmonics; the shape of the perturbation is close to the transverse structure of the lowest mode (see, e.g., Pascoe et al. [2007a]; Inglis et al. [2009]), with one maximum of the radial velocity perturbation in the radial direction. Higher radial sausage harmonics have more than one extremum in the radial direction, and hence are excited by our driver (2.8) less effectively. In the longitudinal direction, the initial perturbation is described by a harmonic function with wavenumber k_z. Equation (2.8) is supplemented by the boundary conditions $V_r(r = 0, t) = V_r(r = 50d, t) = 0$. The former boundary condition is imposed by the cylindrical geometry; the latter simulates the decrease of the perturbation to zero at a large distance from the cylinder.

The evolution of the initial perturbation was calculated numerically using the function *pdsolve* of *Maple* 16, which implements a second-order (in space and time) centred finite difference scheme. The convergence of this method was checked by doubling the number of grid points. The performance of this solver, in particular the radial structure of the sausage mode and its period for a given wavelength, was tested by comparing with the exact analytical results for a similar problem for a zero-β plasma slab with a symmetric Epstein profile of the density embedded in a straight magnetic field [Cooper et al., 2003]. In the cylindrical case considered in this section calculations were carried out in the domain $(0 < r < 50d,$
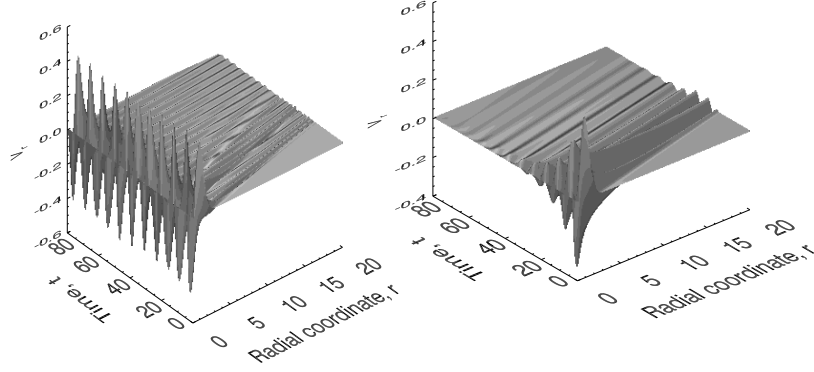
Figure 2.3: Left panel: example of a trapped oscillation, obtained for the parameters $k_z = 1.5$, $\delta = 0.8$, and $\alpha = 6$. Right panel: example of a leaky oscillation for $k_z = 0.4$, $\delta = 0.7$, and $\alpha = 6$. The time is measured in in $d/C_{A\infty}$ and the radial distance in d. The vertical axis shows the radial component of the plasma velocity measured in units of the initial amplitude A_0.

$0 < t < NdC_{A\infty}$), where N is sufficiently large (e.g., $N = 50$) for confident resolution of several periods of oscillation.

Two typical scenarios of the evolution of the initial perturbation, leaky and trapped oscillations, are shown in Fig. 2.3. The figure shows the time evolution of the radial structure of the initial impulsive perturbation which has a harmonic dependence on the longitudinal coordinate, $\cos(k_z z)$, for an arbitrary value of z. It is evident that in the trapped regime the initial excitation remains localised near the axis of the cylinder ($r = 0$) and is evanescent for higher values of r. In contrast, the leaky waves are radiated from the cylinder to the external medium as propagating fast magnetoacoustic waves. However they can be seen in the cylinder for some time after the excitation as decaying harmonic oscillations.

By analysing the signal at a chosen spatial position, e.g., $r = d$, we obtain information about the time evolution and hence the period of oscillations and the decay time. As the signal decays quickly in the leaky regime, the preferred analytical tool is to fit the time signal with an exponentially decaying harmonic function using the least-squares method. In this study we restrict our attention to the analysis of the dependence of the period on the parameters of the cylinder and the initial excitation only.
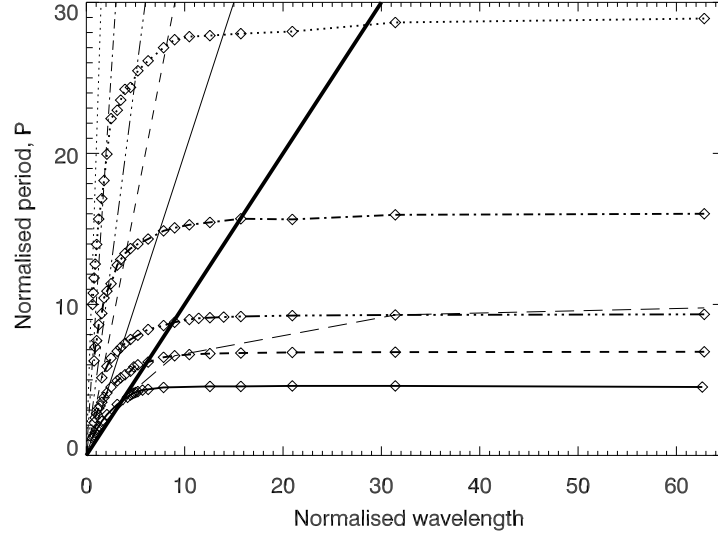
Figure 2.4: Dependence of the period of oscillations on the wavelength $2\pi/k_z$ for different values of the parameter δ that is connected with the density contrast inside and outside the cylinder. The dotted curve shows the case $\delta = 0.95$, the dot-dashed curve $\delta = 0.9$, triple dot-dashed $\delta = 0.8$, dashed $\delta = 0.7$, and the solid line is for $\delta = 0.5$. The diamonds represent the specific measurements. The value of α is 6 for all curves. The thick straight line shows the cutoff, $P = 2\pi/(k_z C_{A\infty})$. Other straight lines show the values of $P = 2\pi/[k_z C_{A\infty}(1 - \delta)]$ for the various values of δ. The long dashed line shows where the damping time is equal to three periods of oscillation. The period is measured in units of $d/C_{A\infty}$ and the wavelength in units of d.

2.3   Results

2.3.1   Dependence of the sausage mode period on the longitudinal wavelength

Figure. 2.4 shows the dependence of the period of sausage oscillations on the wavelength $2\pi/k_z$. This figure is in some ways analagous with Fig. 1.7, showing the dispersion relation for the fundamental sausage mode. In the short wavelength (large wavenumber) limit the dispersion curve is bounded by the internal wavespeed, $\omega/k_z = C_A(r = 0)$, which is represented in the figure by the straight lines whose linestyles match their dispersion curves, and is given by the expression: $P = 2\pi/(k_z C_{A\infty}(1 - \delta))$. With increasing wavelength, the period increases and the effective phase speed is in the range between the Alfvén speed in the centre of the cylinder and at infinity, which is consistent with the reasoning in Nakariakov et al. [2003]. As the wavelength increases, the growth of the period becomes less steep, gradually approaching another asymptote, $P = 2\pi/(k_z C_{A\infty})$, determined by the Alfvén speed outside the cylinder. This asymptote is represented in the figure by the line $\omega/k_z = C_{A\infty}$. An impor-
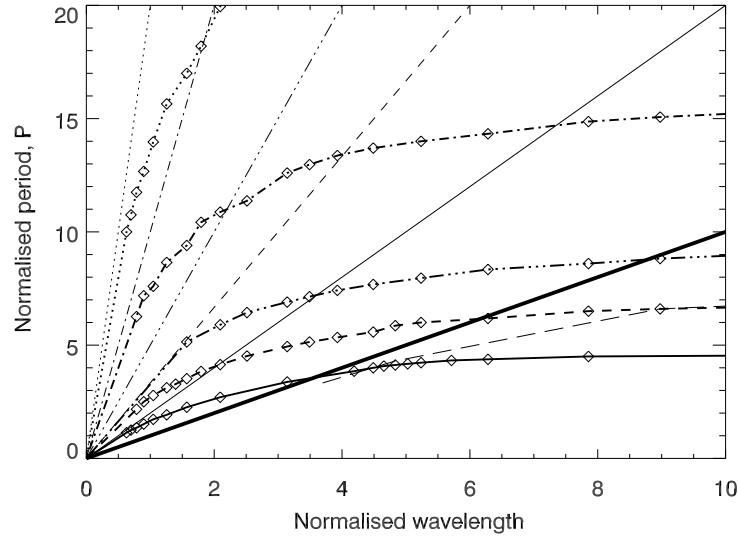
Figure 2.5: The same as Figure. 2.4, but zoomed to show the trapped regime.

tant feature of this dependence is the presence of a cutoff value. At the cutoff, the period is equal to the ratio of the wavelength to the value of the Alfvén speed at infinity.

For wavelengths shorter than the cutoff value, the oscillations are trapped and the period grows with increasing wavelength. This is consistent with the results obtained in the slab geometry [Pascoe et al., 2007a; Inglis et al., 2009]. In the weakly leaky regime, for wavelengths slightly exceeding the cutoff value, the period still grows with wavelength (see Fig. 2.5), again in agreement with the case studeied by Pascoe et al. [2007a]. For long wavelengths, the dependence of the period on the wavelength shows saturation, and the period becomes independent of wavelength. This effect is more pronounced for cylinders with higher ratios of the external to internal Alfvén speeds, in other words a cylinder with a deeper potential well in the radial profile of Alfvén speed. This effect was not found in the previous studies: Pascoe et al. [2007a]; Inglis et al. [2009], because the wavelengths in the simulation were insufficiently long to see the saturation of the sausage mode period. However a more recent study [Hornsey et al., 2014, which is covered in more depth in chapter 4] found the same saturation in the slab case. In all cases considered, for the same values of wavelength and Alfvén speed at infinity, the sausage mode periods are always longer for cylinders with lower internal Alfvén speed. In the low-β model considered, cylinders with lower internal Alfvén speed are cylinders with denser plasma.

The figure also contains a curve indicating where the damping time is equal to three periods of oscillation. Above this curve, the oscillations are of sufficiently high quality to be easily detectable in the data. Thus, leaky sausage oscillations in long dense loops, with a high
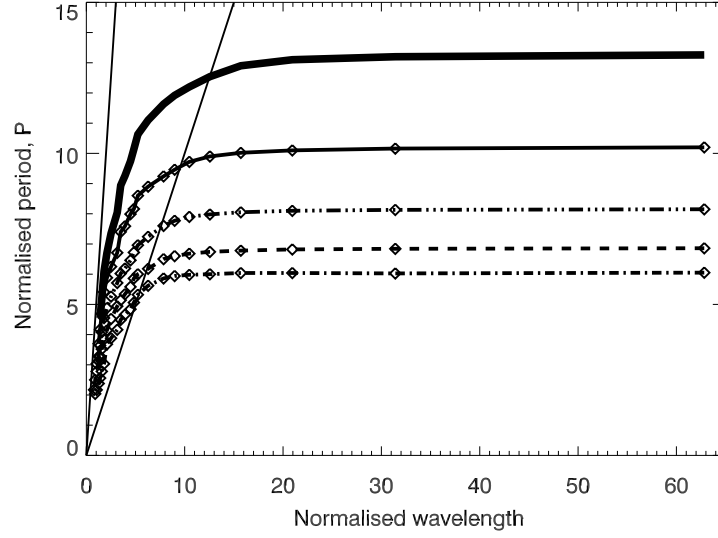
Figure 2.6: Dependence of the period of oscillations on the wavelength for different steepnesses of the radial profile, α. The thick solid line corresponds to $\alpha = \infty$, the thin solid line to $\alpha = 8$, the triple dot-dashed line to $\alpha = 6$, the dashed line to $\alpha = 4$, and the dot-dashed line to $\alpha = 2$. The value of δ is 0.8 for all curves. The thin straight lines are the cutoffs $P = 2\pi/(k_z C_{A\infty})$ and $P = 2\pi/[k_z C_{A\infty}(1 - \delta)]$. The thick solid line shows the analytical solution in the long-wavelength limit for the step-function profile. The period is measured in units of $d/C_{A\infty}$ and the wavelength in units of d.

ratio of Alfvén speeds, can also be of sufficiently high quality, with damping time much longer than the period of oscillation to be easily detectable in the data. We must point out that the damping time considered here is connected with wave leakage only. In addition, the sausage mode can be subject to damping connected with various dissipative processes, which also reduce the quality of the oscillations. For example in hot and dense flaring loops field aligned thermal conduction [Zaitsev and Stepanov, 1982] may be such a process. This effect is not considered in this study, as the equations used are ideal.

2.3.2 Dependence of the sausage mode period on the steepness of the transverse profile

Figure 2.6 shows the effect of the transverse profile steepness on the sausage mode period. A discussed in Section 2.3.1, for the step-function profile, in the short-wavelength limit, the period is determined by the ratio of the longitudinal wavelength to the Alfvén speed at its centre. Our calculations confirm this result, which is correct for smooth profiles too. For all values of α and k_z the period is shorter than the short-wavelength asymptote, $P =$

$2\pi/[k_z C_{A\infty}(1-\delta)]$. For the same wavelength, the periods of sausage oscillations in cylinders with smoother Alfvén speed profiles, i.e. with lower indices α, are evidently shorter. This effect can be understood by considering the oscillations as a wavepacket trapped in the potential well. The distance the wavepacket travels between reflections is constant, as the width of the well and k_z are constant. However the mean wavespeed along the path is changing, and is higher for lower values of α. To understand this, consider two cases: firstly when $\alpha \to \infty$, and secondly $\alpha < \infty$. For $\alpha \to \infty$ $C_A(r) = C_{A0}$ everywhere inside the well. Thus everywhere inside the potential well the speed has its minimal value. But for a smooth profile when $\alpha < \infty$, then the value of $C_A(r)$ is larger than $C_{A0} = C_A(r = 0)$ for all values of r except at the very axis of the cylinder, $r = 0$. Hence the transverse travel time between two reflections decreases, decreasing the wave period.

Also, for steeper profiles, the cutoff value of the wavelength is found to be larger. For comparison, we show the analytical result obtained for a cylinder with a step function profile that corresponds to the limit $\alpha \to \infty$ in our consideration. Hence, as one would intuitively expect, cylinders with steeper profiles are better waveguides for fast magnetoacoustic waves with azimuthal symmetry.

From Fig. 2.6 we find that the effect of the radial steepness of the plasma cylinder on sausage oscillations is rather strong. The difference in the values of the sausage mode period between cylinders with a Gaussian ($\alpha = 2$) radial profile is more than twice as large as for a given parameter δ.

2.3.3 The long-wavelength limit

In Fig. 2.7 we demonstrate the dependence of the period in the long-wavelength limit, when it becomes independent of wavelength, on the Alfvén speed (or density) contrast in the cylinder and on the steepness of it radial profile. The period is systematically longer for higher differences between the Alfvén speeds inside and outside the cylinder, and for steeper profiles.

The thick solid line in Fig. 2.7 represents measurements made using a step function as the radial profile of the Alfvén speed. This is useful as it allows for a direct comparison with results obtained analytically. For example Kopylova et al. [2007] derived the following expression for the period of sausage modes in the long wavelength limit:

$$P = \frac{2\pi d}{\eta_j \sqrt{C_{s0}^2 + c_{A0}^2}},$$

where η_j are the zeroes of the Bessel J_0 function, for this calculation we take $\eta_j \approx 2.4$. In our calculations we are also using the zero-β approximation, so $C_{S0} = 0$. This gives the
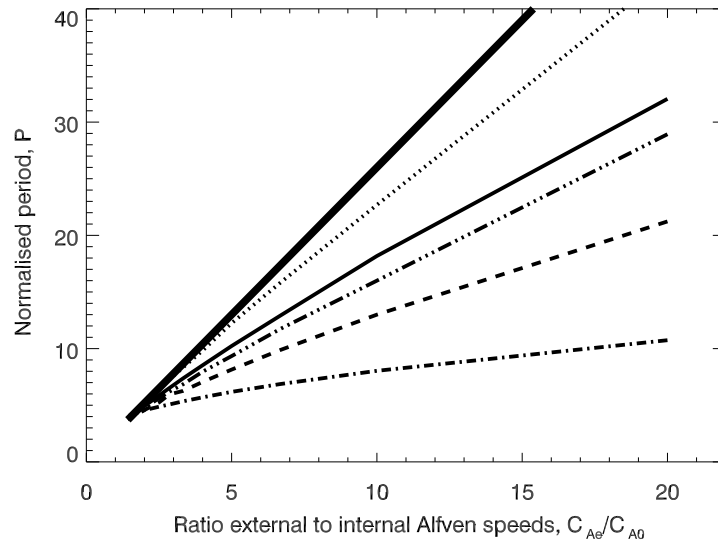
Figure 2.7: Dependence of the period, in the long-wavelength limit, on the ratio of external to internal Alfvén speeds for different steepnesses. The dotted curve corresponds to $\alpha = 20$. The other curve styles correspond to those used in Fig. 2.6. The thick solid line shows the analytical solution in the long-wavelength limit for the step-function profile. The period is measured in units of $d/C_{A\infty}$ and the wavelength in units of d.

following analytically obtained expression for the period in the long-wavelength limit for a step profile cylinder:

$$P \approx 2\pi d / 2.4 C_{A0}, \tag{2.9}$$

which agrees well with results obtained for $\alpha \to \infty$.

It is also evident that for smoother profiles the sausage mode period becomes shorter (see also the discussion in Section 2.3.2). The period grows with increasing ratio $C_{A\infty}/C_{A0}$, while for smaller values of the steepness parameter α this dependence departs from the linear relationship that appears in the $\alpha \to \infty$ cases. For a fixed value of the ratio of the Alfvén speeds, the dependence of the period on the steepness parameter α is seen to be extremely nonlinear. In particular, for $C_{A\infty}/C_{A0} = 10$, which is typical for flaring loops (e.g., Nakariakov et al. [2003]), we get an estimated formula

$$P \approx 26.1 d \tanh(\log(\alpha)). \tag{2.10}$$

This is applicable to low-β profiles steeper than Gaussian, $\alpha > 2$, and is consistent with the analytical result in the $\alpha \to \infty$ limit.

2.4   Conclusions

We performed numerical simulations of the azimuthally symmetric initial-value problem for a field-aligned low-β plasma cylinder with a smooth radial profile of the density (and hence of the Alfvén speed). The plasma cylinder was excited by a symmetric perturbation of the radial velocity of the plasma and of a harmonic shape in the longitudinal direction. Fast magnetoacoustic sausage modes were found to be easily excited in both the trapped and leaky regimes. The results obtained can be summarised as follows.

1. With increasing longitudinal wavelength, the period of the sausage oscillations always grows but this dependence is saturated in the long-wavelength limit.

2. In the trapped regime, the period lies between two values, corresponding to the ratio of the effective radius of the cylinder and the Alfvén speed at its axis and at infinity, and grows increasing in wavelength.

3. For wavelengths greater than the cutoff value, sausage modes become leaky. In response to an impulsive excitation in the cylinder, the leaky waves show decaying oscillatory behaviour with a period determined by the parameters of the cylinder (the Alfvén speed contrast ratio and steepness). Outside the cylinder, the leaky waves form a wavetrain pattern that propagates outward at the external Alfvén speed. As

expected, deeper and steeper profiles of the Alfvén speed correspond to more efficient trapping of the sausage modes: the cutoff value of the wavelength increases with steepness and the density (or Alfvén speed) contrast ratio.

4. In the leaky regime, the period is always longer than the period of a trapped mode of a shorter wavelength, and also is longer than the cutoff value (the ratio of the wavelength and the Alfvén speed far from the cylinder). For shallow profiles of the density (and hence the Alfvén speed) and shorter wavelengths, the period grows with wavelength in the leaky regime as well. In the long-wavelength limit, the period becomes independent of wavelength and is determined by the depth and steepness of the radial profile of the Alfvén speed: the period is approximately inversely proportional to the internal value of the Alfvén speed and depends on the steepness index α as $\tanh(\lg\alpha)$.

Our findings resolve the longstanding problem of the dependence or independence of the period of sausage oscillations on wavelength. Indeed, for shorter wavelengths, even in the leaky regime, the period grows with wavelength. In particular, for thick flaring coronal loops with density contrast of about 10 (and hence with an Alfvén speed contrast ratio of about 3.16) and a length of about $5 - 6$ times their diameters, as considered by Nakariakov et al. [2003] and Aschwanden et al. [2004], the period of the fundamental sausage mode indeed increases with wavelength. But for longer wavelengths (and higher density contrast ratios), the dependence of the period on wavelength experiences saturation and becomes consistent with the analytical results obtained by Zaitsev and Stepanov [1982]; Kopylova et al. [2002, 2007]. Thus we infer that opposing conclusions drawn previously concerning the dependence of the sausage mode period on wavelength were drawn in different ranges of the parameters of the problem, and hence are not contradictory. More specifically, the regime described in Pascoe et al. [2007a]; Inglis et al. [2009] corresponds to segments of the solid and dashed curves near the thick solid line in figure 2.4. On the other hand, the regime described in Zaitsev and Stepanov [1982]; Kopylova et al. [2002, 2007] corresponds to the saturation of the curves in the long wavelength part of that figure.

This result has important implications for the seismological diagnostics of plasma in flaring loops with the use of sausage oscillations. In particular, the pronounced dependence of the sausage oscillation period upon the steepness of the radial profile of the Alfvén speed provides us with a tool for probing that parameter. The transverse steepness is vital for the assessment of the efficiency of kink wave damping in the solar corona (see, e.g., Goossens et al. [2012] and references therein) and of associated coronal heating. An additional advantage of seismological techniques utilising the sausage mode is provided by its independence of the length of the loop in the long-wavelength regime. This allows one to exclude this parameter from consideration in the diagnostics of long dense loops. Moreover, equation 2.10

gives us a tool for probing the transverse profile of the Alfvén speed and density of sausage oscillations in a coronal loop provided we are able to get independent measurements of the loop diameter, d and the Alfvén speed C_{A0}. In particular, the latter parameter can come from the observation of a kink oscillation of the same loop.

Chapter 3

Comparison with analytical approximations

3.1 Introduction

The numerical model considered in Chapter 2 has also proved useful in verifying new analytical studies of the sausage mode. An example of this was performed by Vasheghani Farahani et al. [2014], and is summarised as follows:

3.2 Model

The study considers the plasma cylinder as described in section 1.5.2 and Edwin and Roberts [1983], under the zero-β approximation. The perturbations are assumed to be axisymmetric and hence only the sausage oscillations are considered. This is therefore compatible with the model described in section 2.2 when using a step profile to describe the Alfvén speed, that is $\alpha \to \infty$.

3.2.1 Solution at the cutoff wavenumber, k_c

Starting from the dispersion relation as described by Edwin and Roberts [1983] in the zero-β limit:

$$\frac{\rho_0}{\rho_e} \frac{(\omega_{A0}^2 - \omega^2)}{(\omega_{Ae}^2 - \omega^2)} \frac{m_e}{n_0} = \frac{J_1(n_0 d)}{J_0(n_0 d)} \frac{K_0(m_e d)}{K_1(m_e d)}, \qquad (3.1)$$

here we have used the property of Bessel functions that $J_0'(x) = -J_1(x)$, and similarly for other Bessel functions. We have also introduced $\omega_{Ae} = kC_{Ae}$ and $\omega_{A0} = kC_{A0}$, as the frequencies associated with the Alfvén speeds of the system. We use the same definitions

of m_e and n_0 as before, but in the zero-β limit $C_s = 0$.

$$m_e^2 = \frac{k^2 C_{Ae}^2 - \omega^2}{C_{Ae}^2}, \quad n_0^2 = -\frac{k^2 C_{A0}^2 - \omega^2}{C_{A0}^2}. \tag{3.2}$$

A solution to (3.1) is already known from considering Fig. 1.7, that is that at $k = k_c$, the cutoff wavenumber, $\omega/k = C_{Ae}$. Around this point m_e is small, and therefore K_0 and K_1 can be expanded using their expansion for small arguments [Abramowitz et al., 1988]

$$K_0(m_e d) = -\ln\left(\frac{1}{2} m_e d\right), \quad K_1(m_e d) = \frac{1}{m_e d},$$

substituting these, and replacing ρ_0/ρ_e with C_{Ae}^2/C_{A0}^2 (3.1) becomes:

$$\frac{C_{Ae}^2}{C_{A0}^2} \frac{(\omega^2 - \omega_{A0}^2)}{(\omega^2 - \omega_{Ae}^2)} \frac{m_e}{n_0} = \frac{J_1(n_0 d)}{J_0(n_0 d)} m_e d \ln\left(\frac{1}{2}(m_e d)\right), \tag{3.3}$$

from this it can be shown that $J_0(n_0 d) = 0$ when $k = k_c$, or using the definition of n_0 from (3.2):

$$k_c d = \frac{C_{A0} j_{0,1}}{\sqrt{C_{Ae}^2 - C_{A0}^2}} = \frac{j_{0,1}}{D}, \tag{3.4}$$

where $j_{0,1}$ is the first zero of the Bessel function J_0 and D is a factor that depends on the density contrast ratio:

$$D^2 = \frac{C_{Ae}^2}{C_{A0}^2} - 1 = \frac{\rho_0}{\rho_e} - 1 = \xi - 1.$$

Here we have also used the notation $\xi = \rho_0/\rho_e$ as first introduced in Van Doorsselaere et al. [2004].

3.2.2 Leaky regime in the neighbourhood of the cutoff wavenumber.

There are several regions where an approximate solution to the dispersion relation can be found. The first that will be considered is in the leaky regime in the neighbourhood of k_c. In Fig. 2.4 this is the region just to the right of the thick solid line. In this region the dispersion relation (3.1) no longer holds, as now the exterior solution is a propagating wave. Instead the following dispersion relation is used:

$$\frac{\rho_0}{\rho_e} \frac{(\omega_{A0}^2 - \omega^2)}{(\omega_{Ae}^2 - \omega^2)} \frac{n_e}{n_0} = \frac{J_1(n_0 d)}{J_0(n_0 d)} \frac{H_0^{(2)}(n_e d)}{H_1^{(2)}(n_e d)}, \tag{3.5}$$

where $H_m^{(2)}(n_e r) = J_m(n_e r) - iY_m(n_e r)$ is the outwardly propagating wave solution. In the zero-β case again we have:

$$n_e^2 = -\frac{k^2 C_{Ae}^2 - \omega^2}{C_{Ae}^2}.$$

We are only interested in the regime surrounding the cutoff, therefore we re-write $\omega = \omega_{Ae} + \Delta\omega$ and $k = k_c + \Delta k$, where $\Delta\omega$ and Δk are both considered small quantities. Substituting these into the forms of n_e and n_0 and neglecting terms with $(\Delta\omega)^2$ and $(\Delta k_c)^2$ we get:

$$n_e^2 = \left(\frac{\omega_{Ae}^2 + 2\omega_{Ae}\Delta\omega - C_{Ae}^2 k_c^2 - 2k_c C_{Ae}^2 \Delta k}{C_{Ae}^2} \right), \tag{3.6}$$

$$n_0^2 = \left(\frac{\omega_{Ae}^2 + 2\omega_{Ae}\Delta\omega - C_{A0}^2 k_c^2 - 2k_c C_{A0}^2 \Delta k}{C_{A0}^2} \right). \tag{3.7}$$

The expression for n_e can be simplified with use of $\omega_{Ae} = C_{Ae} k_c$, which gives:

$$n_e = \sqrt{\frac{2\Delta e}{C_{Ae}^2}}, \tag{3.8}$$

where

$$\Delta e = \omega_{Ae}^2 \left(\frac{\Delta\omega}{\omega_{Ae}} - \frac{\Delta k}{k_c} \right).$$

Then substituting $\omega_{Ae} = C_{Ae} k_c$ into the expression for n_0, and factoring out the terms containing the small parameters gives:

$$n_0 = k_c D(1 + \Delta s), \tag{3.9}$$

where

$$\begin{aligned} \Delta s &= \frac{C_{Ae} k_c \Delta\omega - k_c C_{A0}^2 \Delta k}{(C_{Ae}^2 - C_{A0}^2)^2 k_c^2} \\ &= \frac{1}{D^2} \left(\xi \frac{\Delta\omega}{\omega_{Ae}} - \frac{\Delta k}{k_c} \right). \end{aligned}$$

These expressions can then be substituted into (3.5) to give the dispersion relation around the cutoff wavenumber. We also use the fact that the argument of the Bessel J function now

consists of a large and a small parameter to perform a Taylor expansion of these. We obtain:

$$C_{Ae}^2 \frac{k_c^2 D^2 (1 + 2\Delta s)}{2\Delta e} \frac{\sqrt{\frac{2\Delta e}{C_{Ae}^2}}}{k_c D (1 + \Delta s)} =$$

$$-\left(\frac{J_0(k_c dD) - J_2(k_c dD)}{J_1(k_c dD)} + \frac{J_1(k_c dD)}{(k_c dD) J_1(k_c dD)\Delta s} \right) \frac{H_0^{(2)}\left(d\sqrt{\frac{2\Delta e}{C_{Ae}^2}} \right)}{H_1^{(2)}\left(d\sqrt{\frac{2\Delta e}{C_{Ae}^2}} \right)}. \qquad (3.10)$$

Using the fact that $k_c dD$ was shown to be a zero of J_0 in the previous section, as well as simplifying gives:

$$C_{Ae} D \frac{k_c(1 + \Delta s)}{\sqrt{2\Delta e}} = -\left(-\frac{J_2(k_c dD)}{J_1(k_c dD)} + \frac{1}{(k_c dD)\Delta s} \right)$$

$$\times \left\{ \frac{J_0\left(d\sqrt{\frac{2\Delta e}{C_{Ae}^2}} \right) - iY_0\left(d\sqrt{\frac{2\Delta e}{C_{Ae}^2}} \right)}{J_1\left(d\sqrt{\frac{2\Delta e}{C_{Ae}^2}} \right) - iY_1\left(d\sqrt{\frac{2\Delta e}{C_{Ae}^2}} \right)} \right\}. \qquad (3.11)$$

We use the expansions for the Bessel and Hankel functions [Abramowitz et al., 1988]

$$J_0(n_e d) = 1 - \frac{1}{4}\left(d^2 \frac{2\Delta e}{C_{Ae}^2} \right),$$

$$J_1(n_e d) = \frac{1}{2}\left(d\sqrt{\frac{2\Delta e}{C_{Ae}^2}} \right),$$

$$Y_0(n_e d) = \frac{2}{\pi} \ln\left(\frac{1}{2} d\sqrt{\frac{2\Delta e}{C_{Ae}^2}} \right)$$

$$Y_1(n_e d) = -\frac{2}{\pi d\sqrt{\frac{2\Delta e}{C_{Ae}^2}}},$$

and substitute them in equation (3.11). We neglect higher order terms to obtain

$$-C_{Ae} D^2 k_c^2 d\left(\frac{1}{2} d\sqrt{\frac{2\Delta e}{C_{Ae}^2}} + i\frac{2C_{Ae}}{\pi d\sqrt{2\Delta e}} \right) \Delta s$$

$$= \sqrt{2\Delta e}\left[1 - \frac{i}{\pi} \ln\left(\frac{d^2 \Delta e}{2C_{Ae}^2} \right) \right]. \qquad (3.12)$$

46

In order to eliminate Δe in the denominator of the left hand side of equation (3.12), we multiply both sides by $\sqrt{2\Delta e}$, and therefore we obtain

$$-C_{Ae}D^2\left(\frac{d\Delta e}{C_{Ae}^2} + i\frac{2C_{Ae}}{\pi d}\right)\Delta s$$
$$= \frac{2\Delta e}{k_c^2 d}\left[1 - \frac{i}{\pi}\ln\left(\frac{d^2\Delta e}{2C_{Ae}^2}\right)\right]. \tag{3.13}$$

We substitute the expression for Δs and Δe to obtain

$$\left\{1 + i\frac{C_{Ae}^2}{\pi C_{A0}^2} - \frac{i}{\pi}\ln\left[\frac{k_c^2 d^2}{2}\left(\frac{\Delta\omega}{\omega_{Ae}} - \frac{\Delta k}{k_c}\right)\right]\right\}\frac{\Delta\omega}{\omega_{Ae}}$$
$$= \left\{1 + \frac{i}{\pi} - \frac{i}{\pi}\ln\left[\frac{k_c^2 d^2}{2}\left(\frac{\Delta\omega}{\omega_{Ae}} - \frac{\Delta k}{k_c}\right)\right]\right\}\frac{\Delta k}{k_c}. \tag{3.14}$$

This provides an implicit and complex dispersion relation, describing the complex frequency, ω. Here the real part of ω describes the frequency and the imaginary component the decay rate. To proceed we must separate the real and imaginary parts of (3.14). To separate logarithms with complex arguments we use the identity: $\ln(x + iy) = (1/2)\ln(x^2 + y^2) + i\arctan(y/x)$. Applying this identity to the logarithm in (3.14) gives:

$$\ln\left\{\frac{k_c^2 d^2}{2}\left(\frac{\Delta\omega}{\omega_{Ae}} - \frac{\Delta k}{k_c}\right)\right\} = i\arctan\left(\frac{\Im(\Delta\omega)}{\Re(\Delta\omega) - C_{Ae}\Delta k}\right)$$
$$+\frac{1}{2}\ln\left\{\left(\frac{k_c^2 d^2}{2}\right)^2\left[\left(\frac{\Re(\Delta\omega)}{\omega_{Ae}} - \frac{\Delta k}{k_c}\right)^2 + \left(\frac{\Im(\Delta\omega)}{\omega_{Ae}}\right)^2\right]\right\}. \tag{3.15}$$

In (3.15) the arctan term can be neglected as compared to the logarithmic term as we are comparing the logarithm of a small quantity to a term linear in this small quantity, hence we can define the argument of the logarithm as:

$$\Delta W = \left(\frac{k_c^2 d^2}{2}\right)^2\left\{\left(\frac{\Re(\Delta\omega)}{\omega_{Ae}} - \frac{\Delta k}{k_c}\right)^2 + \left(\frac{\Im(\Delta\omega)}{\omega_{Ae}}\right)^2\right\}, \tag{3.16}$$

which allows us to write (3.14):

$$\frac{\Delta\omega}{\Delta k} = C_{Ae}\left[1 + \frac{i}{\pi} - \frac{i\ln(\Delta W)}{2\pi}\right]$$
$$\times\left[1 + \frac{iC_{Ae}^2}{\pi C_{A0}^2} - \frac{i\ln(\Delta W)}{2\pi}\right]^{-1}. \tag{3.17}$$

In order to make the denominator of (3.17) real, so it can be separated into real and imaginary terms, we multiply the numerator and denominator by the denominator's complex conjugate:

$$
\begin{aligned}
\frac{\Delta\omega}{\Delta k} =& C_{Ae}\Bigg[1 + \frac{C_{Ae}^2}{\pi^2 C_{A0}^2} - \frac{C_{Ae}^2}{2\pi^2 C_{A0}^2}\ln(\Delta W) \\
& + \frac{1}{4\pi^2}(\ln(\Delta W))^2 + \frac{i}{\pi} - i\frac{C_{Ae}^2}{\pi C_{A0}^2}\Bigg] \\
& \times \Bigg[1 + \frac{C_{Ae}^4}{\pi^2 C_{A0}^4} + \frac{1}{4\pi^2}(\ln(\Delta W))^2 - \frac{C_{Ae}^2}{\pi^2 C_{A0}^2}\ln(\Delta W)\Bigg]^{-1}.
\end{aligned} \tag{3.18}
$$

Note that the term $(1/2\pi^2)\ln(\Delta E)$ has been neglected in comparison to the term $(1/4\pi^2)[\ln(\Delta W)]^2$ when obtaining equation (3.18), because we assume that $|\Delta\omega| \ll 1$. This neglection is based on the fact that the arguments of the logarithms are small so that the absolute value of the logarithm is large. Hence the square of the logarithm would be much greater than the logarithm itself.

Finally, the dependence of the sausage mode frequency and the damping rate on the wave number could be defined by two coupled implicit equations as:

$$
\begin{aligned}
\frac{\mathfrak{R}(\Delta\omega)}{\Delta k} =& C_{Ae}\Bigg[1 + \frac{C_{Ae}^2}{\pi^2 C_{A0}^2} - \frac{C_{Ae}^2\ln(\Delta W)}{2\pi^2 C_{A0}^2} + \frac{(\ln(\Delta W))^2}{4\pi^2}\Bigg] \\
& \times \Bigg[1 + \frac{C_{Ae}^4}{\pi^2 C_{A0}^4} + \frac{(\ln(\Delta W))^2}{4\pi^2} - \frac{C_{Ae}^2\ln(\Delta W)}{\pi^2 C_{A0}^2}\Bigg]^{-1},
\end{aligned} \tag{3.19}
$$

$$
\begin{aligned}
\frac{\mathfrak{I}(\Delta\omega)}{\Delta k} =& -\frac{C_{Ae}}{\pi}\Bigg[\frac{C_{Ae}^2}{C_{A0}^2} - 1\Bigg] \\
& \times \Bigg[1 + \frac{C_{Ae}^4}{\pi^2 C_{A0}^4} + \frac{(\ln(\Delta W))^2}{4\pi^2} - \frac{C_{Ae}^2\ln(\Delta W)}{\pi^2 C_{A0}^2}\Bigg]^{-1},
\end{aligned} \tag{3.20}
$$

for the frequency and damping rate, respectively. This set of equations is implicit and can be solved numerically.

These equations are however still coupled, and as such further assumptions are required to reach a more useful form. In particular we are assuming a high density contrast. This solution may be relevant for high density contrast jets [Cirtain et al., 2007], for very dense coronal loops, and for chromospheric structures (where Morton et al. [2011] recently measured the cutoff wavenumber for sausage modes). To proceed we simplify the expressions for the frequency and damping rate (3.19) and (3.20), by assuming $\rho_e/\rho_0 = (C_{Ae}^2/C_{A0}^2)^{-1} \ll 1$ and

then neglecting terms without C_{Ae}^2/C_{A0}^2, or C_{Ae}^4/C_{A0}^4 in the denominator. This gives:

$$\frac{\Re(\Delta\omega)}{\Delta k} \approx \frac{C_{A0}^2}{C_{Ae}}\left\{1 - \frac{1}{2}\ln\left[\frac{k_c^4 d^4}{4}\left(\left[\frac{\Re(\Delta\omega)}{\omega_{Ae}} - \frac{\Delta k}{k_c}\right]^2\right.\right.\right.$$
$$\left.\left.\left.+ \left[\frac{\pi C_{A0}^2}{C_{Ae}^2}\frac{\Delta k}{k_c}\right]^2\right)\right]\right\}, \tag{3.21}$$

and

$$\frac{\Im(\Delta\omega)}{\Delta k} = -\frac{\pi C_{A0}^2}{C_{Ae}}, \tag{3.22}$$

for the frequency and the damping rates, respectively. Note that the decay rate is calculated first, and is then substituted into the form of the frequency to simplify (3.19). We can check that the decay rate is sensible, as the right hand side of (3.22) is always negative. Hence we only have a positive decay rate for a negative Δk, that is a wavenumber smaller than the cutoff value.

It is also useful to formulate a definition for the phase speed of these oscillations. To do this first the phase speed is defined in a similar manner to the previous parameters: $V = C_{Ae} + \Delta V$, ΔV is then related to $\Delta\omega$ and Δk by:

$$\frac{\Delta\omega}{\Delta k} = k_c\frac{\Delta V}{\Delta k} + C_{Ae}. \tag{3.23}$$

Substituting this into (3.21) gives:

$$\frac{\Re(\Delta V)}{\Delta k} \approx \frac{C_{A0}^2}{k_c C_{Ae}} - \frac{C_{Ae}}{k_c}$$
$$- \frac{C_{A0}^2}{2k_c C_{Ae}}\ln\left\{\frac{k_c^4 d^4}{4}\left(\left[\frac{\Re(\Delta V)}{C_{Ae}}\right]^2 + \left[\frac{\pi C_{A0}^2}{C_{Ae}^2}\frac{\Delta k}{k_c}\right]^2\right)\right\}. \tag{3.24}$$

Then as $(C_{Ae}^2/C_{A0}^2) \gg 1$ we neglect terms with C_{A0}^2, which leaves:

$$\frac{\Re(\Delta V)}{\Delta k} \approx -\frac{C_{Ae}}{k_c}. \tag{3.25}$$

3.2.3 Leaky regime in the long wavelength limit

It is also of interest to find a similar expansion in the long wavelength limit. To do this first we consider the dispersion relation in the case $k = 0$:

$$\frac{\rho_0}{\rho_e}\frac{(\omega_{A0}^2 - \omega_0^2)}{(\omega_{Ae}^2 - \omega_0^2)}\frac{n_e}{n_0} = \frac{J_1(n_0 d)H_0^{(2)}(n_e d)}{J_0(n_0 d)H_1^{(2)}(n_e d)}, \tag{3.26}$$
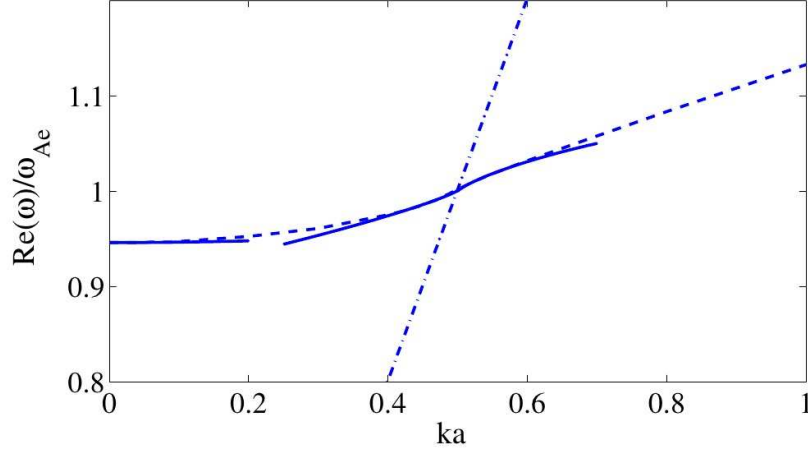
Figure 3.1: The frequency dependence of the sausage oscillation on the wavenumber. The solid lines are the analytical expression derived in the long wavelength limit and around the cutoff. The dashed line is the results obtained from the numerical model. The dot-dashed line represents the external Aflvén speed, and therefore demonstrates the cutoff. The density ratio was taken to be $\rho_0/\rho_e = C_{Ae}^2/C_{A0}^2 = 25$. All frequencies have been normalised by the external Alfvén frequency at the cutoff.

here, $\omega_0 = \omega(k = 0)$ the frequency in the long wavelength limit, as in section 2.3 we showed that the real part of this asymptotically approaches a constant value for small values of k. As in section 3.2.2 we assume that the frequency and wavenumber are constants plus a small perturbation from this point. Performing the expansion as before yields:

$$
\frac{C_{Ae}(1 + \frac{\Delta A}{2})}{C_{A0}(1 + \frac{\Delta Ae}{2})} = \frac{\left[J_1\left(\frac{\omega_0 d}{C_{A0}}\right) + \frac{\omega_0 d}{2C_{A0}}\left(J_0\left(\frac{\omega_0 d}{C_{A0}}\right) - J_2\left(\frac{\omega_0 d}{C_{A0}}\right)\right)\Delta A\right]}{\left[J_0\left(\frac{\omega_0 d}{C_{A0}}\right) - \frac{\omega_0 d}{C_{A0}}J_1\left(\frac{\omega_0}{C_{A0}}d\right)\Delta A\right]}
$$
$$
\times \left[J_0\left(\frac{\omega_0 d}{C_{Ae}}\right) - \frac{\omega_0 d}{C_{Ae}}J_1\left(\frac{\omega_0 d}{C_{Ae}}\right)\Delta Ae - iY_0\left(\frac{\omega_0 d}{C_{Ae}}\right)\right.
$$
$$
+ i\frac{\omega_0 d}{C_{Ae}}Y_1\left(\frac{\omega_0 d}{C_{Ae}}\right)\Delta Ae\right]\left[J_1\left(\frac{\omega_0 d}{C_{Ae}}\right)\right.
$$
$$
+ \frac{\omega_0 d}{2C_{Ae}}\left\{J_0\left(\frac{\omega_0 d}{C_{Ae}}\right) - J_2\left(\frac{\omega_0 d}{C_{Ae}}\right)\right\}\Delta Ae - iY_1\left(\frac{\omega_0 d}{C_{Ae}}\right)
$$
$$
- i\frac{\omega_0 d}{2C_{Ae}}Y_0\left(\frac{\omega_0 d}{C_{Ae}}\right)\Delta Ae + i\frac{\omega_0 d}{2C_{Ae}}Y_2\left(\frac{\omega_0 d}{C_{Ae}}\right)\Delta Ae\right]^{-1}, \qquad (3.27)
$$

where

$$
\Delta Ae = \frac{2\omega_0\Delta\omega - C_{Ae}^2(\Delta k)^2}{\omega_0^2}, \quad \Delta A = \frac{2\omega_0\Delta\omega - C_{A0}^2(\Delta k)^2}{\omega_0^2}. \qquad (3.28)
$$

50

This is a fairly unwieldy equation, and therefore further assumptions will have to be made to simplify it. Firstly we consider the zeroth order approximation, that is to neglect all terms containing small parameters. This leaves:

$$\frac{C_{Ae}}{C_{A0}} = \frac{J_1\left(\frac{\omega_0 d}{C_{A0}}\right)}{J_0\left(\frac{\omega_0 d}{C_{A0}}\right)} \times \frac{J_0\left(\frac{\omega_0 d}{C_{Ae}}\right) - iY_0\left(\frac{\omega_0 d}{C_{Ae}}\right)}{J_1\left(\frac{\omega_0 d}{C_{Ae}}\right) - iY_1\left(\frac{\omega_0 d}{C_{Ae}}\right)}. \tag{3.29}$$

This is very useful, as it allows us to find the value of ω_0 for a given C_{Ae} and C_{A0}. As with the case in the vicinity of the cutoff we can proceed by assuming a high density contrast ratio. We multiply out the fractions in (3.27) and neglect terms which are linear or higher in ρ_e/ρ_0. This gives

$$\frac{1}{2}J_0\left(\frac{\omega_0 d}{C_{A0}}\right)J_0\left(\frac{\omega_0 d}{C_{Ae}}\right)\Delta Ae$$
$$-\frac{C_{Ae}}{C_{A0}}J_1\left(\frac{\omega_0 d}{C_{A0}}\right)J_1\left(\frac{\omega_0 d}{C_{Ae}}\right)\Delta A$$
$$+i\frac{C_{Ae}}{C_{A0}}J_1\left(\frac{\omega_0 d}{C_{A0}}\right)Y_1\left(\frac{\omega_0 d}{C_{Ae}}\right)\Delta A = 0. \tag{3.30}$$

We then use the limiting expressions for the Bessel functions:

$$J_0 = 1 - \frac{(\omega_0 d)^2}{4C_{A0,e}^2}, \quad J_1 = \frac{1}{2}\frac{\omega_0 d}{C_{A0,e}}, \quad Y_1 = -\frac{2C_{Ae}}{\pi\omega_0}, \tag{3.31}$$

and the definitions of ΔA and ΔAe, which gives:

$$\left(\omega_0 - \frac{3\omega_0^3 d^2}{4C_{A0}^2} + \frac{\omega_0^5 d^4}{16C_{A0}^2 C_{Ae}^2} - i\frac{2C_{Ae}^2\omega_0}{\pi C_{A0}^2}\right)\Delta\omega$$
$$= \left(\frac{1}{2}C_{Ae}^2 - \frac{\omega_0^2 d^2 C_{Ae}^2}{8C_{A0}^2} + \frac{\omega_0^4 d^4}{32C_{A0}} - i\frac{C_{Ae}^2}{\pi}\right)(\Delta k)^2. \tag{3.32}$$

We then consider the solutions to (3.29), to find values for ω_0. For some wave guiding structures the imaginary part of ω_0 is much smaller than the real part. This means that even in the long wavelength limit the oscillations have a reasonably high quality. This agrees with our findings in section 2.3, the thin long dashed line in Fig. 2.4 shows where oscillations have a quality factor below 3, and for cylinders with a reasonably high density contrast ratio the dispersion curve never reaches this line. This fact aids in the following analysis, as it means the imaginary part of ω_0 can be neglected with regards to the real part.

Hence (3.32) simplifies to:

$$\frac{\Delta\omega}{(\Delta k)^2} = \left(\frac{C_{Ae}^2}{2} - \frac{(\Re(\omega_0))^2 d^2 C_{Ae}^2}{8 C_{A0}^2} - i \frac{C_{Ae}^2}{\pi} \right)$$
$$\times \left(\Re(\omega_0) - \frac{3d^2}{4C_{A0}^2}(\Re(\omega))^3 - i \frac{2C_{Ae}^2}{\pi C_{A0}^2}\Re(\omega_0) \right)^{-1}, \qquad (3.33)$$

As before the denominator is made real by multiplying the numerator and the denominator by the denominator's complex conjugate. This then allows the real and imaginary parts to be separated, giving:

$$\frac{\Re(\Delta\omega)}{(\Delta k)^2} = \frac{\pi^2 C_{A0}^4}{8 C_{Ae}^2 \Re(\omega_0)} \left(1 + \frac{4 C_{Ae}^2}{\pi^2 C_{A0}^2} - \frac{(\Re(\omega))^2 d^2}{C_{A0}^2} \right). \qquad (3.34)$$

and

$$\frac{\Im(\Delta\omega)}{(\Delta k)^2} = \left(\frac{\pi C_{A0}^2}{4 C_{Ae}^2 \Re(\omega_0)} \right)$$
$$\times \left(C_{Ae}^2 - \frac{C_{Ae}^2 (\Re(\omega_0))^2 d^2}{4 C_{A0}^2} + \frac{3(\Re(\omega_0))^2 d^2}{4} \right). \qquad (3.35)$$

3.2.4 Non-leaky regime in the vicinity of the cutoff frequency

The final region in which an approximation will be derived is in the vicinity of the cutoff, but in the trapped regime. To start we refer back to the dispersion relation in this regime (3.1). We then proceed in the same manner as in the weakly leaky regime, introducing $\Delta\omega$ and Δk as small parameters from the known point (ω_{Ae}, k_c), and use Taylor expansions for the Bessel functions about this point, which gives:

$$C_{Ae}^2 \frac{D^2 k_c^2 (1 + 2\Delta s)}{(-2\Delta e)} \frac{\sqrt{\frac{-2\Delta e}{C_{Ae}^2}}}{k_c D(1 + \Delta s)}$$
$$= \left(\frac{J_0(k_c dD) - J_2(k_c dD)}{J_1(k_c dD)} + \frac{J_1(k_c dD)}{(k_c dD)J_1(k_c dD)\Delta s} \right)$$
$$\times \frac{K_0 \left(d \sqrt{\frac{-2\Delta e}{C_{Ae}^2}} \right)}{K_1 \left(d \sqrt{\frac{-2\Delta e}{C_{Ae}^2}} \right)}. \qquad (3.36)$$

Further simplification, and the neglect of small terms in the high density contrast regime leads to:

$$\frac{\Delta\omega}{\Delta k} \approx -\frac{C_{A0}^2}{C_{Ae}} \ln \left(\frac{k_c^2 d^2}{2} \left| \frac{\Delta\omega}{\omega_{Ae}} - \frac{\Delta k}{k_c} \right| \right). \qquad (3.37)$$
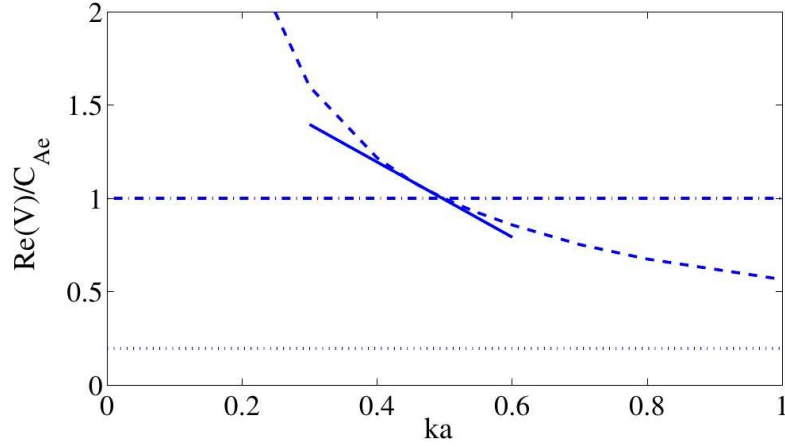
Figure 3.2: The phase speed dependence of the sausage oscillation on the wavenumber. The solid lines are the analytical expression derived around the cutoff. The dashed line is the results obtained from the numerical model. The dotted and dot-dashed line represents the internal and external Aflvén speeds respectively. The density ratio was taken to be $\rho_0/\rho_e = C_{Ae}^2/C_{A0}^2 = 25$. All speed have been normalised by the external Alfvén speed.

As well as showing that the imaginary part of the frequency is zero, i.e. the oscillation is not damped.

3.3 Comparison with numerical simulations

Thus we derived analytical asymptotic approximations for the frequency of the sausage mode in three regions, either side of the cutoff, and in the long wavelength limit, as well as the damping rate for the two regions in the leaky regime. This therefore then allows us to compare these solutions to the numerical model developed in section 2.2.

Fig. 3.1 shows the variation in the real component of frequency with wavenumber, both for the analytical expressions in the regions in which they were derived, and the numerical results obtained using the method described in section 2.2. There is a good agreement between the numerical and analytical results both around the cutoff (where the dashed and solid lines intersect the dot-dashed line), and in the very leaky regime.

We also used (3.24), the expression for the phase speed around the cutoff, to compare the phase speed variation with the numerical case, as shown in Fig. 3.2. Again there is a good agreement between the analytical and numerical cases. For both these plots we used a density contrast ratio, $\rho_0/\rho_e = 25$, allowing us to use the assumption of a high density contrast ratio.
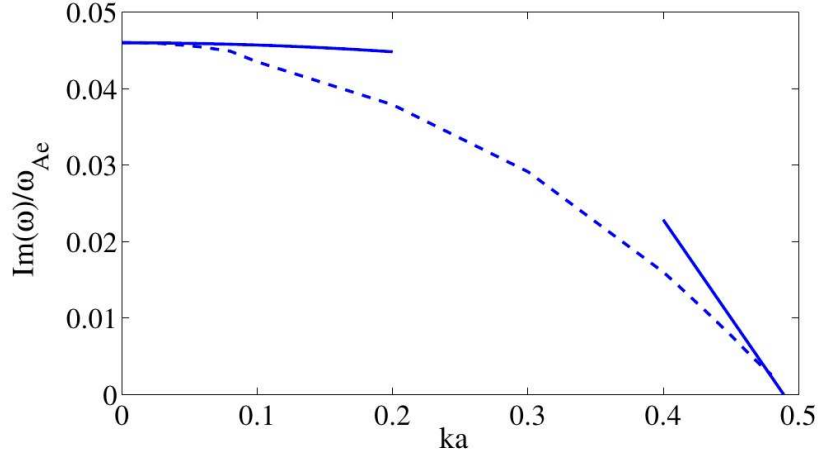
Figure 3.3: The decay rate dependence of the sausage oscillation on the wavenumber. The solid lines are the analytical expression derived in the long wavelength limit and in the weakly leaky regime. The dashed line is the results obtained from the numerical model. The density ratio was taken to be $\rho_0/\rho_e = C_{Ae}^2/C_{A0}^2 = 25$. The damping has been normalised by the external Alfvén frequency at the cutoff.

Finally we considered the damping rate of these oscillations, given by (3.22), this is shown in Fig. 3.3. In order to calculate the damping rate of oscillations from our numerical model we fit the peaks of the oscillation with a decaying exponential and use its decay rate as the damping rate of the oscillation. There is a good agreement between the analytical results in both the weakly and strongly leaky regimes.

3.4 Conclusions

In this chapter we have developed analytical asymptotic expressions for the real and imaginary parts of the dispersion relation for sausage oscillations in three regions: the weakly trapped, weakly leaky and strongly leaky regimes. This is the same dispersion relation as considered in Chapter 2, where the oscillations were modelled, and a modelled solutions to the dispersion curve was deduced. The results of this can be summarised as follows:

1. The analytical solutions for the real component of ω derived in this chapter were then compared with the values for ω obtained from the numerical model developed in chapter 2. A good agreement was found between these two in all considered regions.

2. The model developed in Chapter 2 was extended to also consider the decay rate of

these oscillations in the leaky region.

3. The modelled decay rate was compared with the imaginary component of ω in the leaky regions that were considered using the analytical expansion. A good match was found between these quantities.

Chapter 4

Sausage oscillations of a slab geometry

4.1 Introduction

The work presented in this chapter is based on Hornsey et al. [2014]. In chapter 2 a numerical model for the sausage oscillation of a plasma cylinder was considered. However the sausage oscillation is not purely restricted to the cylindrical geometry, a sausage oscillation can also appear in a slab geometry. The underlying mathematics is very similar to the cylindrical case and was performed for a step-function profile by Edwin and Roberts [1982]. Indeed, in a number of cases the waveguiding coronal plasma non-uniformity is better described by a plane or curved slab than a cylinder. In particular, sausage perturbations can readily occur in coronal streamers and other current sheets [e.g. Smith et al., 1997], in dark lanes in post-flare supra-arcades [e.g. Verwichte et al., 2005; Costa, 2011], and global oscillations of prominence slabs. Sausage modes in this geometry have also been used to explain various phenomena that have been observed in the corona. For example, Scott et al. [2013] developed a model to explain the observed EUV emission of the large vertical fans above arcades. Their model involves a travelling sausage oscillation descending down a flaring current sheet. This movement triggers peristaltic pumping, or a flow inside the sheet causing by these axi-symmetric oscillations, which could lead to chromospheric evaporation which fills the supra arcade fans with the hot plasma required to emit the EUV emission that is observed.

Another example of sausage oscillations being used to explain observations is provided by Karlický et al. [2013] who studied radio fibre bursts. They compared radio spectra of these events with artificial ones generated using a semi-emperical model and a MHD model of a sausage mode in a flaring current sheet. They found a good agreement between observa-

tions and their models and hence considered sausage oscillation in current sheets to be an excellent candidate to explain this phenomena.

The aim of this chapter is to generalise the results obtained in the previous chapter and Nakariakov et al. [2012] on the slab geometry. We also aim to develop the work of Pascoe et al. [2007a] on the case of long wavelengths, studying the transition between trapped and leaky regimes, and comparison of the results obtained in both the geometries. The chapter is organised as follows. Section 4.2.1 describes the model that was used to describe these oscillations in the slab geometry. Section 4.2.2 details the results of measurements made using this model, firstly studying how the period of the oscillations varies with the wavenumber for different shapes and depths of well, as well as how these values compare to the cylindrical case. Then the effect of varying the steepness of the well was considered in depth. Finally in this section the values of the cutoff wavelength, that is the value of the wavelength for which the oscillation transitions for being trapped to being leaky, were studied, and compared with analytical results in the case of an infinitely steep well. Section 4.2.3 summarises the conclusions.

4.2 Slab

4.2.1 Model

Consider a slab of a zero-β plasma of infinite extent in the x-direction. The plasma is penetrated by a straight and uniform magnetic field, $\mathbf{B_0}$ directed along the x axis. Here, the index "0" denotes the equilibrium quantities. The equilibrium density, ρ_0, is

$$\rho_0 = \frac{4\pi B_0^2}{C_{A\infty}^2}\left[1 - \delta \exp\left(-\left(\frac{|z|}{d}\right)^\alpha\right)\right]^{-2}, \tag{4.1}$$

and the Alfvén speed, $C_A(z)$, obeys

$$C_A(z) = C_{A\infty}\left[1 - \delta \exp\left(-\left(\frac{|z|}{d}\right)^\alpha\right)\right], \tag{4.2}$$

where $C_{A\infty}$ is the Alfvén speed at a large distance from the slab, where d is the slab half-width, the parameter $0 < \delta < 1$ controls the value of the Alfvén speed at the centre of the slab, and the parameter α controls the steepness of the profile of the Alfvén speed. This is the same Alfvén speed profile as considered in the cylindrical case (see chapter 2). This allows a direct comparison of the results obtained in the cylindrical and slab geometries. There are no steady flows in the considered equilibrium. The use of the zero-β limit is justified by the previous numerical experiments that showed that properties of sausage oscillations are practically independent of β, provided it is lower than unity [Inglis et al.,

2009]. As β is taken to zero, profile (4.2) of the Alfvén speed coincides with the profile of the fast magnetoacoustic speed, $C_{\text{FastMode}} = (C_A^2 + C_s^2)^{1/2} \approx C_A$, where the sound speed, C_s is neglected in comparison with the Alfvén speed. Thus, the slab has a decrease in the fast magnetoacoustic speed and hence can act as a fast magnetoacoustic waveguide [Nakariakov and Roberts, 1995]. As the propagation of fast magnetoacoustic waves is not sensitive to whether the magnetic field is directed in the positive or negative direction along the x-axis in the considered geometry, our model is also applicable to infinitely thin current sheets situated at $z = 0$ and embedded in a plasma slab.

In the following we restrict ourselves to considering ideal processes only, described by the ideal zero-β MHD equations, these are:

$$\rho \frac{\partial \mathbf{v}}{\partial t} = -\frac{1}{\mu_0} \left[\mathbf{B} \times (\nabla \times \mathbf{B}) \right], \tag{4.3}$$

$$\frac{\partial \mathbf{B}}{\partial t} = \nabla \times (\mathbf{v} \times \mathbf{B}), \tag{4.4}$$

where the notations are standard. The mass continuity and energy equations that are not needed for this study, are not shown.

We then proceed in a similar manner to the cylindriucal case, by assuming small perturbations to the equilibrium quantities, denoted by an index, 1, then linearising the equations we obtain:

$$\rho_0 \frac{\partial \mathbf{v_1}}{\partial t} = -\frac{1}{\mu_0} \left[\mathbf{B_0} \times (\nabla \times \mathbf{B_1}) \right], \tag{4.5}$$

$$\frac{\partial \mathbf{B_1}}{\partial t} = \nabla \times (\mathbf{v_1} \times \mathbf{B_0}). \tag{4.6}$$

For the components of the vector quantities we obtain the equations

$$\frac{\mu_0 \rho_0}{B_0} \frac{\partial v_z}{\partial t} = \frac{\partial B_x}{\partial z} - \frac{\partial B_z}{\partial x}, \tag{4.7}$$

$$\frac{\partial B_x}{\partial t} = -B_0 \frac{\partial v_z}{\partial z}, \tag{4.8}$$

$$\frac{\partial B_z}{\partial t} = -B_0 \frac{\partial v_z}{\partial x}. \tag{4.9}$$

Differentiating Eq. (4.7) by t, Eq. (4.8) by x and Eq. (4.9) by z, eliminating the variables B_z and B_x, and assuming that the perturbations are periodic in the x-direction with the wavelength $2\pi/k_x$, we obtain

$$C_A^{-2}(z) \frac{\partial^2 v_z}{\partial t^2} - \frac{\partial^2 v_z}{\partial z^2} + k_x^2 v_z = 0. \tag{4.10}$$

Equation (4.10) is a 1D wave equation describing the evolution of fast magnetoacoustic oscillations of a given longitudinal wavelength $2\pi/k_x$ in the transverse direction, in a field-aligned zero-β plasma slab with a smooth transverse profile of the plasma density. This equation is a Cartesian analogue of Eq. (2.6).

The Fourier transform in the x-direction, made in the derivation of Eq. (4.10) is possible if the slab is uniform in the x-direction. This condition corresponds to the assumption that the wavelength of the perturbations is shorter than the non-uniformity along the magnetic field (e.g. the density scale height in the case of the vertical slab representing the stalk of a helmet streamer). Also, the slab is assumed to be uniform in the third, y-direction, that is perpendicular to both the magnetic field and the plasma density non-uniformity gradient. This allows us to assume the perturbations to be independent of the y-direction. These assumptions are standard in modelling plasma non-uniformities in the solar corona, e.g. current sheets in helmet streamers and above post-flaring arcades.

A parametric study of an initial value problem for Eq. (4.10) was performed numerically using the *pdsolve* function of *Maple 16* that implements a second order (in space and time) centred finite difference scheme (see chapter 2 for details) The initial conditions were chosen to be an impulsive anti-symmetric pulse centred at the axis of the slab,

$$ v_z(z, t = 0) = A_0 z \exp\left[-\left(\frac{z}{d}\right)^2\right], \tag{4.11}$$

where A_0 is the initial amplitude. The symmetry of the initial perturbation excludes the excitation of kink oscillations. All the energy of the initial pulse goes to sausage oscillations. As the initial pulse does not coincide with eigen functions of the slab, it can excite a number of transverse harmonics. However, as function (4.11) decreases monotonically with the increase in the distance from the slab central plane, the fundamental mode that has a similar structure is excited much more effectively than higher transverse harmonics. In the simulations the higher harmonics are practically absent. The boundary conditions were set as

$$ v_z(z = 0, t) = 0, \quad v_z(z = 50d, t) = A_0 z \exp\left(-(50d)^2\right), \tag{4.12}$$

where $z = 50d$ is the transverse extent of the simulation domain. This value for the boundary condition was chosen so as there would not be a discontinuity in the initial perturbation, as it is a requirement of the pdsolve function. (see chapter 2 for details). Thus, we use the symmetry of the problem to consider the perturbations in a half of the slab, in the domain $z = [0, 50d]$ only. The spatial structure of the velocity oscillations in the domain $z = [-50d, 0]$ is the same as in the considered domain, but in the anti-phase in time. The external boundary of the simulation domain was taken far enough from the slab axis, to avoid the interaction of the excited oscillations with the outer boundary in the duration of
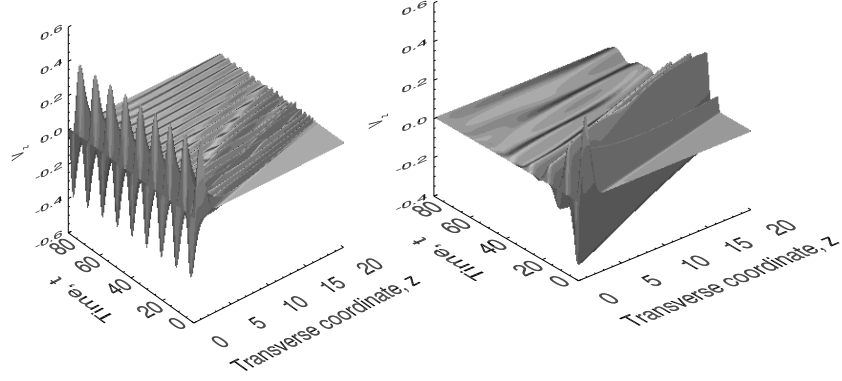
Figure 4.1: Time-distance plots of transverse flows in sausage oscillations. Left panel: example of a trapped sausage oscillation in a plasma slab with the parameters: $\delta = 0.8$ and $\alpha = 6$ for the wave number $k_x = 1.5$. Right panel: example of a leaky sausage oscillation in a plasma slab with the parameters: $\delta = 0.7$ and $\alpha = 6$, for $k_x = 0.4$. The spatial coordinate is normalised such that the half-width of the slab, $d = 1$, and the time is measured in the units $d/C_{A\infty}$, where d is the slab half-width and $C_{A\infty}$ is the Alfvén speed outside the slab.

the simulation.

Once excited, the perturbations oscillate almost harmonically (Fig. 4.1). As in the cylindrical case, discussed in chapter 2, the simulations show two regimes of oscillation: trapped and leaky.

In the trapped regime the oscillation is completely contained by the plasma inhomogeneity. It is determined from the simulation as the amplitude of the oscillation inside the well remains constant (Fig. 4.1, left panel). These are the sausage oscillations described by Edwin and Roberts [1983], as shown in Fig. 1.7, who found that these oscillations could only exist when $C_{A0} < \omega/k < C_{A\infty}$, which gives the extent of the trapped regime. These limits are shown by the straight lines in Fig. 4.2, 4.3.

The leaky regime is characterised by oscillations which do not remain contained by the plasma inhomogeneity, these oscillations continuously excite fast waves that propagate away from the centre of the simulation towards the boundary. These oscillations are identified by their decreasing amplitude inside the inhomogeneity (Fig. 4.1, right panel). However these oscillations generally remain of sufficient quality for the period to be measured and studied. This finding is consistent with the analytical estimation obtained in Terradas

et al. [2005] for the long-wavelength ($k_x d \ll 1$) oscillations in a slab with a step-function profile of the Alfvén speed. Using Eq. (12-14) from Terradas et al. [2005], and converting to the notation used in this study:

$$\tau_D = \frac{2\pi}{\omega_I} \approx \frac{2\pi a C_{A\infty}}{C_{A0}^2}, \text{ and } P = \frac{2\pi}{\omega_R} \approx \frac{4a}{C_{A0}}, \tag{4.13}$$

where τ_D is the decay time of the oscillations, P is the period, and ω_I and ω_R are the imaginary and real parts of the oscillation frequency, respectively. Consequently, the oscillation quality can be estimated as:

$$Q = \frac{\tau_D}{P} \approx \frac{\pi}{2} \frac{C_{A\infty}}{C_{A0}} = \frac{\pi}{2} (1 - \delta)^{-1}. \tag{4.14}$$

Thus, Eq. (4.14) with $\delta = 0.5$ gives $Q = \pi$. Our numerical results give, e.g. $Q \approx 4.02$ for $\delta = 0.5$, $\alpha = 8$ and $k_x = 1$. These two numbers are sufficiently close to each other. The small discrepancy should be attributed to the finite wavelength and finite smoothness of the profile, used in the numerical simulations.

Moreover, sausage oscillations have been identified in the microwave and hard X-ray emission generated in the impulsive phase of solar flares (see Nakariakov and Melnikov [2009] for details). The observations do not show any evidence of the exponential damping, and their duration is determined by the duration of the impulsive phase of the flare. Our simulations show that the decay time in a number of cases is significantly longer than several periods of oscillation. This makes the damping time non-detectable in the observations limited by the duration of the impulsive phase of the flare. As in chapter 2 we concentrate only on the dependence of the sausage oscillation period on the parameters of the problem, and do not discuss further the oscillation quality and the damping time.

For ease of visualisation the following normalisations were used: The spatial units are normalised such that the half-width of the inhomogeneity, $d = 1$, the temporal units were $d/C_{A\infty}$ where $C_{A\infty} = 1$ is the external Alfvén speed. By order of magnitude, the half-width could be about 1 Mm, and the external Alfvén speed is about 2–3 Mm/s.

4.2.2   Results

Fig. 4.2 shows the dependence of the sausage oscillation period on the wavelength for different density ratios. This figure extends the results obtained in [Pascoe et al., 2007a] to the case of long wavelengths. It shows that, similarly to the cylindrical case, the sausage oscillation period becomes gradually independent of the wavelength. This figure is the slab equivalent to Fig. 2.4. Edwin and Roberts [1983] showed that the sausage oscillation exists as a trapped oscillation when $C_{A0} < \omega/k_x < C_{A\infty}$. These are indicated by the straight lines
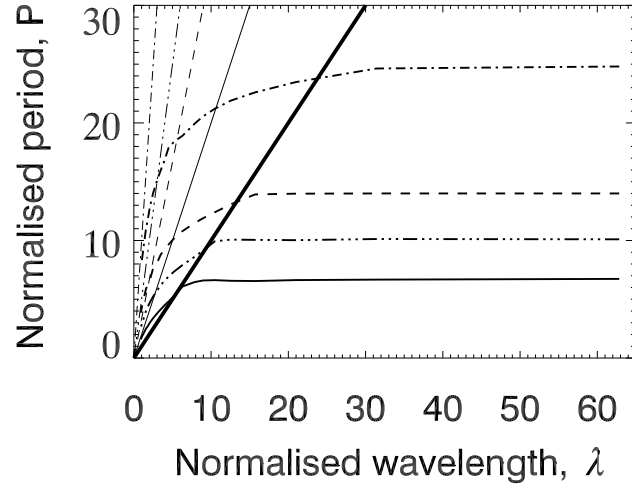
Figure 4.2: The variation of the sausage oscillation period with the wavelength in a plasma slab with $\alpha = 6$, for different values of δ: the solid line corresponds to $\delta = 0.5$, the triple dot-dashed line corresponds to $\delta = 0.7$, the dashed line to $\delta = 0.8$, and the dot-dashed line to $\delta = 0.9$. The thick straight line shows $P = \lambda/C_{\mathrm{Ae}}$, that is the cutoff separating the trapped and leaky regimes. The thinner straight lines show $P = \lambda/C_{\mathrm{A0}}$ that correspond to the short wavelength asymptote in each case.

radiating from the origin on the plot, any oscillation to the right of the thick straight line is therefore leaky, and any to the left are trapped. It is consistent with the conclusion drawn for step-function profiles, that the same qualitative behaviour is observed in the slab geometry as in the cylindrical geometry [Edwin and Roberts, 1982, 1983]. Moreover, this similarity remains valid in the leaky regime too. For a given density ratio δ, the period P increases monotonically with the wavelength λ. For a given wavelength, a slab with a higher density ratio, in other words with a deeper well in the fast speed, oscillates with a longer period. The plot also demonstrates that the dependence saturates in the long wavelength limit for all depths of the well. This similarity with the cylindrical case is expected, as the nature of the oscillation has not changed.

An estimate for the typical period of sausage oscillations for typical coronal parameters can be obtained as follows. In a plasma slab of half-width $d = 2,000$ km and an external Alfvén speed of $C_{A\infty} = 1,000$ kms^{-1} the normalised period $P_{\mathrm{saus}} \approx 0.5 d/C_{A\infty}$ is about one second. For wider slabs, the period can be several times longer. This is consistent with typical observations e.g. in the radio band [e.g., Nakariakov and Melnikov, 2009]. Also, these typical periods are much shorter than the typical life-times of oscillating plasma non-uniformities, such as helmet streamers, flaring current sheets and supra-arcade flows.

Fig. 4.3 shows a comparison of the dependences of the sausage oscillation period on the wavelength for the slab and cylindrical geometries, for the same profile of the transverse non-uniformity and its width. In the slab case the sausage period is longer. This result is consistent with the estimates obtained analytically in the case of the step-function profiles [Edwin and Roberts, 1982, 1983] in the trapped regime. It can be illustrated, e.g., by the cut-off values of the wave numbers that are (as obtained in section 3.2 for the cylinder)

$$
k_{\mathrm{c}} d \left(\frac{C_{\mathrm{Ae}}^2 - C_{\mathrm{A0}}^2}{C_{\mathrm{A0}}^2} \right)^{1/2} \approx \begin{cases} 1.57, & \text{in a slab,} \\ 2.4, & \text{in a cylinder,} \end{cases} \tag{4.15}
$$

where C_{Ae} and C_{A0} are the Alfvén speed values outside and inside the waveguide, and d is the half-width of the waveguide (cf. the parameter d in Eq. (4.1)). The plasma inside and outside is taken to be of zero-β. It is clear that on the plane representing the dependence of the phase speed of the sausage mode on the longitudinal wave number the dispersion curve for a slab is situated lower than for a cylinder, when all parameters of the slab and the cylinder are the same. Thus, for the same wave number, the phase speed in the slab case is lower than in the cylinder. Hence, the sausage oscillation period in a slab is longer than in the cylinder. In the trapped regime, the quantitative difference between the slab and cylindrical cases can be readily understood. In both cases the oscillation is confined to the non-uniformity, while in the cylindrical case this confinement is more efficient. If in the slab case the energy outside the slab decreases exponentially, in the cylindrical case such
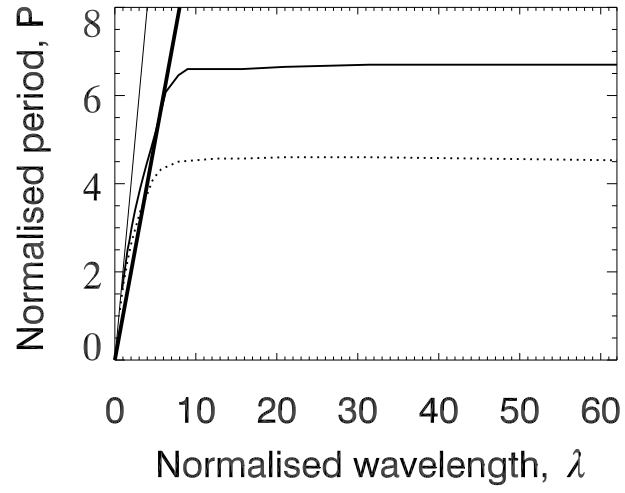
Figure 4.3: Comparison of the variation of period of these oscillations against longitudinal wavelength in the slab and cylindrical cases, both curves have values of $\alpha = 6$ and $\delta = 0.5$, the dotted line represents the cylindrical case [Nakariakov et al., 2012], the solid line represents the slab. The thick straight line shows $P = \lambda/C_{A\infty}$, that is the cutoff separating the trapped and leaky regimes. The thinner straight line shows $P = \lambda/C_{A0}$ which corresponds to the short wavelength asymptote.
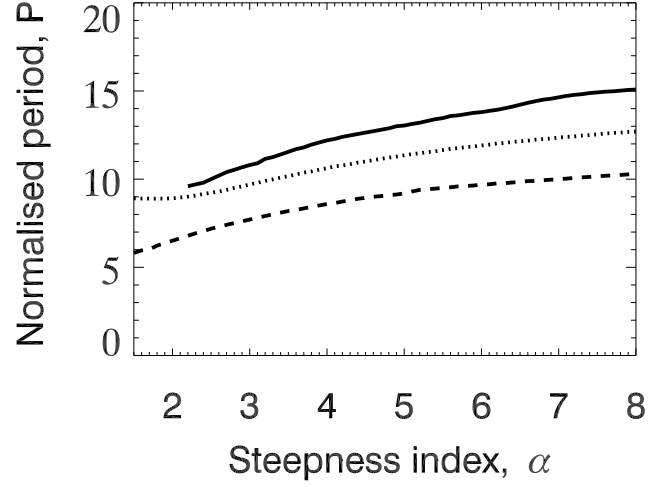
Figure 4.4: The dependence of the period of trapped sausage oscillations on the steepness index, α, for different wave numbers: $k_x = 0.4$ shown by the solid line, $k_x = 0.7$ shown by the dotted line, and $k_x = 1.4$ by the dashed line. The solid line stops where the oscillation becomes too leaky to accurately measure the period. For all the curves, the value of the parameter δ was fixed as 0.8. The period is measured in normalised units, equal to $d/C_{A\infty}$, where d is the slab half-width and $C_{A\infty}$ is the Alfvén speed outside the slab.

an exponential decrease has the additional $1/r$-factor, where r is the transverse (e.g. radial) coordinate. Our results show that this behaviour is also seen in the leaky regime, and in non-uniformities with smooth transverse profiles.

Fig. 4.4 shows the dependence of the sausage oscillation period on the steepness of the transverse profile, α, for a fixed value of the parameter δ. Each of the lines represents a fixed value of k_x, for the line $k_x = 0.4$ the oscillations are leaky for all values of α, for $k_x = 1.4$ the oscillations are trapped for all values of α, and for $k_x = 0.7$ the oscillations are leaky for values of α lower than 2.5, yet trapped for larger α. As expected for any given value of α a smaller value of k_x, and hence longer longitudinal wavelength, results in a larger period of oscillation. This can be understood by considering the oscillations as a wave packet trapped inside the potential well of the fast magnetoacoustic speed, being reflected or refracted off the walls at either side, whilst also travelling along the well. As the longitudinal wavelength increases the effective distance between two reflections increases, resulting in the increase in the wave period.

As with the cylindrical case, for a fixed longitudinal wave number k_x a larger value of α, and hence a steeper potential well, also results in a longer period of oscillations. An
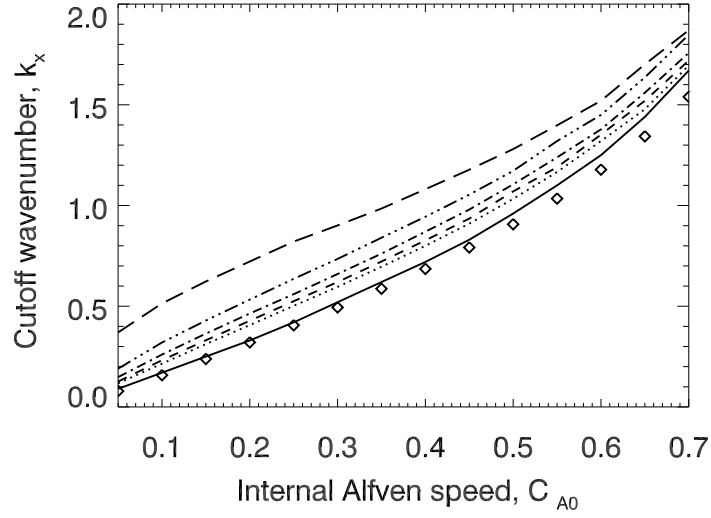
Figure 4.5: The dependence of the cutoff longitudinal wave number of a sausage oscillation on the internal Alfvén speed (and hence the potential well depth) for a fixed value of the external Alfvén speed and for different values of α. The long dashed line corresponds to $\alpha = 2$, the triple-dot dashed line to $\alpha = 4$, the dot dashed line to $\alpha = 6$, the dashed line to $\alpha = 8$, the dotted line to $\alpha = 10$ and the solid line shows the step-function profile, i.e. $\alpha \to \infty$. The diamonds are the values for the cutoff in the case of a step-function profile, obtained analytically. The internal Alfvén speed is normalised such that the external Alfvén speed, $C_{Ae} = 1$, and the wavenumber is normalised such that the characteristic width of the slab, $d = 1$

explanation for this has already been discussed in chapter 2. The same reasoning applies in the slab case as in the cylindrical.

Fig. 4.5 shows the dependence of the cutoff wave number on the depth of the potential well in the slab geometry. The cutoff is defined as the value of the longitudinal wave number k_c at which the oscillations transition from being trapped to leaky. For the cutoff wave number, the phase speed of the sausage mode equals to the Alfvén speed outside the slab, C_{Ae}. Thus, at the cut-off, the sausage oscillation period is

$$P = \frac{\lambda}{C_{Ae}} = \frac{2\pi}{k_x C_{Ae}}. \tag{4.16}$$

It is evident that for all values of the steepness parameter α, the cutoff value of the longitudinal wave number increases with the increase in the Alfvén speed at the axis of the slab (i.e. at the bottom of the potential well). This result can be readily understood, as it is easier for the waves to escape a shallower potential well. Also, the cutoff wave number increases
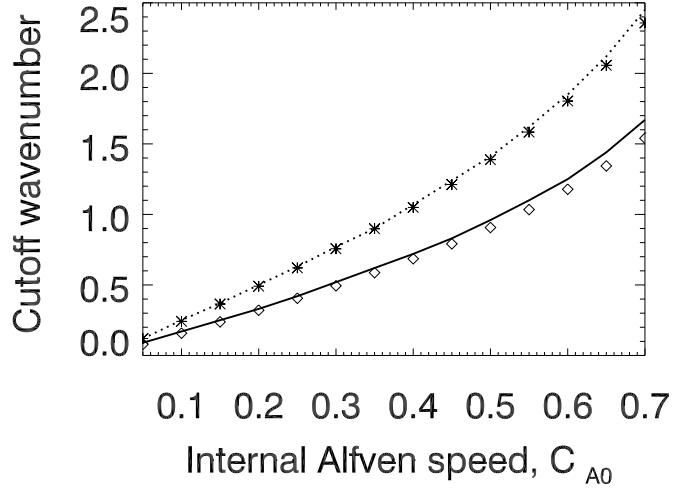
Figure 4.6: Comparison of the variation in the cutoff longitudinal wave number with the internal Alfvén speed, in the slab and cylindrical cases with the step-function profiles, $\alpha \rightarrow \infty$. The solid line represents the numerically calculated values in the slab case, and the diamonds the analytical values; the dotted line represents the numerically calculated values in the cylindrical case [Nakariakov et al., 2012], and the crosses the analytical values.

with the decrease in the steepness parameter α, as a smoother transverse profile is more suitable for fast wave leakage.

In Fig. 4.5, we also show the cutoff values determined analytically in the case of a step-function profile [Edwin and Roberts, 1982], the calculation for the cylindrical case is performed in 3.2. The analytical results are slightly different from the results obtained numerically in the case $\alpha \rightarrow \infty$. This small discrepancy can be attributed to the intrinsic difficulties in the determination of the cut-off value numerically: the transition from the trapped to leaky regimes is rather smooth and is not easy to determine precisely. However, the numerical results show the main tendency very well and hence are reliable. In general, our results show that in a slab, as well as in a cylinder [Nakariakov et al., 2012], the steeper and deeper wells of the fast magnetoacoustic speed confine sausage oscillations to a greater degree.

Fig. 4.6 shows a comparison of the cutoff longitudinal wave numbers calculated analytically and obtained numerically for both cylindrical and slab geometries, c.f. Fig. 4.5. There is a good agreement between the analytical values and those obtained numerically for both the cylindrical and the slab geometries.

It is evident that the cutoff longitudinal wavenumber is larger in the cylindrical ge-

ometry than in the slab geometry, hence these oscillations are better confined in a cylindrical waveguide than a slab.

4.2.3   Conclusions

We studied sausage modes of a plasma slab stretched along the magnetic field, considering the effect of the smooth transverse profile of the fast magnetoacoustic speed. The slab could contain a thin (much thinner than the transverse size of the slab) current sheet with an anti-parallel magnetic field at its centre. Our attention is restricted to the case of waves propagating along the magnetic field in the zero-β plasma. In this case, a localised increase in the density of the plasma results in a localised decrease in the Alfvén speed, and hence in the fast magnetoacoustic speed. A localised decrease in the fast magnetoacoustic speed makes the slab a fast magnetoacoustic waveguide. Both trapped and leaky regimes of the oscillations were studied. It was found that sausage modes of slabs have, in general, the same properties as sausage modes of plasma cylinders, studied in chapter 2. Our results can be summarised as follows:

1. Both leaky and trapped regimes of sausage oscillations can be readily excited by an initial impulsive driver. The leaky regime occurs for longitudinal wavelengths longer than the trapped regime.

2. In the trapped regime, the sausage oscillation period grows with the increase in the longitudinal wavelength. In the leaky regime, the dependence of the period on the wavelength experiences saturation, and the period becomes independent of the wavelength. In the leaky regime the period is always longer than in the trapped regime.

3. In a plasma cylinder and a slab of the same half-width and the same parameters of the transverse profiles of the fast magnetoacoustic speed, the sausage oscillation period in the slab is always longer than in the cylinder. The difference can reach 50%.

4. In slabs with steeper transverse profiles of the fast magnetoacoustic speed, the sausage oscillation periods are longer.

5. For a given depth of the potential well, smoother profiles of the fast magnetoacoustic speed (with a smaller value of the parameter α), have bigger values of the cutoff longitudinal wave numbers. The cutoff values separate the leaky and trapped regimes.

6. For the same potential wells, the cutoff wave numbers in a cylinder are always larger than in a slab.

In the presence of the current sheet at the centre of the slab the results remain the same, as our formalism in this case remains exactly the same. Indeed, the presence of the current sheet causes a singularity at the centre of the slab, that does not affect the sausage oscillations that have zero transverse flows at the slab centre and hence do not "feel" the singularity.

We would like to stress that both leaky and trapped regimes of sausage oscillations of plasma slabs in the solar corona are well observable, as the quality of leaky oscillations can be high. Also, results obtained for a slab can be applied to coronal current sheets, provided the magnetic field at either sides of the sheet is anti-parallel.

Chapter 5

Developing a static model for a coronal active region

5.1 Introduction

In this chapter we consider the coronal heating problem in more detail. As previously mentioned in Chapter 1 there are many coronal heating theories which have been proposed. In this chapter we present a model for a coronal active region which allows an arbitrary empirically determined heating rate to be applied. This model can then be compared to EUV observations. This allows us to test different heating mechanisms, as each of these coronal heating theories suggest an underlying heating rate, related to the magnetic field and the various other plasma parameters. This allows these various mechanisms to be modelled and compared to observational data for the solar corona [Mandrini et al., 2000; Schrijver et al., 2004].

Efforts to provide observational constraints on heating models have been made possible by the continuing development of solar X-ray and EUV instrumentation [e.g. Golub et al., 1980; Fisher et al., 1998]. Simulations of the coronal magnetic fields and modelling of the expected X-ray and/or EUV emission for different coronal heating models have been performed by previous authors. For instance, Schrijver et al. [2004] use a potential-field source-surface (PFSS) model to model the entire coronal magnetic field from SOHO/MDI magnetograms, as well as a quasi-hydrostatic model for the plasma. This information was combined to produce simulations of EIT and SXT images, and compare them to the observations. More recently Dudík et al. [2011] used a potential magnetic field model and scaling laws to model an active region in EUV and X-ray bands. On the other hand, Fludra and Ireland [2003, 2008] studied global relationships between the active region integrated magnetic flux and EUV emission line intensities in a large number of active regions. From this

statistical analysis they obtained clear power laws linking these quantities, and assessed their capability to constrain the heating rate. A subsequent study by Fludra and Warren [2010] for the first time compared fully resolved images in an EUV spectral line of O v 63.0 nm with the photospheric magnetic field, leading to the identification of a dominant, ubiquitous variable component of the transition region EUV emission and a discovery of a steady basal heating, and derived the following dependence of the basal heating rate E_H on the photospheric magnetic flux density ϕ and loop length L: $E_H \propto \phi^{0.5} L^{-1}$.

In a most general approach, one would assume that the heating is variable in time and leads to a dynamic behaviour of plasma confined in coronal loops. Radiative hydro-dynamic loop models with different forms of the heating function have been studied by many authors (see Reale [2014] for review). However, since the temporal variability of the heating rate needs to be arbitrarily prescribed, it adds an additional degree of freedom, increasing the complexity of the problem. In this chapter we are addressing the ability of the observations to provide constraints on models, therefore we begin with simpler, hydrostatic models, reducing significantly the number of model parameters. This way, we are able to study the effect of the spatial variability of the heating rate along the loop on the resulting EUV emission without the complications of the temporal variability.

The magnetic field defines the geometry of coronal loops and is postulated to affect the heating rate in many heating models. Unfortunately, in the majority of cases at present it is not possible to directly measure the magnetic field in the corona. It is however possible to measure the magnetic field in the photosphere, one such instrument that currently provides excellent photospheric magnetic field data is the Helioseismic and Magnetic Imager on the Solar Dynamics Observatory [SDO/HMI, Scherrer et al., 2012]. This photospheric magnetic field can then be extrapolated into the corona. This is performed using a non-linear force-free magnetic field model.

The other element required is modelling the thermodynamic properties of the plasma in coronal loops. Many models have been proposed, from static 1-D models e.g. [Rosner et al., 1978], to full 3-D MHD simulations e.g. [Pascoe et al., 2009a].

The aim of this chapter is to develop a diagnostic of the heating mechanisms in coronal loops and evaluate the capability of the observed EUV emission to provide constraints on the parameters of the heating model. We achieve this by modelling a coronal active region, firstly by extrapolating its magnetic field from the photospheric field, then by using a 1-D hydrostatic model to model the plasma in selected magnetic flux tubes of this active region. This model allows an arbitrary heating rate, which was chosen to be a function of the local magnetic field strength. By comparing modelled EUV emission of these loops to EUV images of the active region a diagnostic can be developed to measure the heating rate in the corona.

SDO provides a unique opportunity to perform this study, using two of its instruments, the Helioseismic and Magnetic Imager (HMI) and the EUV imager Atmospheric Imaging Assembly (AIA) [Lemen et al., 2012]. HMI provides full disk vector magnetograms with 1"x1" pixel size every 12 minutes. This allows accurate measurements of the photospheric magnetic field for any active region, which is a basis for performing nonlinear force-free (NLFF) extrapolations [Schou et al., 2012]. AIA provides full disk EUV images with seven different filters every twelve seconds, with a pixel size of ~ 0.6"x0.6" - this allows for comparison with predicted EUV emission from our model.

This chapter is arranged as follows. In section 5.2.1 we discuss the NLFF extrapolations then the hydrostatic loop modelling is discussed in section 5.2.2, leading to modelling of the EUV emission, which is discussed in section 5.2.3. We then use all of these components together to model the whole active region in section 5.2.4. These models are then discussed and compared to coronal observations in section 5.3.

5.2   Method

5.2.1   Magnetic field extrapolations

The first stage of the model is to extrapolate the coronal magnetic field. The theory behind extrapolating force free fields was discussed in section 1.4.3. The basic principle is that force free fields must obey:

$$\nabla \times \mathbf{B} = \alpha \mathbf{B}, \tag{5.1}$$

$$\nabla \cdot \mathbf{B} = 0. \tag{5.2}$$

In this case we are assuming non-linear force free fields, where the force free parameter, α, can vary across field lines, but is constant on a given field line.

Various methods have been proposed to find solutions to the non-linear system of equations (5.1) and (5.2) [e.g Amari et al., 1997; Sakurai, 1981; Roumeliotis, 1996; Aschwanden, 2013; Wheatland et al., 2000]. Schrijver et al. [2006] and Metcalf et al. [2008] compared different NLFF magnetic field models and found that the optimisation code developed by Wiegelmann [2004] was the most accurate model tested, as well as being reasonably computationally efficient.

The bottom boundary conditions for the NLFF extrapolation were vector magnetograms obtained from SDO/HMI. These contained the vector photospheric magnetic field data with a 1"x1" resolution. A typical size of the box surrounding the active region is 5x5 arcminutes, leaving a sufficient margin around the active region magnetic fields to include all of the strong magnetic field lines as they expand into the corona. An NLFF model was

then used to extrapolate this field into the corona to give an estimate of the coronal magnetic field. The NLFF model used is described by Wiegelmann et al. [2012]. A brief overview of the process is as follows:

Before the vector magnetograms can be used as boundary conditions the 180 degree ambiguity must be resolved. This ambiguity arises because when the magnetograms are derived from the optical observations there are two solutions for the perpendicular components of the magnetic field 180 degrees apart from each other. This ambiguity must therefore be resolved for each pixel in the magnetogram by finding a solution that is self consistent. Many methods have been proposed for doing this, the data products used in this study already had this ambiguity resolved by using the "Minimum Energy" method [Hoeksema et al., 2014; Metcalf, 1994].

The first stage of the modelling is to 'pre-process' the vector magnetogram, in order to obtain the best results from the NLFF model [see Wiegelmann et al., 2006]. This pre-processing involves making small adjustments to the vector magnetogram in order for the NLFF model to be applied more accurately. This is justified so long as the data remains within the measurement errors of the original magnetogram, these are larger in a direction perpendicular to the line-of-sight. As the considered active regions are sufficiently close to the disk centre these directions are equivalent to the x- and y- directions, of the Cartesian projection of the magnetogram, where the z- axis is the vertical direction.

The purpose of this pre-processing is to firstly make sure the data is consistent with the force free approximation, obeying the criteria set out by Aly [1989], which are that the total force on the boundary vanishes:

$$\int_S B_x B_z dx dy = \int_S B_y B_z dx dy = 0, \tag{5.3}$$

$$\int_S (B_x^2 + B_y^2) dx dy = \int_S B_z^2 dx dy, \tag{5.4}$$

and that the torque on the boundary vanished:

$$\int_S x(B_x^2 + B_y^2) dx dy = \int_S x B_z^2 dx dy, \tag{5.5}$$

$$\int_S y(B_x^2 + B_y^2) dx dy = \int_S y B_z^2 dx dy, \tag{5.6}$$

$$\int_S B_x B_z dx dy = \int_S x B_y B_x dx dy, \tag{5.7}$$

where S is a boundary of the modelled region, in this case the magnetogram.

The other reason for the pre-processing is to smooth the data to make it easier to compute the NLFF field. This is particularly relevant around the boundaries of the magne-

togram, which should have a minimal impact on the final NLFF field.

Once the magnetogram has been pre-processed, the NLFF model is calculated using the optimisation code developed by Wiegelmann [2004], and tested with SDO data [Wiegelmann et al., 2012].

The optimisation technique initially only considers the vertical component of the photospheric magnetic field, which is then used as the boundary condition for a potential field. This potential field is then used as the boundary condition for the other five sides of the computational domain, as well as the initial conditions for the optimisation process. A parameter, K, is used to optimise the field towards a force free field:

$$
\begin{aligned}
K = \int_V w(x, y, z) \left[B^{-2} |(\nabla \times \mathbf{B}) \times \mathbf{B}|^2 + |\nabla \cdot \mathbf{B}|^2 \right] d^3 V \\
+ \nu \int_S ((\mathbf{B} - \mathbf{B}_{\text{obs}}) \cdot \mathbf{W} \cdot (\mathbf{B} - \mathbf{B}_{\text{obs}}) \mathbf{d}^2 \mathbf{S},
\end{aligned}
\tag{5.8}
$$

where $w(x, y, z)$ is the weighting function, ν is a Lagrangian multiplier and $\mathbf{W}(x, y)$ is a diagonal error matrix, V is the entire volume of the modelled region and S is the boundary as before. From this it is clear that $K = 0$ when the field is force-free and matches the observed boundary conditions, the field is therefore iterated in such a way to reduce K. The weighting function w is set to be equal to unity in the majority of the model region, and decrease to 0 through a boundary region toward the top and lateral boundaries of the domain. The purpose of this is to reduce the importance of these boundaries on the final field as they are essentially unknown. The second term in Eq. (5.8) ensures that the modelled field matches the observed field within observation errors. The error matrix $\mathbf{W}$ should be specified for each instrument (SDO/HMI in this case) and controls the rate which these boundary conditions are applied. A more detailed description of the technique can be found in Wiegelmann and Inhester [2010]. The Lagrangian multiplier is used during the optimisation process, its specific value is not important for the purposes of this study.

This procedure provides a model for the coronal magnetic field of the active region. The next stage is to define the loops traced by this field. We trace a field line from each pixel in the base of our field. To do this we use a fourth order Runge-Kutta scheme to calculate the direction at each step of the field line by using the direction of the local magnetic field as the line's gradient. As this study is only interested in coronal loops, we discard those loops that do not reach a coronal height (2000 km), as well as those loops which could not be traced from photosphere to photosphere (i.e., those which left the sides or top of the box containing the modelled magnetic field).
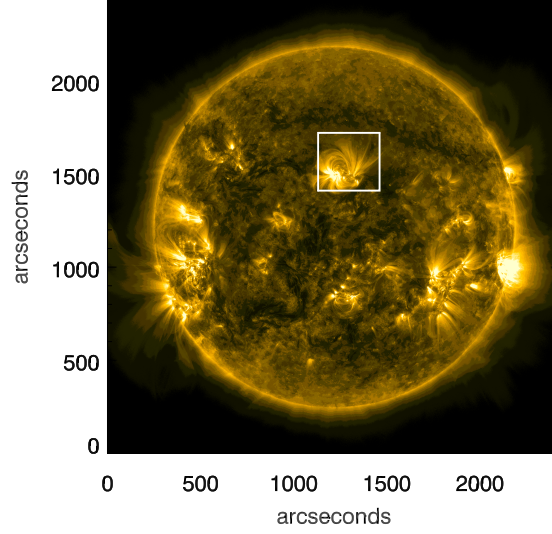
Figure 5.1: Full disk AIA 171 image from 4th November 2013. The area surrounding NOAA 11897 which has been modelled using the NLFF optimisation routine is shown by the white box.

Example active region

In this section we demonstrate how this model is applied to and compared with SDO observations. A similar test was performed and explained in detail by Wiegelmann et al. [2012].

To do this we must first select an active region to be modelled, the chosen region is NOAA 11897 from the 4th November 2013. Fig 5.1 shows a full disk AIA 171 Å image from 4th November 2013 with the white box denoting the area surrounding the active region to be modelled. This active region is a good candidate for the modelling as its magnetic field is well isolated from any other region of strong magnetic field. Fig. 5.2 shows the line-of-sight magnetogram for this active region, the size of this cut out is shown by the white box in Fig. 5.1. We can see that the regions of strong photospheric magnetic field are well contained in this cutout with a sizeable border of weaker magnetic field surrounding it towards the edge of the region to be modelled. This is important as the weighting function limits the importance of the magnetic field data towards the boundaries of the region considered, so it is important to restrict these to being the areas of low magnetic field which are less likely to influence the coronal magnetic structures which are observed.

The optimisation routine as described was then applied to the vector magnetogram data of this region, after the vector magnetograms have been pre-processed as described.
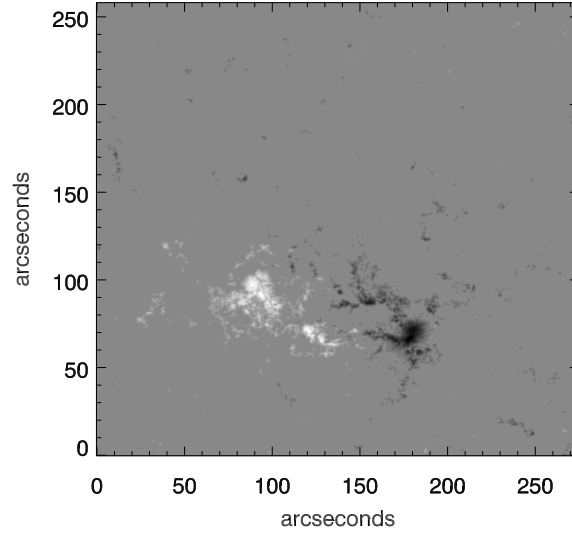
Figure 5.2: Line-of-sight magnetogram of NOAA 11897 from 4th November 2013.
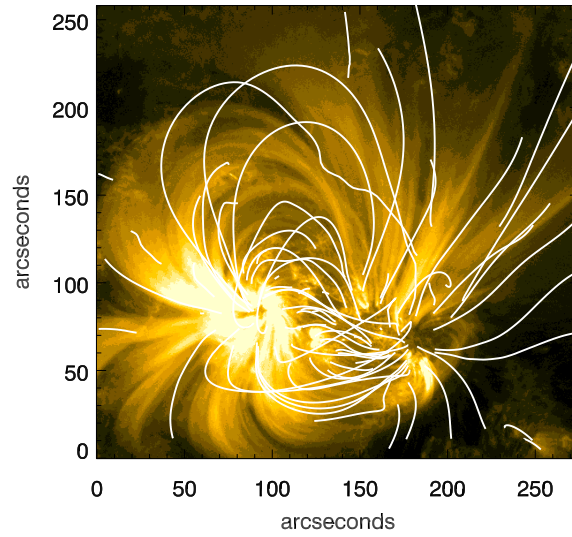

Figure 5.3: AIA 171 image of NOAA 11897, with selected field lines modelled by the NLFFF optimisation code overlaid.

This gives us a cube of magnetic field data describing the magnetic field above the photospheric region shown. From this cube of magnetic field data field lines can be traced, and compared to the observed coronal structures. Fig. 5.3 shows an AIA 171 image of the selected region with selected field lines plotted on top, we can see that the geometry of the modelled field appears to match very well with the observed EUV structures.

5.2.2 Loop models

Once the magnetic topology has been defined by the NLFF model, the plasma in the loops must be modelled to derive electron temperature, density and flow velocities. In the general case of dynamic plasmas, magnetohydrodynamic modelling needs to be performed. Under the assumption of weak variation of the loop's cross-sectional area along the loop, hydrodynamic models considering the field aligned motions could be sufficient. Examples of hydrodynamic software codes include Oran et al. [1982], Rosner and Vaiana [1977], Tsiklauri et al. [2004]. The spatial and temporal variation of the heating along the loop is the primary input required by these models. As this is normally not known and needs to be postulated, a simpler approach is to investigate cases of quasi-static loops, where the heating is either constant in time or varies with a timescale shorter than the typical radiative cooling and thermal conduction timescales, and therefore can be considered constant. Many such models are described in the literature [Rosner et al., 1978; Reale et al., 2000; Vesecky et al., 1979].

More recently the validity of the assumption of steady heating in some categories of loops has been questioned [Schrijver and van Ballegooijen, 2005]. While it is true that a multitude of intermittent acts of energy release are observed in the corona in the form of small events [Berghmans et al., 1998] possibly associated with nanoflares [Parker, 1988], a study of the heating observed at transition region temperatures by Fludra and Warren [2010] showed that at least 25% of the area covered by active region magnetic fields stronger than 90 G undergo quasi-steady heating, through some universal while not yet identified process which is the same in all active regions. Moreover, examination of several SDO/AIA movies taken at coronal temperatures shows that the observed loop intensities remain constant over at least 10 minutes, which is longer than the timescales for the radiative and conductive cooling. In this chapter we therefore investigate quasi-steady heating using hydrostatic loop models.

We use a hydrostatic model code devoloped by van Ballegooijen [Schrijver and van Ballegooijen, 2005]. This code finds a static solution to the energy balance equation in 1D, and allows for an arbitrary heating rate along the loop. It models the loop from the transition region at the first footpoint through the corona, and back to the transition region at the second footpoint. It sets the temperature at each footpoint to 20000 K, twice the temperature of the low chromosphere. The energy flux through the boundary is calculated

in the appendix of the cited paper. The model also assumes that the loop cross section is inversely proportional to local magnetic field strength.

For this study we use a volumetric heating rate of the following form:

$$E_H(s) = Q_a L^\lambda \left(\frac{B(s)}{B_{\max}}\right)^\beta,\tag{5.9}$$

where $B(s)$ is the magnitude of the magnetic field at distance s along the loop, and $B_{\max}$ is a constant, set to be 2500 G for this study, as that was larger than any magnetic field strength considered which ensures B/B_{max} is less than 1. This gives three parameters to control the heating rate, Q_a, β and λ.

The range of values of β considered here is from -2 to 2. These values include a case of a constant heating along the loop ($\beta = 0$), the predictions from the DC heating models $\beta = 2$, and intermediate values that include predictions of the heating rate dependence on B from AC models. Since B decreases with height, positive β gives heating concentrated near the footpoints. We have therefore included also negative values of β which give heating concentrated near the loop-top, as is suggested by some wave heating theories [Ruderman et al., 1997; Halberstadt and Goedbloed, 1995].

5.2.3 Modelling the coronal EUV emission

In order to compare the modelled active region loops with real loops observed by the current or recent instruments, the EUV emission is modelled in two different channels, the 171 Å and 335 Å used by SDO/AIA, and the emission for the pure spectral lines Fe ıx 171 Å and Fe xvı 335 Å. The Fe xvı lines were routinely observed by the SOHO Coronal Diagnostic Spectrometer at 360.8 Å [Fludra and Ireland, 2003, 2008] and also at 335 Å, while the Hinode EIS spectrometer [Culhane et al., 2007] observes Fe xvı 263.0 Å and Fe ıx 171 Å.

The temperature response for the AIA channels has been calculated by Lemen et al. [2012] and is available in the SolarSoft library. The emissivity of the Fe ıx 171, Fe xvı 335 and 360.7 Å spectral lines has been derived using the ADAS package [Summers, 2001] and is also available in CHIANTI [Dere et al., 2009]. The response functions for the AIA 171 & 335 channels, and Fe ıx 171 Å and Fe xvı 335 Å lines are shown in Fig. 5.4. The electron temperature and density of the plasma was then modelled along each of the loops in the active region for different values of Q_a and β as described in the previous Section, and these parameters were convolved with the response functions of the various lines to give the modelled emission.
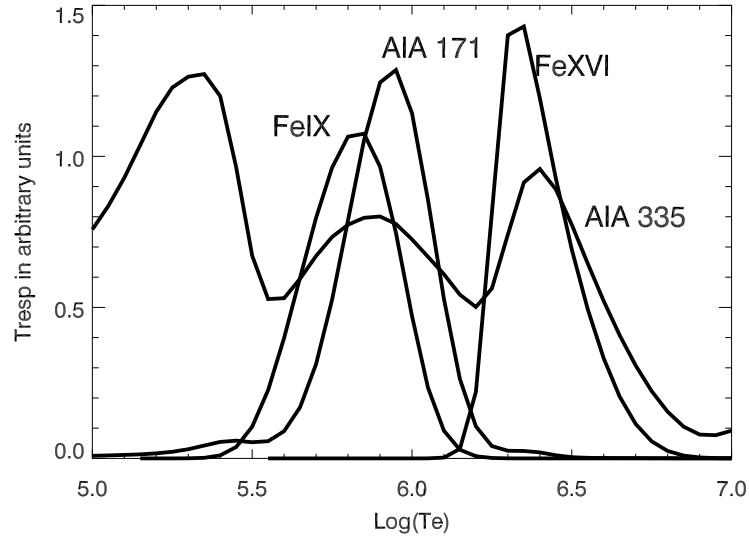
Figure 5.4: Temperature response of the considered SDO/AIA filters, 171 and 335, and spectral lines Fe ɪx 171 Å and Fe xvɪ 335 Å.

5.2.4 Bringing it all together

The final difficulty involves selecting sensible values for the parameters, λ, β and Q_a. Fludra and Warren [2010] found that $\lambda = -0.5$ was an appropriate value, so that was also used in this study. Identifying the value of β was the main focus of this study, and therefore it was not appropriate to prescribe a fixed value for this parameter. Instead a range of values were considered, as described in 5.2.2. The parameter Q_a controls the overall magnitude of the heating, its value was therefore selected to provide a range of temperatures close to the peak response of the chosen filter. This was done by taking the total heating along each loop and assuming it is evenly distributed along the loop, then using the RTV scaling laws [Rosner et al., 1978], which were described in more detail in Chapter 1, to estimate an appropriate value of Q_a. The full model is then run with this estimated Q_a and the range of loop temperatures are recorded, Q_a can then be manually adjusted if the initial estimate is too high or low.

Once this modelled emission had been calculated for all loops it is then projected on a 2D plane in the same manner as would be observed by SDO/AIA, as shown in Fig. 5.6. Line of sight effects are accounted for by assuming that our loops are narrower than the pixels, and therefore assigning the total intensity of each loop section to the nearest pixel. This can be compared to the observed AIA 171 Å image in Fig. 5.5. It is important to note that there are several differences between the modelled and observed images, due to the
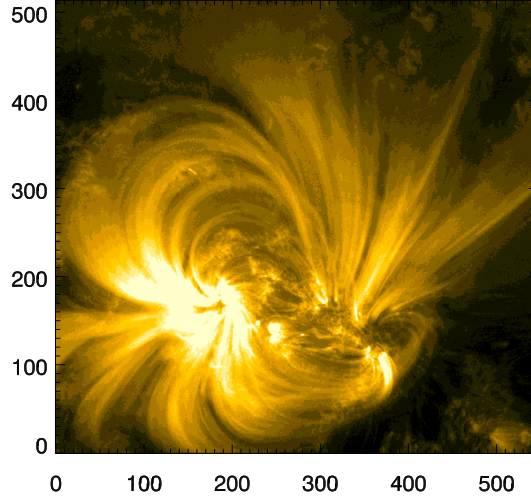
Figure 5.5: SDO/AIA image of active region NOAA 11897 in 171 Å filter, observed on 4th November 2013.
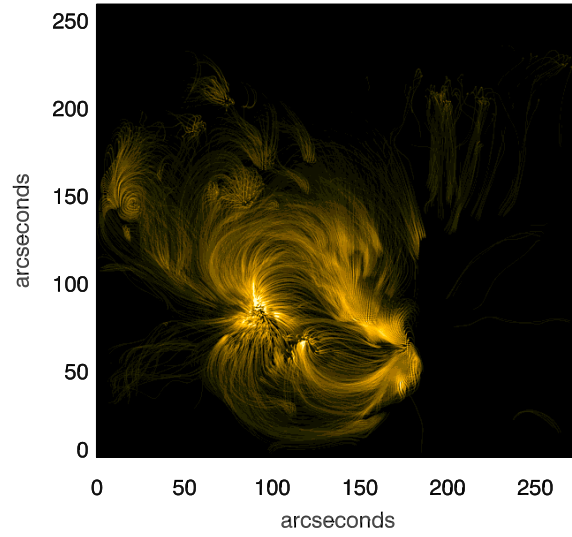

Figure 5.6: Example of an active region NOAA 11897 modelled in SDO/AIA 171 Å filter for $\beta = 0.5$.

Figure 5.7: Example of an active region NOAA 11897 modelled in SDO/AIA 335 Å filter for $\beta = 0.5$.

limitations of the model. Firstly, the longer loops on the right hand side and in the bottom left hand corner are not modelled in the artificial image because they leave the volume of the modelled data cube, hence the black areas of this image in Fig. 5.5. These long loops are either open magnetic field lines or they close outside the modelled volume. Very short loops, not reaching 2 Mm height, are also not included. There is also background emission possibly from the coronal moss which is not modelled in the artificial image, as this is coming from the legs of the hot loops that are not present in the assumed model due to centring the peak temperature distribution around 1.0 MK.

5.3   Results

This model can now be used to test different heating rates and to compare their effects on the emission to EUV observations of the active region. This was initially done by comparing the images by eye to see which heating parameters gave the best match. In Fig. 5.6 the value of β was 0.5, this was chosen as it gave a distribution of bright loops that was the closest match to the observed image.

We also modelled the active region in AIA's 335 Å filter, this was initially performed using a value for $\beta = 0.5$, as this was the value of β that appeared to shown the best representation of the active region in the 171 Å band. This is shown in Fig. 5.7, and can be compared with the AIA observation in Fig. 5.8. This does not appear to provide an accurate representation of the active region in the 335 Å band. Whilst the AIA image shows most
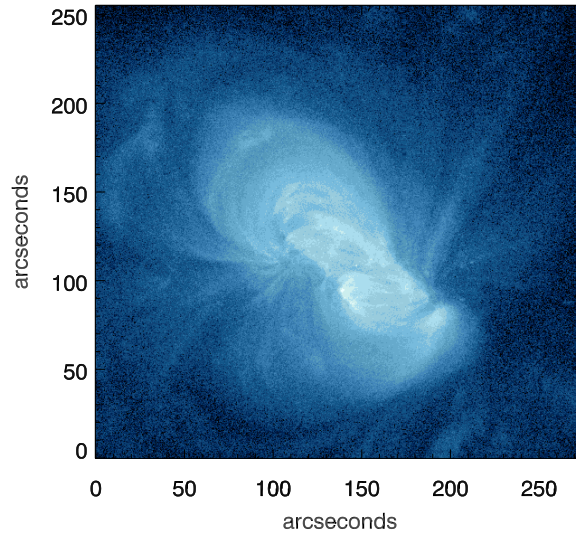
Figure 5.8: SDO/AIA image of active region NOAA 11897 in 335 Å filter, observed on 4th November 2013.

of the emission concentrated in the centre of the active region, it appears as though there is a hotter core of loops emitting at 335 Å beneath those cooler loops observed in 171Å. This behaviour is not reproduced in the modelled active region, here the emitting loops are similar to those that were emitting at 171 Å, with most of the emission coming from longer loops around the edge of the core of the active region. This suggests that whilst $\beta = 0.5$ is a sensible value to model the 171 Å emission a different value may have to be used to model 335 Å emission.

Testing various values for β to determine which appears to best reproduce the observed 335 Å emission leads to Fig. 5.9, which shows the active region modelled using $\beta = 1.5$. This provides a much more accurate looking representation of the active region, now more of the emission is originating from the shorter more central loops, some of which have become fairly bright. There is also still a faint emission from the longer outer loops, which is also seen in the observed image.

5.4 Conclusions

In this chapter we have described a model for a static, well isolated active region, which allows an arbitrary heating rate. This enables a quick comparison with observations of active regions, most notably observations made using SDO/AIA.

The first stage of the modelling was to model the coronal magnetic field using a non-linear
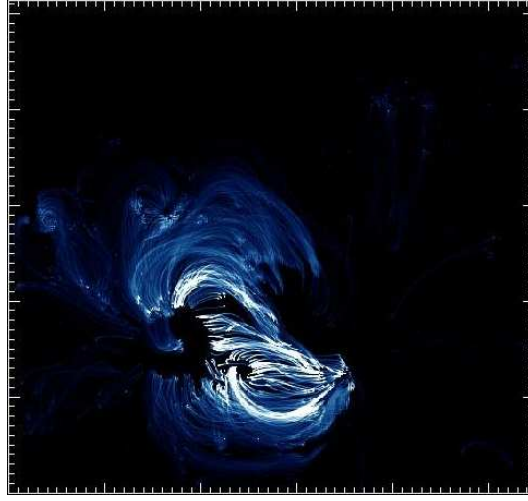
82

Figure 5.9: Example of an active region NOAA 11897 modelled in SDO/AIA 335 Å filter for $\beta = 1.5$.

force-free extrapolation from vector magnetogram data produced by SDO/HMI. The extrapolation was performed using the optimisation approach developed by Wiegelmann et al. [2012], this approach was found to be the most accurate model in a test of various NLFF models performed by Schrijver et al. [2006]. The model works by "relaxing" an initial potential field-model to a force free one that matches the full vector boundary conditions. This model allows us to accurately model the coronal magnetic field of any reasonably magnetically isolated active region that is not too far from the disk centre.

The next stage of the model is to convert the magnetic field data into loops. This is performed by tracing the magnetic field from every point in the bottom boundary of the magnetic field model. This allows us to determine the magnetic field line coming through any given spatial point. Not all of these loops were found to be useful however, and several of them are discarded. Those which leave through the top or side boundaries of the modelled region are discarded as the hydrostatic model assumes that the loops start and end in the photosphere. Those which are not long enough for the hydrostatic model to properly model are discarded as well.

Once the loops have all been defined properly, the plasma which they contain is then modelled using a hydrostatic model developed by van Ballegooijen, it is described in Schrijver and van Ballegooijen [2005]. For each loop it solves the energy balance equation for the given heating rate. The model allows the heating rate to be freely chosen, it is at this point that the heating rate is specified.

Finally the EUV emission for the modelled plasma can now be estimated. Given the density and temperature of the plasma calculated by the hydrostatic model the emission in a given

filter along each loop can be calculated using the filter's response function. These calculated intensities are then projected into the plain as they would be observed by SDO/AIA. These artificial images can then be compared with AIA observations of the active region, in each of AIA's filters. Initially the 171 Å filter was modelled, and an appropriate value for $\beta \sim 0.5$ was identified by comparing the various images by eye. This was performed by ensuring that the parts of the active region where more of the emission originated were also brighter in the artificial image. This value of β does not however appear to be able to accurately reproduce the active region in the 335 Å filter, instead a different value of $\beta \sim 1.5$ gives a more accurate reproduction.

It is possible that this discrepancy has been caused as values of $\beta > 1$ preferentially heat the shorter loops in the centre of the active region, whereas smaller values of β heat the longer loops preferentially. This suggests that the current chosen form of the heating rate may not be able to fully explain the heating of these structures, further study may require an examination of different forms of the heating function.

In order to further this investigation a more rigorous attempt must be made to compare the modelled and observed images. As the geometry of the modelled and observed active region does not exactly align it is very challenging to perform a quantitative comparison of these images. It is however possible to identify single loops and to observe the effect that varying the heating rate has on their emission.

Chapter 6

Investigating the behaviour of single loops in the model

6.1 Introduction

In this chapter, we use the model for an active region developed in the previous chapter to study single loops from the modelled active region in more depth. This was initially motivated as using the full active region models in the previous chapter it was not possible to form a qualitative comparison with the images of those active regions. Only considering single loops at a time provides a better understanding of how the model behaves when varying the parameters of the heating rate. Which allows us to consider specific observable parameters which could be used as diagnostics of the coronal heating function.

Initially this allows us to confirm that the hydrostatic model is behaving in the expected manner, by observing the effect that varying the heating rate in a simple manner for a model of a typical loop has on the modelled emission from that loop.

We can then proceed to develop a diagnostic for the heating rate by varying a key heating parameter and considering the variation in modelled emission caused by this change to discover an observable variation in the emission.

We are also able to consider loops with different magnetic field strengths along their length, observing the effect that shape and magnitude of a loop's magnetic field has on its modelled emission.

The chapter is arranged as follows: first, we discuss how the model was set up to consider single loops, and which loops were analysed, as well as describing those loops. Then, we discuss the results of modelling these loops with different heating rates. Finally we present our conclusions.
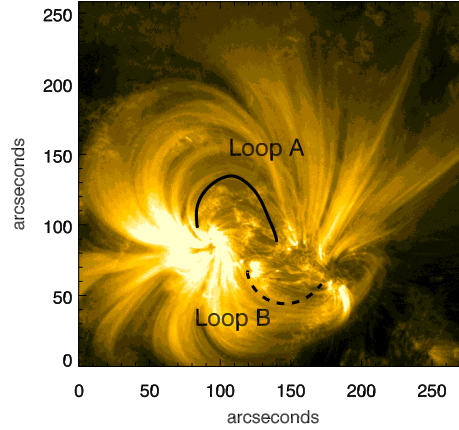
Figure 6.1: SDO/AIA image of active region NOAA 11897 in 171 Å filter, observed on 4th November 2013. Black lines show the NLFF modelled loops that were studied further. The solid line is loop A, the dashed line is loop B. Loops C and D which are are also considered in this chapter are not shown on this plot for clarity.

6.2 Method

The model used in this chapter is the same as the model described in chapter 5. It is, however, only used to model a single loop in the active region at any one time. As the NLFF modelling for the active region has already been performed the magnetic field data can be used to identify loops which are good candidates for individual modelling, as well as providing the magnetic field strength along the loop.

Fig. 6.1 shows an AIA 171 image for the considered active region. From the modelled magnetic field four loops were chosen for further study. For clarity, only two of these loops, denoted A and B, are shown in Fig. 6.1. The magnetic field strengths along all four loops are shown in Fig. 6.2. Loop A is in the upper fan of loops in this active region, whilst loop B is in the downward fan. Loop B is fairly short, $\sim$ 75 Mm and its magnetic field appears to be very symmetric about the loop top, as well as fairly strong at its footpoints, with a magnetic field strength $\sim$ 1300 G. Loop A by contrast is slightly longer, $\sim$ 100 Mm with a weaker and much less symmetric field, $\sim$ 500 G in one footpoint and $\sim$ 280 G in the other footpoint. Loop C is an example of a longer loop, in a similar location in the active region to loop B, but 150 Mm in length and has a magnetic field strength slightly larger than loop A. Loop D is the shortest of the four loops, at roughly 40 Mm long. It is located close to loop B in the active region, and its magnetic field strength distribution differs from the other three loops, as will be discussed in Section 6.3.2. Loops C and D allow us to consider
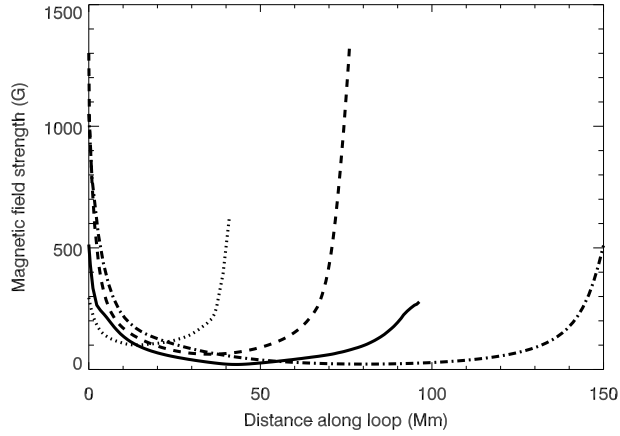
Figure 6.2: The magnetic field strength along loop A (solid line), loop B (dashed line), loop C (dot-dashed line) and loop D (dotted line). These linestyles are kept consistent throughout this paper.

the effect of varying the loop length. All four loops have magnetic fields strengths fairly typical for loops in this active region.

6.3 Results

6.3.1 EUV emission in coronal loops

Fig. 6.3 shows the emission in the Fe xvi 335 Å line along loop B for a fixed value of $\beta = 0.5$, but varying Q_a. The values of Q_a were selected so as to fix the peak temperature in the loop at: $T_e = 1.5, 1.75, 2.0, 2.25$ and 2.5 MK. The peak of emission is initially located at the top of the loop, with very limited emission towards the footpoints for lower peak temperatures. This is due to the plasma at the centre of the loop being close to the peak response of the line, whilst the plasma closer to the footpoints is too cool to significantly emit at this wavelength. As the peak temperature increases, the proportion of the loop significantly emitting increases too, as when T_e along the loop increases a larger segment of the loop becomes hot enough to emit at this wavelength. As the peak temperature rises further the emission at the top of the loop drops off, and two peaks of emission form and move towards the footpoints of the loop. This is due to the top of the loop becoming too hot to emit significantly at this wavelength, and the plasma of a more appropriate temperature being located towards the footpoints. This overall behaviour coincides with results described in Fludra and Ireland [2003], and suggests that the model is behaving in a physically realistic manner. This behaviour can also be reproduced by modelling the 335 Å AIA and 171 Å
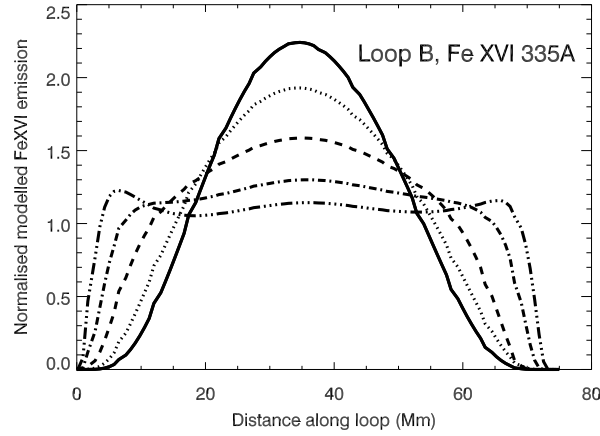
Figure 6.3: The variation of modelled emission in the spectral line Fe xvi 335 Å along loop B for $\beta = 0.5$. The solid line has a peak temperature of 1.5 MK, the dotted line 1.75 MK, the dashed line 2.0 MK, the dot-dashed line 2.25 MK and the triple dot-dashed 2.5 MK. In this plot the emission for each temperature is normalised such as the mean emission along the loop is equal to unity.

AIA filters, however it is not as pronounced as the emission peak for these filters is much broader than the pure Fe xvi (which is the primary ion in the 335 Å AIA filter).

It is of more interest for the diagnostic of the heating mechanism to consider the effect that varying β has on the modelled loops. Figs. 6.4-6.7 show the plasma parameters for loop B and how they vary with β for a fixed peak temperature $T_e = 2$ MK, as well as modelled emission in the Fe xvi 335 Å spectral line and the AIA 335 channel. As β increases, the distribution of temperature along the loop becomes a little broader as more heating is focused towards the footpoints which become hotter for larger values of β. For the highest value of $\beta = 0.75$ the asymmetry of the magnetic field has caused the temperature distribution to become asymmetric with the peak temperature now occurring at ~ 20 Mm, whilst the plasma at the centre of the loop is now ~ 1.8 MK. This has caused the peak of Fe xvi emission to shift to ~ 30 Mm. For most of the considered values of β, the peak of emission is located at the centre of the loop which steadily expands as β increases, in the same manner as the temperature.

The most noticeable change is the increase of the electron density with β which changes by a factor of ~ 2.5 at the loop top. As discussed later, this will lead to our most important diagnostics of the heating mechanism.

There is little variation in the shape of the normalised AIA 335 emission with β as this filter has a fairly broad temperature response and is more influenced by the density distribution, which retains a broadly similar shape, though the values do vary this does not
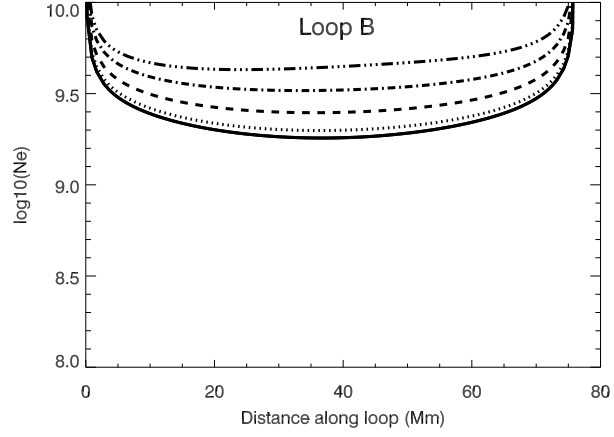
Figure 6.4: Results of modelling loop B for different values of β and the peak temperature fixed at 2 MK. The solid line represents $\beta = -2.0$, the dotted line $\beta = -1.0$, the dashed line $\beta = 0.0$, the dot-dashed line $\beta = 0.5$, the triple dot-dashed line $\beta = 0.75$. The electron density along the loop is shown for these different parameters.
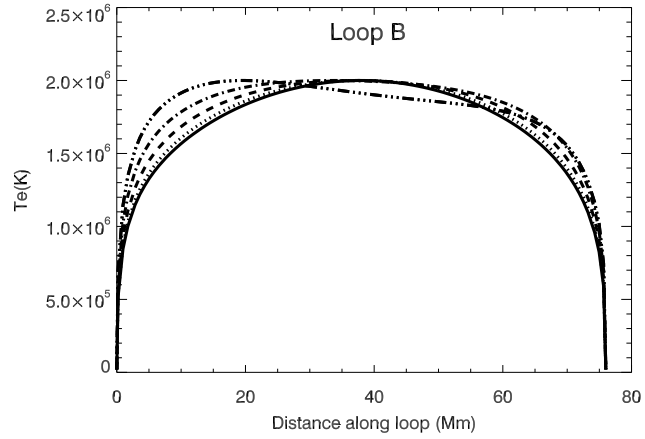

Figure 6.5: Results of modelling loop B for different values of β and the peak temperature fixed at 2 MK. The solid line represents $\beta = -2.0$, the dotted line $\beta = -1.0$, the dashed line $\beta = 0.0$, the dot-dashed line $\beta = 0.5$, the triple dot-dashed line $\beta = 0.75$. The electron temperature along the loop is shown for these different parameters.
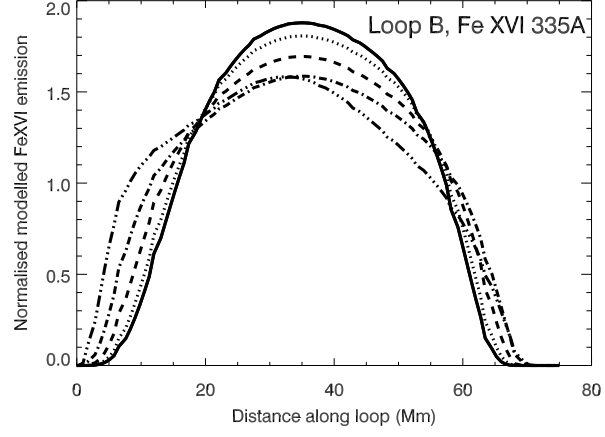
Figure 6.6: Results of modelling loop B for different values of β and the peak temperature fixed at 2 MK. The solid line represents $\beta = -2.0$, the dotted line $\beta = -1.0$, the dashed line $\beta = 0.0$, the dot-dashed line $\beta = 0.5$, the triple dot-dashed line $\beta = 0.75$. The Fe xvi 335 Å emission along the loop is shown for these different parameters.
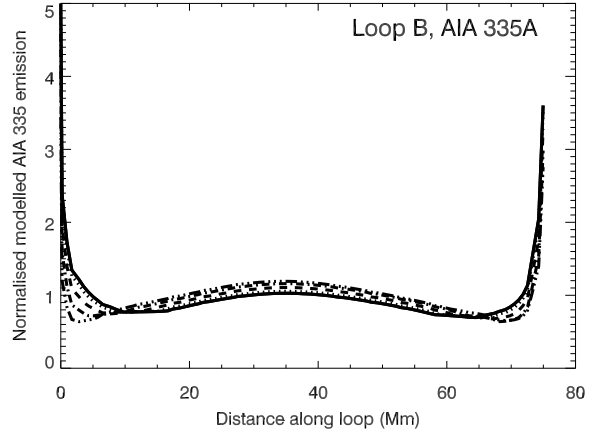

Figure 6.7: Results of modelling loop B for different values of β and the peak temperature fixed at 2 MK. The solid line represents $\beta = -2.0$, the dotted line $\beta = -1.0$, the dashed line $\beta = 0.0$, the dot-dashed line $\beta = 0.5$, the triple dot-dashed line $\beta = 0.75$.

Figure 6.8: Results of modelling loop B for different values of β and peak temperature fixed at 1 MK. The solid line represents $\beta = -2.0$, the dotted line $\beta = -1.0$, the dashed line $\beta = 0.0$, the dot-dashed l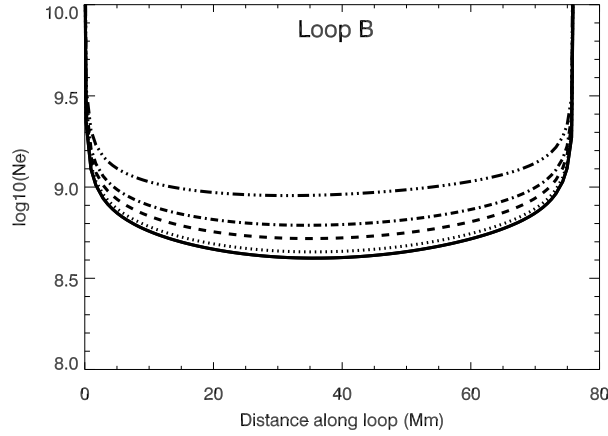ine $\beta = 0.5$, the triple dot-dashed line $\beta = 1.0$. The electron density along the loop is shown for these different parameters.

affect this plot as the emission is normalised. The AIA 335 response is sensitive to low temperatures, hence the emission near loop footpoints is strongly increased.

Figs. 6.8-6.11 show a similar series of plots, but for the AIA 171 filter and the Fe IX 171 Å line, and with a lower loop peak temperature, 1 MK. The lower temperature was chosen as it is close to the peak response of this filter. The behaviour of the temperature and density is broadly the same as in the 2 MK case. As β increases there is a broadening of the temperature peak, until for the largest value of $\beta = 1.0$ the temperature distribution becomes fairly asymmetric. A similar behaviour is also seen in the density distribution as with the hotter case, with the density steadily increasing with β by up to a factor of ~ 3, and becoming asymmetric for the largest value of β. The plasma parameters are then combined with the temperature response function for the AIA 171 filter. As before for the largest value of β there is a high degree of asymmetry, as well as a noticeable asymmetry for $\beta = 0.5$. Unlike the Fe XVI case, the asymmetry in the modelled AIA 171 emission has the opposite behaviour to that of the temperature asymmetry, with the emission peak towards the cooler end of the loop. This is caused as the chosen peak temperature for these loops is above the peak response of the filter (the peak response temperature for AIA 171 is $\log(T_e) = 5.8$ [Lemen et al., 2012]), so the cooler plasma emits more.

This modelling was also performed for loop A. The overall behaviour of the plasma parameters in both loops is similar. As the asymmetry is more pronounced in the magnetic field for loop A, the modelled emission is more asymmetric, particularly the modelled Fe XVI emission.
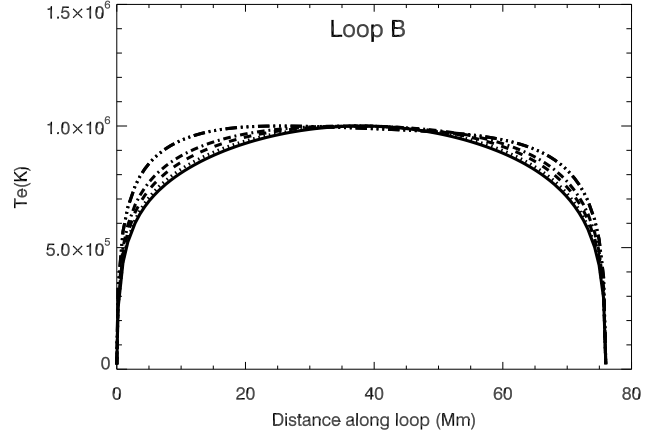
Figure 6.9: Results of modelling loop B for different values of β and peak temperature fixed at 2 MK. The solid line represents $\beta = -2.0$, the dotted line $\beta = -1.0$, the dashed line $\beta = 0.0$, the dot-dashed line $\beta = 0.5$, the triple dot-dashed line $\beta = 1.0$. The electron temperature along the loop is shown for these different parameters.
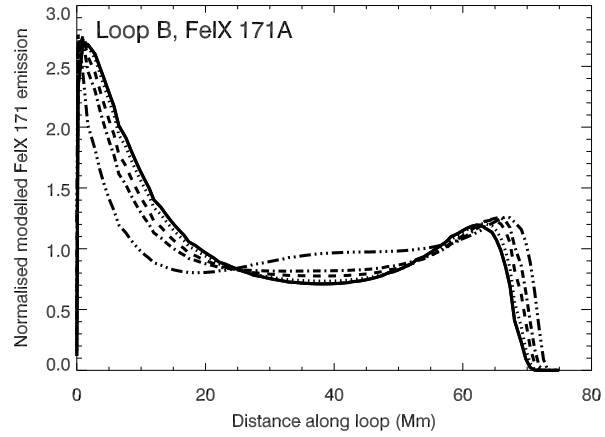

Figure 6.10: Results of modelling loop B for different values of β and peak temperature fixed at 2 MK. The solid line represents $\beta = -2.0$, the dotted line $\beta = -1.0$, the dashed line $\beta = 0.0$, the dot-dashed line $\beta = 0.5$, the triple dot-dashed line $\beta = 1.0$. The Fe IX 171 Å emission along the loop is shown for these different parameters.
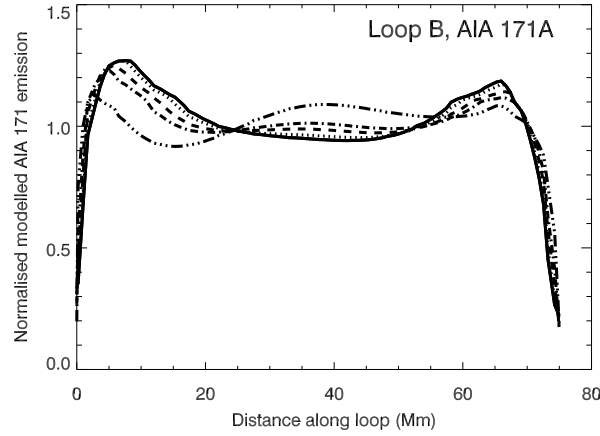
Figure 6.11: Results of modelling loop B for different values of β and peak temperature fixed at 1 MK. The solid line represents $\beta = -2.0$, the dotted line $\beta = -1.0$, the dashed line $\beta = 0.0$, the dot-dashed line $\beta = 0.5$, the triple dot-dashed line $\beta = 1.0$. The SDO/AIA 171 Å band emission along the loop for these different parameters.

6.3.2 Diagnostics of the heating function

The aim of this chapter is to develop a diagnostic technique to identify the power index, β, by comparing these models to coronal images. We are seeking to develop a measurable quantity that could provide a quantifiable comparison. We are comparing loops with the same maximum temperature as the EUV filters will only show loops which have similar temperatures.

There are two possible diagnostics to consider: one diagnostic would compare changes of the distribution of the EUV emission along the loop, the other would measure the change of the total intensity.

Figures 6.11 and 6.7 show the normalised intensity along the loop for different values of β both for the AIA bands 171 and 335. While there are some differences between these distributions, they appear to be too small to distinguish between different values of β, especially in the expected presence of measurements errors in real data. The same normalised intensity distributions for the pure Fe IX 171 and Fe XVI 335 Å line emission are shown in Figures 6.10 and 6.6. We conclude that the normalised spatial distributions along the loops are too similar to provide the required diagnostics. Whilst the spatial emission along the loop modelled as from the pure ions is slightly more sensitive to variations in β, overall it is still not sensitive enough to be a useful diagnostic.

The next measure to be considered was the total emission of each loop, and how this behaves with a varying value of β. The intensity for all points along the loop was summed,
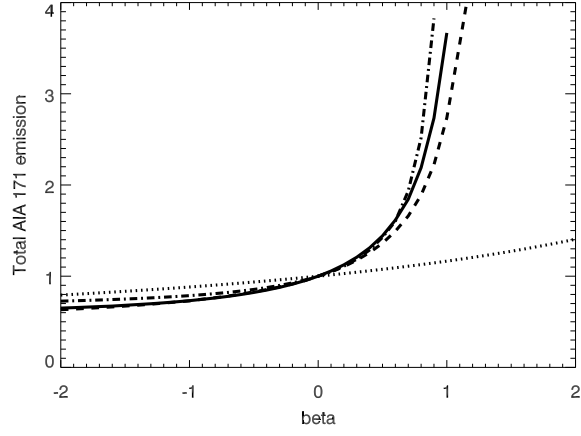
Figure 6.12: The variation of total modelled emission with β for the AIA 171 band. Solid line is loop A, dashed line is loop B, dot-dashed line is loop C and dotted line is loop D.

Figure 6.13: The variation of total modelled emission with β for pure Fe IX. Solid line is loop A, dashed line is loop B, dot-dashed line is loop C and dotted line is loop D.

Figure 6.14: The variation of total modelled emission with β for the AIA 335 band. Solid line is loop A, dashed line is loop B, dot-dashed line is loop C and dotted line is loop D.
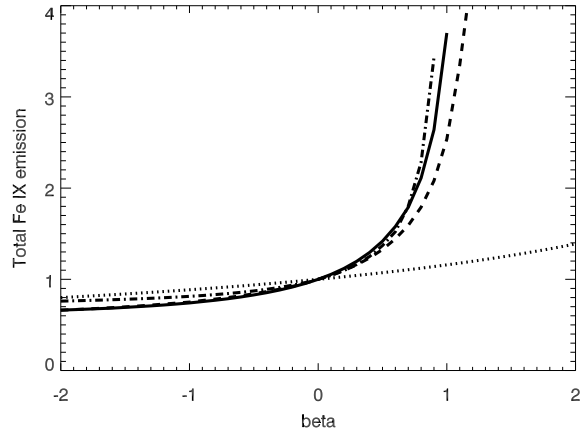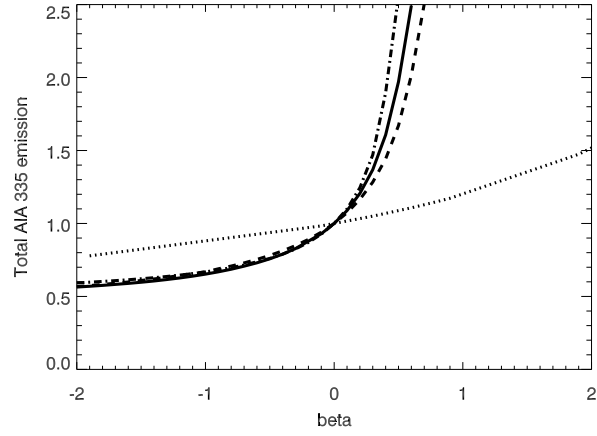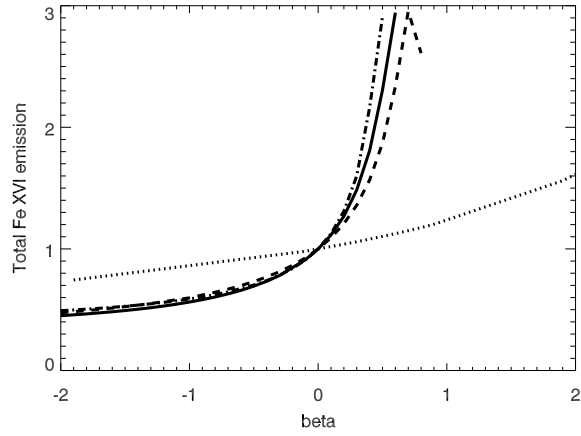

Figure 6.15: The variation of total modelled emission with β for pure Fe xvi. Solid line is loop A, dashed line is loop B, dot-dashed line is loop C and dotted line is loop D.

giving the total emission along the loop for each considered band. These are shown for all four loops in Figs. 6.12-6.15. It was found that the behaviour for loops A, B and C was similar, whereas loop D shows somewhat different behaviour. Therefore, we will initially limit discussion to loops A, B and C. As β increases from 0 to 1, for loops A, B and C, the total intensity for all lines rises steeply by over a factor of roughly 3, being clearly sensitive to β (i.e. to the increasing concentration of heating towards the footpoints). Finally as β increases towards and beyond 1 the model is unable to find a stable solution for these loops, and therefore these lines stop on the plots, this instability is discussed in more detail in section 6.3.3. Therefore, this appears to be a promising diagnostic of β. In contrast, for values of β decreasing from 0 to -2, there is only a $\sim$ 40% decrease in the total intensity. As the heating distribution changes from a uniform heating to one concentrated near the loop top, the conductivity efficiently redistributes the heat along the loop. While the 40% change between $\beta = -2$ and $\beta = 0$ is measurable, the error bars on the derived β in this range would be significantly greater than in the range $0 < \beta < 1$. We note that the curves in Figs. 6.12-6.15 are normalised to 1 for $\beta = 0$. Therefore, the variation of the absolute total intensity with β is not shown in these figures.

We have found that the dependence of the total loop intensity on β is related to how the magnetic field strength varies along the loop. The magnetic field strengths of all of the loops we have considered could be reasonably modelled as the sum of an exponentially decaying component and a constant component. Loops A, B and C have a magnetic field which steeply decreases with height, with a low level of the constant component. When this type of the dependence of $B(s)$ is scaled to a shorter loop length, the resulting $I_{tot} - \beta$ dependence is very similar, with the loss of stable solutions close to $\beta = 1$ (see section 6.3.3). The magnetic field along loop D, however, has a significantly higher level of the constant component, which increases the range of β for which stable solutions exist. In the extreme case, if the magnetic field strength is nearly constant along the loop, the heating rate $B(s)^{\beta}$ would vary very little along the loop even for large values of β, resembling the case of nearly constant heating rate. Such loops are found to have stable solutions up to large values of $\beta > 10$ but offer very little diagnostics capability in the range $0 < \beta < 2$. A survey of a number of loops in the active region under study reveals that such loops with a flat distribution of $B(s)$ indeed appear to exist, particularly for shorter lengths below 60 Mm. Whether this comes from the complexity of the magnetic field in the active region core or from an inadequate spatial resolution of our 3D data cube is not clear. Therefore, the diagnostics presented in Figs. 6.12-6.15 is applicable only to some of the loops with steeply decreasing $B(s)$ and a low constant component of $B(s)$.

The effect of varying the loop length on the total emission was further tested by taking loop B, and scaling its length by various factors - the effect of this is shown in

Fig. 6.16. The peak temperature here was kept fixed at 1 MK, hence the shape of the temperature distribution remains similar for the different loop sizes. However, the density decreases substantially with the loop length, and since EUV line intensities are proportional to the square of the density, this shows that increasing the loop length causes the total emission from the loop to decrease rapidly, as shown in Figs. 6.17-6.20. For example, a change of length from 40 Mm to 250 Mm decreases the total Fe IX 171 Å line intensity by a factor of ~ 10. This is greater than the maximum change of the total intensity caused by the variation of β (Figs. 6.17-6.20). Therefore, the loop length must be measured accurately to allow the diagnostics of β from Figs. 6.17-6.20.

6.3.3 Loss of stable solutions

In Figs. 6.17-6.20 we restricted the range of β to below 1.2. The reason is that for larger values of β the hydrostatic code does not find a stable solution for loops A, B and C. Schrijver and van Ballegooijen [2005] also pointed out that for certain heating rates there is no steady solution of the energy balance equation. We investigate how the loss of stability depends on the maximum loop temperature and the loop length. Fig. 6.21 shows the largest maximum temperature for each value of β for which a stable solution exists for loops A and B. The plot shows the temperature range $5.0 < \log_{10}(T_e) < 7.0$ as this fully covers the temperature range of interest. Both loops show similar behaviour, with the maximum allowable temperature rapidly dropping from above $\log_{10}(T_e) = 7.0$ to just ~ 6.3, i.e. ~ 2 MK, in the range $0.6 < \beta < 1.0$. The curves then flatten out as β increases to ~ 1.5, before falling away below the temperature of interest.

This thermal instability occurs as the heating becomes more concentrated towards the footpoints. As more heating is located at the footpoints the peak temperature is no longer located at the top of the loop, which leads to coronal condensation, and a rapid cooling of the plasma at the peak of the loop. The loop then undergoes a condensation–evaporation cycle with significant plasma flows [Mok et al., 2008]. This instability was studied analytically by Serio et al. [1981], for a half-loop with an exponentially decreasing heating function. They found that the loops became unstable when the scale height of the heating rate, S_H, was roughly one third the loop half length. We postulate that this is the same instability that is causing our loops to become unstable at higher temperatures and values of β. Unfortunately, a direct comparison to this criterion is not possible as a pure exponential function is not a good fit to our heating rate. We have found that the exponential component of the magnetic field strength has a scale height of ~ 2.8 Mm in one of the footpoints of loop B. For other loops we found values of around ~ 5 to ~ 10 Mm. These values are much smaller than the $L/3$ suggested by Serio et al. [1981]. However, the constant component of $B(s)$ ensures that there is always a significant portion of heating occurring at the loop apex and therefore the

exponential component must be significantly steeper to trigger the instability.

This study of the existence of static solutions for a given heating rate can also provide information on the nature of the heating mechanism. Table 5 in [Mandrini et al., 2000] provides a list of potential heating mechanisms, and their expected heating rate. This list suggests that DC heating mechanisms tended to have a value of $\beta = 2$, which for the loops we are considering would not provide a static solution. However, the heating rates for AC heating mechanisms usually have values of $\beta \leq 1$, suggesting that these mechanisms could provide static solutions for the loops considered here.

6.4   Conclusions

We have carried out simulations of coronal loops in a solar active region, seeking a diagnostic method for the coronal heating rate. Our aim has been to ascertain whether observations of individual coronal loops made in the EUV band are capable of providing constraints on the coronal heating model. To reduce the number of free parameters and arbitrary assumptions, we have considered a quasi-static model that requires the heating rate as a function of position along the loop. Considerations of temporal variability of the heating that would be required by the dynamic loop models have been deferred to a future paper.

Starting with a photospheric vector magnetogram from SDO/HMI, the coronal magnetic field was modelled using an NLFF extrapolation code. The geometry of this field was compared to an SDO/AIA 171 image of the same active region, and four loops that matched well were identified. The plasma in these loops was then modelled using a 1D hydrostatic model capable of applying an arbitrary heating rate as a function of magnetic field strength along the loop. From the plasma parameters derived from this model, estimates of the EUV emission in four wavelengths: SDO/AIA 171 and 335 bands, and pure Fe IX and Fe XVI spectral lines were made along the loop. The heating rate was then varied as a function of the power index β (Eq. 5.9), and the effect this variation has on the modelled EUV emission was observed.

We find the following characteristics of the modelled EUV emission, similar in loops with peak temperatures of 1 MK and 2 MK:

1. The distribution of the EUV intensities along the loop varies relatively little as a function of the power index β, therefore the shape of these distributions does not allow us to identify whether the heating is concentrated near the footpoints or the loop-top.

2. The total intensity of the EUV emission summed along the loop is much more sensitive to β. The range of sensitivity for β depends on the shape of the distribution of the magnetic field strength along the loop. For steeply decreasing $B(s)$ and lower $B(s)$ near the loop-top, the achievable diagnostic range is $0 < \beta < 1$, where the total intensity increases

by over a factor of 3. This provides a clear distinction between a uniform heating and the heating concentrated near the footpoints, and allowing the measurement of the value of β. For the heating concentrated near the loop top ($-2 < \beta < 0$), the change of the total intensity is up to 40% — this is measurable but due to the flat nature of this part of the curve the error bars on the determined values of β would be much larger.

3. For this category of loops, when the heating becomes strongly concentrated near the footpoints ($\beta > 1$), there are no more stable solutions.

4. For loops with a flat distribution of $B(s)$ over a significant portion of the loop, the range of β for which stable solutions exist increases and can reach values from 4 to 16 as $B(s)$ becomes progressively more constant. However, values of β greater than 2 are less interesting for the diagnostic of coronal heating, and the normalised intensities for these loops change little for $\beta < 2$ even when the maximum range of β is 4.

5. Loop length provides another factor to consider, as there is a large decrease in density and the absolute total EUV emission for longer loops as shown in Fig. 6.16(b) and Figs. 6.17-6.20. Therefore, the dependence of the total intensity on β needs to be calculated for each value of L.

6. For loops considered in item 2 above, if the heating rate depends locally on the magnetic field as in Eq. 5.9, the heating mechanisms that give stable static solutions ($\beta < 1$) are likely to be AC heating models [Mandrini et al., 2000]. The DC heating models with $\beta = 2$ would lead to non-steady solutions.
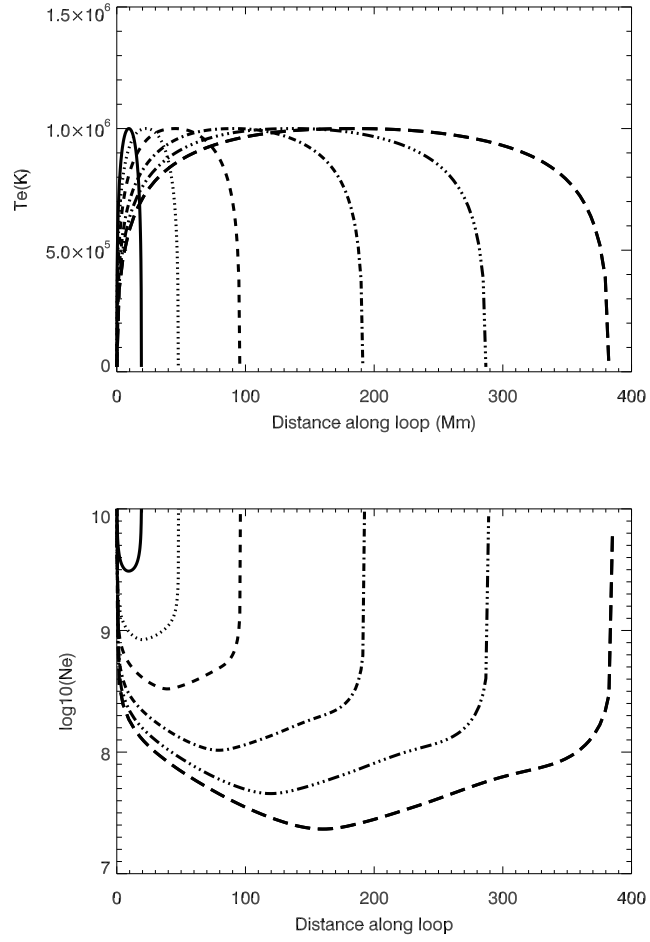
Figure 6.16: Electron temperature (top) and density (bottom) for loops of varying length, produced by scaling loop A. The peak temperature was fixed at 1 MK, and $\beta = 0$. The solid line represents the loop being scaled by a factor of 0.2, the dotted line represents a scaling factor of 0.5, the dashed line: 1, the dot-dashed line: 2, the triple dot-dashed: 3 and the long dashed: 4.

Figure 6.17: The variation of total modelled emission with loop length for the AIA 171 band. This plot is generated by calculating the emission from the scaled loop in Fig. 6.16.

Figure 6.18: The variation of total modelled emission with loop length for pure Fe ix 171 Å. This plot is generated by calculating the emission from the scaled loop in Fig. 6.16.
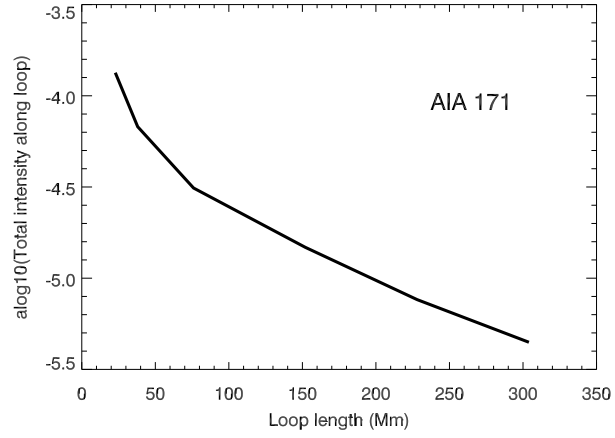
Figure 6.19: The variation of total modelled emission with loop length for the AIA 335 band. This plot is generated by calculating the emission from the scaled loop in Fig. 6.16.
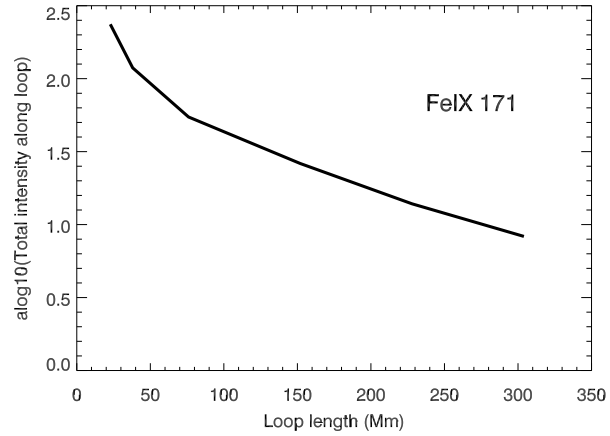

Figure 6.20: The variation of total modelled emission with loop length for pure Fe xvi 335 Å. This plot is generated by calculating the emission from the scaled loop in Fig. 6.16.
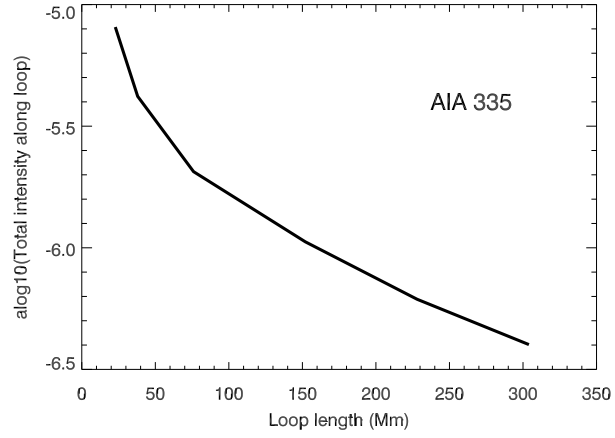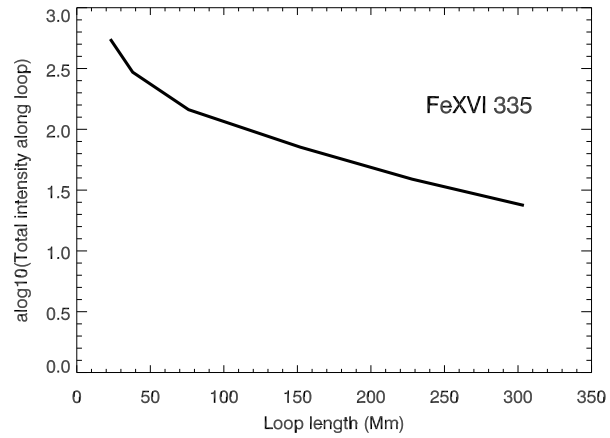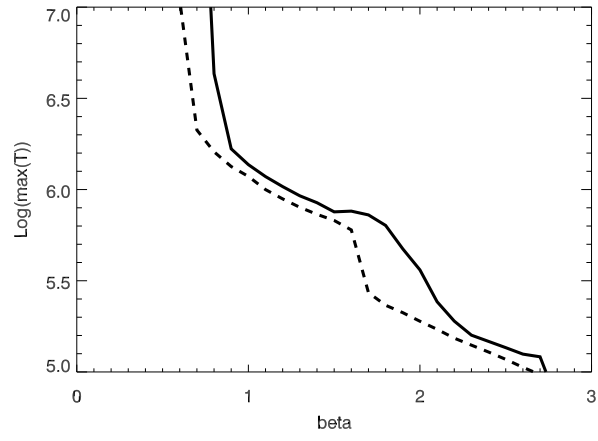
Figure 6.21: The variation in maximum temperature for stable solutions found with this model with β for loop A (continuous line) and loop B (dashed line).

Chapter 7

Conclusions

In this thesis we have broadly considered two distinct areas of Solar Physics research, firstly studying the behaviour of the axisymmetric, or 'Sausage' oscillations of coronal plasma structures. Secondly using a combination of modelling techniques to develop a model for the EUV emission from a coronal active region based on vector magnetogram data of the photosphere.

The common theme through both of these areas has been in developing relatively simple mathematical representations of complex physical problems. This allows these problems to be modelled quickly without using large amounts of processing power. This also allows for a larger parameter space to be explored, which was particularly useful when modelling sausage oscillations.

We will finish by reviewing the work which has been described so far.

7.1   Sausage oscillations

The initial set up considered in the study of sausage oscillations was that of a plasma cylinder. In this we considered a cylinder of denser plasma embedded in a uniform magnetic field aligned with the axis of the cylinder. The variation in magnetic field strength in the radial direction, which is the only direction in which it is varying, gives a variation in the Alfvén speed of the following form:

$$C_A(r) = C_{A\infty} \left[1 - \delta \exp\left(-\frac{r^\alpha}{d^\alpha} \right) \right], \tag{7.1}$$

where $C_A(r)$ is the Alfvén speed, $C_{A\infty}$ is the Alfvén at an infinite radial distance, α is the index of steepness of the Alfvén speed profile, d is the characteristic width of the cylinder.

An important feature of this profile to consider is that as $\alpha \to \infty$ this profile becomes a step profile. This is important as the set up with the step profile has been solved analytically by Zaitsev and Stepanov [1975] and also by Edwin and Roberts [1983].

Using this profile we were able to reduce the problem to a 1-D PDE (2.6), which could easily be solved numerically for a variety of parameters. This allowed us to study how the period of these oscillations varies with longitudinal wavenumber, which is directly related to the length of the loop. We also accounted for the effect that varying the shape of the Alfvén speed profile has on the period.

The main result found in this section was to resolve the long standing discrepancy between analytical results which had been calculated in the strongly leaky regime [Zaitsev and Stepanov, 1982; Kopylova et al., 2002, 2007], and results calculated using models in the weakly leaky regime [Pascoe et al., 2007a; Inglis et al., 2009]. This work was published in Nakariakov et al. [2012].

This approach was then used to verify a novel analytical approximation of the dispersion relation for sausage oscillations.

Analytical approximations for the dispersion relation were found for three regimes: the weakly trapped regime, the weakly leaky regime and the strongly leaky regime. These approximations were developed by performing a Taylor expansion of the dispersion relation about the relevant point and determining the appropriate number of terms to consider. These expansions were then separated into their real and complex components to give expressions for the real and complex parts of the frequency.

The model of the sausage oscillation was then used to generate results to compare with the analytical approximations. The real component of the frequency was compared with the modelled frequency around the cutoff, and in the long-wavelength (strongly leaky) regime. The complex component of the frequency was used to compare with the decay rate of the leaky oscillations. In all regimes a good match was found between the analytical approximations and the model. These results were published in [Vasheghani Farahani et al., 2014]. The final consideration of sausage oscillations involved generalising the model to consider the slab geometry. This was relevant as these oscillations are believe to be present in the corona [Smith et al., 1997; Verwichte et al., 2005; Costa, 2011].

The set up considered here was very similar to that of the cylindrical case. Instead of a cylinder of plasma embedded in a uniform magnetic field, we considered an infinite slab of plasma aligned with the magnetic field. This set up allows a similar form for the Alfvén speed as before, but instead of varying radially it is varying in the direction perpendicular to the slab (the z-direction), its variation is described by (4.2).

This set up allowed the sausage oscillation in the slab geometry to be modelled in the same manner as in the cylindrical geometry. The variation of the period of these oscillations with

the wavelength displayed qualitatively the same behaviour as in the cylindrical case. Over-all it was found that the cylindrical geometry was better able to contain the oscillations, as was in line with expectations. We were also able to compare the cutoff wavelength values to those obtained analytically by considering the dispersion relation, and found them to be a good match.

7.2   Modelling coronal active regions

The other half of this thesis concerns developing a model of a coronal active region. The aim of this was to develop a model that allowed for an arbitrary heating function to be applied, and then the EUV emission of the modelled region could be calculated and compared to EUV observations of the active region which had been made by SDO/AIA.
The initial stage of this process involved modelling the coronal magnetic field. This was done by using a non-linear force free model using the photospheric magnetic field, as measured by SDO/HMI, as the bottom boundary condition. The method used to calculate this model was the optimisation method developed by Wiegelmann et al. [2012].
From this magnetic field model, the underlying loops structures which define the active region were traced. This was done by tracing the magnetic field from the bottom boundary of the modelled region back to the bottom boundary. Each of these loops forms the underlying structure for the rest of the modelling. As well as defining the geometry of the active region. The plasma inside these loops was then modelled using a 1-D hydrostatic model developed by van Ballegooijen [van Ballegooijen, 2004]. This model solved the energy balance equation for the loop given an arbitrary heating rate, the particular heating rate we chose to study was:

$$Q(B) = Q_a \left(\frac{B}{B_{m}ax} \right)^{\beta} L^{\lambda}. \tag{7.2}$$

Finally the EUV emission from these loops needed to be modelled. This was done by using the temperature response function for the AIA filters, which are present in the SolarSoft library for IDL. This function allowed for the emission from each loop to be calculated along its length. The modelled emission for the entire active region was then calculated by projecting each of these loops on to the plane on which they are observed by AIA, and summing their emission.
These modelled AIA images where then compared to observations made by AIA of the modelled active regions. It was found that different values of β were required to model the emission as observed at the 335 Å wavelength and at the 171 Å wavelength. It was also found to be difficult for a direct quantitative comparison of images due to the slight varia-

tion in geometry between the modelled and observed region.

We then proceeded to model individual loops from the active region to gain a more in depth understanding of how their behaviour varies with the variation in the form of the heating rate. This was initially done by keeping β constant and increasing Q_a, the variation in emission from the loop. As the heating, and therefore its temperature, increased followed the expected behaviour.

We then studied the variation in emission as β varied, whilst the peak temperature of the loop was kept constant. Here we found that the overall shape of the emission along the loops did not vary much, however as β increased the overall emission from the loop did increase.

In this section we also considered a limitation of the hydrostatic model, that for certain loops and certain heating rates it is not possible to find a static solution. This of course reflects reality in that applying these heating rates would not lead to a stable loop. It is of some interest to note for which heating rates the model cannot find a stable solution. Our findings here agreed with the earlier work of Serio et al. [1981].

We conclude here the possibility of using the total overall emission for the loop as a diagnostic for the coronal heating rate, as it has showed a reasonable sensitivity to the parameter β.

7.3 Conclusion

Through this thesis various mathematical techniques have been used to model a wide range of processes in the corona. These techniques have led to useful new results which further our understanding of the many complex processes which are occurring throughout the corona.

Bibliography

M. Abramowitz, I. A. Stegun, and R. H. Romer. Handbook of Mathematical Functions with Formulas, Graphs, and Mathematical Tables. *American Journal of Physics*, 56:958–958, October 1988. doi: 10.1119/1.15378.

J. J. Aly. On the reconstruction of the nonlinear force-free coronal magnetic field from boundary data. Sol. Phys., 120:19–48, March 1989. doi: 10.1007/BF00148533.

T. Amari, J. J. Aly, J. F. Luciani, T. Z. Boulmezaoud, and Z. Mikic. Reconstructing the Solar Coronal Magnetic Field as a Force-Free Magnetic Field. Sol. Phys., 174:129–149, August 1997. doi: 10.1023/A:1004966830232.

A. Asai, M. Shimojo, H. Isobe, T. Morimoto, T. Yokoyama, K. Shibasaki, and H. Nakajima. Periodic Acceleration of Electrons in the 1998 November 10 Solar Flare. ApJ, 562:L103–L106, November 2001. doi: 10.1086/338052.

M. J. Aschwanden. Theory of radio pulsations in coronal loops. Sol. Phys., 111:113–136, March 1987. doi: 10.1007/BF00145445.

M. J. Aschwanden. A Nonlinear Force-Free Magnetic Field Approximation Suitable for Fast Forward-Fitting to Coronal Loops. I. Theory. Sol. Phys., 287:323–344, October 2013. doi: 10.1007/s11207-012-0069-7.

M. J. Aschwanden and L. W. Acton. Temperature Tomography of the Soft X-Ray Corona: Measurements of Electron Densities, Tempuratures, and Differential Emission Measure Distributions above the Limb. ApJ, 550:475–492, March 2001. doi: 10.1086/319711.

M. J. Aschwanden, R. W. Nightingale, and D. Alexander. Evidence for Nonuniform Heating of Coronal Loops Inferred from Multithread Modeling of TRACE Data. ApJ, 541: 1059–1077, October 2000. doi: 10.1086/309486.

M. J. Aschwanden, V. M. Nakariakov, and V. F. Melnikov. Magnetohydrodynamic Sausage-Mode Oscillations in Coronal Loops. ApJ, 600:458–463, January 2004. doi: 10.1086/379789.

D. Banerjee, R. Erdélyi, R. Oliver, and E. O'Shea. Present and Future Observing Trends in Atmospheric Magnetoseismology. Sol. Phys., 246:3–29, November 2007. doi: 10.1007/s11207-007-9029-z.

D. Berghmans, F. Clette, and D. Moses. Quiet Sun EUV transient brightenings and turbulence. A panoramic view by EIT on board SOHO. A&A, 336:1039–1055, August 1998.

P. S. Cally. Leaky and non-leaky oscillations in magnetic flux tubes. Sol. Phys., 103: 277–298, February 1986. doi: 10.1007/BF00147830.

H. Carmichael. A Process for Flares. *NASA Special Publication*, 50:451, 1964.

J. W. Cirtain, L. Golub, L. Lundquist, A. van Ballegooijen, A. Savcheva, M. Shimojo, E. DeLuca, S. Tsuneta, T. Sakao, K. Reeves, M. Weber, R. Kano, N. Narukage, and K. Shibasaki. Evidence for Alfvén Waves in Solar X-ray Jets. *Science*, 318:1580–, December 2007. doi: 10.1126/science.1147050.

F. C. Cooper, V. M. Nakariakov, and D. R. Williams. Short period fast waves in solar coronal loops. A&A, 409:325–330, October 2003. doi: 10.1051/0004-6361:20031071.

A. Costa. Topics on shock waves and coronal seismology. *Plasma Physics and Controlled Fusion*, 53(7):074006, July 2011. doi: 10.1088/0741-3335/53/7/074006.

J. L. Culhane, L. K. Harra, A. M. James, K. Al-Janabi, L. J. Bradley, R. A. Chaudry, K. Rees, J. A. Tandy, P. Thomas, M. C. R. Whillock, B. Winter, G. A. Doschek, C. M. Korendyke, C. M. Brown, S. Myers, J. Mariska, J. Seely, J. Lang, B. J. Kent, B. M. Shaughnessy, P. R. Young, G. M. Simnett, C. M. Castelli, S. Mahmoud, H. Mapson-Menard, B. J. Probyn, R. J. Thomas, J. Davila, K. Dere, D. Windt, J. Shea, R. Hagood, R. Moye, H. Hara, T. Watanabe, K. Matsuzaki, T. Kosugi, V. Hansteen, and Ø. Wikstol. The EUV Imaging Spectrometer for Hinode. Sol. Phys., 243:19–61, June 2007. doi: 10.1007/s01007-007-0293-1.

I. De Moortel and V. M. Nakariakov. Magnetohydrodynamic waves and coronal seismology: an overview of recent results. *Royal Society of London Philosophical Transactions Series A*, 370:3193–3216, July 2012. doi: 10.1098/rsta.2011.0640.

I. De Moortel, J. Ireland, and R. W. Walsh. Observation of oscillations in coronal loops. A&A, 355:L23–L26, March 2000.

K. P. Dere, E. Landi, P. R. Young, G. Del Zanna, M. Landini, and H. E. Mason. CHIANTI - an atomic database for emission lines. IX. Ionization rates, recombination rates, ioniza-

tion equilibria for the elements hydrogen through zinc and updated atomic data. A&A, 498:915–929, May 2009. doi: 10.1051/0004-6361/200911712.

J. F. Drake. Characteristics of Soft Solar X-Ray Bursts. Sol. Phys., 16:152–185, January 1971. doi: 10.1007/BF00154510.

J. Dudík, E. Dzifčáková, M. Karlický, and A. Kulinová. Is it possible to model observed active region coronal emission simultaneously in EUV and X-ray filters? A&A, 531: A115, July 2011. doi: 10.1051/0004-6361/201015947.

P. M. Edwin and B. Roberts. Wave propagation in a magnetically structured atmosphere. III - The slab in a magnetic environment. Sol. Phys., 76:239–259, March 1982. doi: 10.1007/BF00170986.

P. M. Edwin and B. Roberts. Wave propagation in a magnetic cylinder. Sol. Phys., 88: 179–191, October 1983. doi: 10.1007/BF00196186.

G. H. Fisher, D. W. Longcope, T. R. Metcalf, and A. A. Pevtsov. Coronal Heating in Active Regions as a Function of Global Magnetic Variables. ApJ, 508:885–898, December 1998. doi: 10.1086/306435.

G. D. Fleishman, Q. J. Fu, G.-L. Huang, V. F. Melnikov, and M. Wang. Discovery of unusual large group delay in microwave millisecond oscillating events. A&A, 385:671–685, April 2002. doi: 10.1051/0004-6361:20020172.

A. Fludra and J. Ireland. Inversion of the intensity-magnetic field relationship in solar active regions. A&A, 398:297–303, January 2003. doi: 10.1051/0004-6361:20021616.

A. Fludra and J. Ireland. Radiative and magnetic properties of solar active regions. I. Global magnetic field and EUV line intensities. A&A, 483:609–621, May 2008. doi: 10.1051/0004-6361:20078183.

A. Fludra and H. Warren. Radiative and magnetic properties of solar active regions. II. Spatially resolved analysis of O V 62.97 nm transition region emission. A&A, 523:A47, November 2010. doi: 10.1051/0004-6361/201014261.

C. Foullon, E. Verwichte, V. M. Nakariakov, and L. Fletcher. X-ray quasi-periodic pulsations in solar flares as magnetohydrodynamic oscillations. A&A, 440:L59–L62, September 2005. doi: 10.1051/0004-6361:200500169.

G. A. Gary, R. L. Moore, M. J. Hagyard, and B. M. Haisch. Nonpotential features observed in the magnetic field of an active region. ApJ, 314:782–794, March 1987. doi: 10.1086/165104.

L. Golub, C. Maxson, R. Rosner, G. S. Vaiana, and S. Serio. Magnetic fields and coronal heating. ApJ, 238:343–348, May 1980. doi: 10.1086/157990.

M. Goossens, J. Andries, R. Soler, T. Van Doorsselaere, I. Arregui, and J. Terradas. Surface Alfvén Waves in Solar Flux Tubes. ApJ, 753:111, July 2012. doi: 10.1088/0004-637X/753/2/111.

M. Gruszecki, V. M. Nakariakov, and T. Van Doorsselaere. Intensity variations associated with fast sausage modes. A&A, 543:A12, July 2012. doi: 10.1051/0004-6361/201118168.

G. Halberstadt and J. P. Goedbloed. Alfven wave heating of coronal loops: photospheric excitation. A&A, 301:559, September 1995.

Mike Hapgood and Alan Thomson. *Space weather: its impact on Earth and implications for business*. Lloyds 360 Risk Insight, 2010.

T. Hirayama. Theoretical Model of Flares and Prominences. I: Evaporating Flare Model. Sol. Phys., 34:323–338, February 1974. doi: 10.1007/BF00153671.

J. T. Hoeksema, Y. Liu, K. Hayashi, X. Sun, J. Schou, S. Couvidat, A. Norton, M. Bobra, R. Centeno, K. D. Leka, G. Barnes, and M. Turmon. The Helioseismic and Magnetic Imager (HMI) Vector Magnetic Field Pipeline: Overview and Performance. Sol. Phys., 289:3483–3530, September 2014. doi: 10.1007/s11207-014-0516-8.

J. V. Hollweg. Resonance absorption of magnetohydrodynamic surface waves Physical discussion. ApJ, 312:880–885, January 1987. doi: 10.1086/164934.

C. Hornsey, V. M. Nakariakov, and A. Fludra. Sausage oscillations of coronal plasma slabs. A&A, 567:A24, July 2014. doi: 10.1051/0004-6361/201423524.

H. S. Hudson. Solar flares, microflares, nanoflares, and coronal heating. Sol. Phys., 133: 357–369, June 1991. doi: 10.1007/BF00149894.

A. R. Inglis, V. M. Nakariakov, and V. F. Melnikov. Multi-wavelength spatially resolved analysis of quasi-periodic pulsations in a solar flare. A&A, 487:1147–1153, September 2008. doi: 10.1051/0004-6361:20079323.

A. R. Inglis, T. van Doorsselaere, C. S. Brady, and V. M. Nakariakov. Characteristics of magnetoacoustic sausage modes. A&A, 503:569–575, August 2009. doi: 10.1051/0004-6361/200912088.

G. W. Inverarity and E. R. Priest. Turbulent coronal heating. III. Wave heating in coronal loops. A&A, 302:567, October 1995.

M. Karlický, H. Mészárosová, and P. Jelínek. Radio fiber bursts and fast magnetoacoustic wave trains. A&A, 550:A1, February 2013. doi: 10.1051/0004-6361/201220296.

A. G. Kislyakov, V. V. Zaitsev, A. V. Stepanov, and S. Urpo. On the Possible Connection between Photospheric 5-Min Oscillation and Solar Flare Microwave Emission. Sol. Phys., 233:89–106, January 2006. doi: 10.1007/s11207-006-2850-y.

J. A. Klimchuk. On Solving the Coronal Heating Problem. Sol. Phys., 234:41–77, March 2006. doi: 10.1007/s11207-006-0055-z.

R. A. Kopp and G. W. Pneuman. Magnetic reconnection in the corona and the loop prominence phenomenon. Sol. Phys., 50:85–98, October 1976. doi: 10.1007/BF00206193.

Y. G. Kopylova, A. V. Stepanov, and Y. T. Tsap. Radial Oscillations of Coronal Loops and Microwave Radiation from Solar Flares. *Astronomy Letters*, 28:783–791, November 2002. doi: 10.1134/1.1518717.

Y. G. Kopylova, A. V. Melnikov, A. V. Stepanov, Y. T. Tsap, and T. B. Goldvarg. Oscillations of coronal loops and second pulsations of solar radio emission. *Astronomy Letters*, 33:706–713, October 2007. doi: 10.1134/S1063773707100088.

J. R. Lemen, A. M. Title, D. J. Akin, P. F. Boerner, C. Chou, J. F. Drake, D. W. Duncan, C. G. Edwards, F. M. Friedlaender, G. F. Heyman, N. E. Hurlburt, N. L. Katz, G. D. Kushner, M. Levay, R. W. Lindgren, D. P. Mathur, E. L. McFeaters, S. Mitchell, R. A. Rehse, C. J. Schrijver, L. A. Springer, R. A. Stern, T. D. Tarbell, J.-P. Wuelser, C. J. Wolfson, C. Yanari, J. A. Bookbinder, P. N. Cheimets, D. Caldwell, E. E. Deluca, R. Gates, L. Golub, S. Park, W. A. Podgorski, R. I. Bush, P. H. Scherrer, M. A. Gummin, P. Smith, G. Auker, P. Jerram, P. Pool, R. Soufli, D. L. Windt, S. Beardsley, M. Clapp, J. Lang, and N. Waltham. The Atmospheric Imaging Assembly (AIA) on the Solar Dynamics Observatory (SDO). Sol. Phys., 275:17–40, January 2012. doi: 10.1007/s11207-011-9776-8.

B. C. Low and Y. Q. Lou. Modeling solar force-free magnetic fields. ApJ, 352:343–352, March 1990. doi: 10.1086/168541.

C. H. Mandrini, P. Démoulin, and J. A. Klimchuk. Magnetic Field and Plasma Scaling Laws: Their Implications for Coronal Heating Models. ApJ, 530:999–1015, February 2000. doi: 10.1086/308398.

112

M. Mathioudakis, J. H. Seiradakis, D. R. Williams, S. Avgoloupis, D. S. Bloomfield, and R. T. J. McAteer. White-light oscillations during a flare on II Peg. A&A, 403:1101–1104, June 2003. doi: 10.1051/0004-6361:20030394.

T. R. Metcalf. Resolving the 180-degree ambiguity in vector magnetic field measurements: The 'minimum' energy solution. Sol. Phys., 155:235–242, December 1994. doi: 10.1007/BF00680593.

T. R. Metcalf, M. L. De Rosa, C. J. Schrijver, G. Barnes, A. A. van Ballegooijen, T. Wiegelmann, M. S. Wheatland, G. Valori, and J. M. McTtiernan. Nonlinear Force-Free Modeling of Coronal Magnetic Fields. II. Modeling a Filament Arcade and Simulated Chromospheric and Photospheric Vector Fields. Sol. Phys., 247:269–299, February 2008. doi: 10.1007/s11207-007-9110-7.

Y. Mok, Z. Mikić, R. Lionello, and J. A. Linker. The Formation of Coronal Loops by Thermal Instability in Three Dimensions. ApJ, 679:L161–L165, June 2008. doi: 10.1086/589440.

R. J. Morton, R. Erdélyi, D. B. Jess, and M. Mathioudakis. Observations of Sausage Modes in Magnetic Pores. ApJ, 729:L18, March 2011. doi: 10.1088/2041-8205/729/2/L18.

G. Mossessian and G. D. Fleishman. Modeling of Gyrosynchrotron Radio Emission Pulsations Produced by Magnetohydrodynamic Loop Oscillations in Solar Flares. ApJ, 748: 140, April 2012. doi: 10.1088/0004-637X/748/2/140.

H. Nakajima, M. Nishio, S. Enome, K. Shibasaki, T. Takano, Y. Hanaoka, C. Torii, H. Sekiguchi, T. Bushimata, S. Kawashima, N. Shinohara, Y. Irimajiri, H. Koshiishi, T. Kosugi, Y. Shiomi, M. Sawa, and K. Kai. The Nobeyama radioheliograph. *IEEE Proceedings*, 82:705–713, May 1994.

V. M. Nakariakov and V. F. Melnikov. Quasi-Periodic Pulsations in Solar Flares. Space Sci. Rev., 149:119–151, December 2009. doi: 10.1007/s11214-009-9536-3.

V. M. Nakariakov and B. Roberts. On Fast Magnetosonic Coronal Pulsations. Sol. Phys., 159:399–402, July 1995. doi: 10.1007/BF00686541.

V. M. Nakariakov and E. Verwichte. Coronal Waves and Oscillations. *Living Reviews in Solar Physics*, 2:3, July 2005. doi: 10.12942/lrsp-2005-3.

V. M. Nakariakov, L. Ofman, E. E. Deluca, B. Roberts, and J. M. Davila. TRACE observation of damped coronal loop oscillations: Implications for coronal heating. *Science*, 285: 862–864, August 1999. doi: 10.1126/science.285.5429.862.

V. M. Nakariakov, V. F. Melnikov, and V. E. Reznikova. Global sausage modes of coronal loops. A&A, 412:L7–L10, December 2003. doi: 10.1051/0004-6361:20031660.

V. M. Nakariakov, C. Hornsey, and V. F. Melnikov. Sausage Oscillations of Coronal Plasma Structures. ApJ, 761:134, December 2012. doi: 10.1088/0004-637X/761/2/134.

U. Narain and P. Ulmschneider. Chromospheric and Coronal Heating Mechanisms II. Space Sci. Rev., 75:453–509, February 1996. doi: 10.1007/BF00833341.

L. Ofman, J. M. Davila, and R. S. Steinolfson. Coronal heating by the resonant absorption of Alfven waves: Wavenumber scaling laws. ApJ, 444:471–477, May 1995. doi: 10.1086/175621.

L. Ofman, M. Romoli, G. Poletto, G. Noci, and J. L. Kohl. Ultraviolet Coronagraph Spectrometer Observations of Density Fluctuations in the Solar Wind. ApJ, 491:L111–L114, December 1997. doi: 10.1086/311067.

E. S. Oran, J. T. Mariska, and J. P. Boris. The condensational instability in the solar transition region and corona. ApJ, 254:349–360, March 1982. doi: 10.1086/159739.

E. N. Parker. Magnetic Neutral Sheets in Evolving Fields - Part Two - Formation of the Solar Corona. ApJ, 264:642, January 1983. doi: 10.1086/160637.

E. N. Parker. Nanoflares and the solar X-ray corona. ApJ, 330:474–479, July 1988. doi: 10.1086/166485.

D. J. Pascoe, V. M. Nakariakov, and T. D. Arber. Sausage oscillations of coronal loops. A&A, 461:1149–1154, January 2007a. doi: 10.1051/0004-6361:20065986.

D. J. Pascoe, V. M. Nakariakov, and T. D. Arber. Sausage Oscillations in Multishell Coronal Structures. Sol. Phys., 246:165–175, November 2007b. doi: 10.1007/s11207-007-9055-x.

D. J. Pascoe, I. de Moortel, and J. A. McLaughlin. Impulsively generated oscillations in a 3D coronal loop. A&A, 505:319–327, October 2009a. doi: 10.1051/0004-6361/200912270.

D. J. Pascoe, V. M. Nakariakov, T. D. Arber, and K. Murawski. Sausage oscillations in loops with a non-uniform cross-section. A&A, 494:1119–1125, February 2009b. doi: 10.1051/0004-6361:200810541.

F. Reale. Coronal Loops: Observations and Modeling of Confined Plasma. *Living Reviews in Solar Physics*, 11:4, July 2014. doi: 10.12942/lrsp-2014-4.

F. Reale, G. Peres, S. Serio, R. M. Betta, E. E. DeLuca, and L. Golub. A Brightening Coronal Loop Observed by TRACE. II. Loop Modeling and Constraints on Heating. ApJ, 535:423–437, May 2000. doi: 10.1086/308817.

B. Roberts. Wave propagation in a magnetically structured atmosphere. I - Surface waves at a magnetic interface. Sol. Phys., 69:27–38, January 1981a. doi: 10.1007/BF00151253.

B. Roberts. Wave Propagation in a Magnetically Structured Atmosphere - Part Two - Waves in a Magnetic Slab. Sol. Phys., 69:39–56, January 1981b. doi: 10.1007/BF00151254.

B. Roberts, P. M. Edwin, and A. O. Benz. On coronal oscillations. ApJ, 279:857–865, April 1984. doi: 10.1086/161956.

R. Rosner and G. S. Vaiana. Hydrostatic and dynamic models of solar coronal holes. ApJ, 216:141–157, August 1977. doi: 10.1086/155455.

R. Rosner, W. H. Tucker, and G. S. Vaiana. Dynamics of the quiescent solar corona. ApJ, 220:643–645, March 1978. doi: 10.1086/155949.

G. Roumeliotis. The "Stress-and-Relax" Method for Reconstructing the Coronal Magnetic Field from Vector Magnetograph Data. ApJ, 473:1095, December 1996. doi: 10.1086/178219.

M. S. Ruderman and B. Roberts. Comment on "Note on the Initial Value Problem for Coronal Loop Kink Waves" By P. S. Cally. Sol. Phys., 237:119–121, August 2006. doi: 10.1007/s11207-006-0192-4.

M. S. Ruderman, D. Berghmans, M. Goossens, and S. Poedts. Direct excitation of resonant torsional Alfven waves by footpoint motions. A&A, 320:305–318, April 1997.

T. Sakurai. Calculation of force-free magnetic field with non-constant α. Sol. Phys., 69: 343–359, February 1981. doi: 10.1007/BF00149999.

P. H. Scherrer, J. Schou, R. I. Bush, A. G. Kosovichev, R. S. Bogart, J. T. Hoeksema, Y. Liu, T. L. Duvall, J. Zhao, A. M. Title, C. J. Schrijver, T. D. Tarbell, and S. Tomczyk. The Helioseismic and Magnetic Imager (HMI) Investigation for the Solar Dynamics Observatory (SDO). Sol. Phys., 275:207–227, January 2012. doi: 10.1007/s11207-011-9834-2.

J. Schou, P. H. Scherrer, R. I. Bush, R. Wachter, S. Couvidat, M. C. Rabello-Soares, R. S. Bogart, J. T. Hoeksema, Y. Liu, T. L. Duvall, D. J. Akin, B. A. Allard, J. W. Miles, R. Rairden, R. A. Shine, T. D. Tarbell, A. M. Title, C. J. Wolfson, D. F. Elmore, A. A.

Norton, and S. Tomczyk. Design and Ground Calibration of the Helioseismic and Magnetic Imager (HMI) Instrument on the Solar Dynamics Observatory (SDO). Sol. Phys., 275:229–259, January 2012. doi: 10.1007/s11207-011-9842-2.

C. J. Schrijver and M. L. De Rosa. Photospheric and heliospheric magnetic fields. Sol. Phys., 212:165–200, January 2003. doi: 10.1023/A:1022908504100.

C. J. Schrijver and A. A. van Ballegooijen. Is the Quiet-Sun Corona a Quasi-steady, Force-free Environment? ApJ, 630:552–560, September 2005. doi: 10.1086/431754.

C. J. Schrijver, A. W. Sandman, M. J. Aschwanden, and M. L. De Rosa. The Coronal Heating Mechanism as Identified by Full-Sun Visualizations. ApJ, 615:512–525, November 2004. doi: 10.1086/424028.

C. J. Schrijver, M. L. De Rosa, T. R. Metcalf, Y. Liu, J. McTiernan, S. Régnier, G. Valori, M. S. Wheatland, and T. Wiegelmann. Nonlinear Force-Free Modeling of Coronal Magnetic Fields Part I: A Quantitative Comparison of Methods. Sol. Phys., 235:161–190, May 2006. doi: 10.1007/s11207-006-0068-7.

R. B. Scott, D. W. Longcope, and D. E. McKenzie. Peristaltic Pumping near Post-coronal Mass Ejection Supra-arcade Current Sheets. ApJ, 776:54, October 2013. doi: 10.1088/0004-637X/776/1/54.

M. Selwa, K. Murawski, and G. Kowal. Three-dimensional numerical simulations of impulsively generated MHD waves in solar coronal loops. A&A, 422:1067–1072, August 2004. doi: 10.1051/0004-6361:20047112.

S. Serio, G. Peres, G. S. Vaiana, L. Golub, and R. Rosner. Closed coronal structures. II - Generalized hydrostatic model. ApJ, 243:288–300, January 1981. doi: 10.1086/158597.

T. Shimizu. Energetics and Occurrence Rate of Active-Region Transient Brightenings and Implications for the Heating of the Active-Region Corona. PASJ, 47:251–263, April 1995.

J. M. Smith, B. Roberts, and R. Oliver. Magnetoacoustic wave propagation in current sheets. A&A, 327:377–387, November 1997.

L. Spitzer. *Physics of Fully Ionized Gases*. 1962.

A. K. Srivastava, T. V. Zaqarashvili, W. Uddin, B. N. Dwivedi, and P. Kumar. Observation of multiple sausage oscillations in cool post-flare loop. MNRAS, 388:1899–1903, August 2008. doi: 10.1111/j.1365-2966.2008.13532.x.

P. A. Sturrock. Model of the High-Energy Phase of Solar Flares. Nature, 211:695–697, August 1966. doi: 10.1038/211695a0.

J. T. Su, Y. D. Shen, Y. Liu, Y. Liu, and X. J. Mao. Imaging Observations of Quasi-periodic Pulsations in Solar Flare Loops with SDO/AIA. ApJ, 755:113, August 2012. doi: 10.1088/0004-637X/755/2/113.

H. P. Summers. *The ADAS manual, version 2-3, http://www.adas.ac.uk/.* 2001.

B. Tan. Observable Parameters of Solar Microwave Pulsating Structure and Their Implications for Solar Flare. Sol. Phys., 253:117–131, December 2008. doi: 10.1007/s11207-008-9235-3.

J. Terradas, R. Oliver, and J. L. Ballester. On the excitation of trapped and leaky modes in coronal slabs. A&A, 441:371–378, October 2005. doi: 10.1051/0004-6361:20053198.

B. J. Thompson, S. P. Plunkett, J. B. Gurman, J. S. Newmark, O. C. St. Cyr, and D. J. Michels. SOHO/EIT observations of an Earth-directed coronal mass ejection on May 12, 1997. Geophys. Res. Lett., 25:2465–2468, 1998. doi: 10.1029/98GL50429.

D. Tsiklauri, M. J. Aschwanden, V. M. Nakariakov, and T. D. Arber. Radiative hydro-dynamic modeling of the Bastille-Day flare (14 July, 2000). I. Numerical simulations. A&A, 419:1149–1158, June 2004. doi: 10.1051/0004-6361:20041088-1.

A. A. van Ballegooijen. Observations and Modeling of a Filament on the Sun. ApJ, 612: 519–529, September 2004. doi: 10.1086/422512.

T. Van Doorsselaere, J. Andries, S. Poedts, and M. Goossens. Damping of Coronal Loop Oscillations: Calculation of Resonantly Damped Kink Oscillations of One-dimensional Nonuniform Loops. ApJ, 606:1223–1232, May 2004. doi: 10.1086/383191.

T. Van Doorsselaere, A. De Groof, J. Zender, D. Berghmans, and M. Goossens. LYRA Observations of Two Oscillation Modes in a Single Flare. ApJ, 740:90, October 2011. doi: 10.1088/0004-637X/740/2/90.

S. Vasheghani Farahani, C. Hornsey, T. Van Doorsselaere, and M. Goossens. Frequency and Damping Rate of Fast Sausage Waves. ApJ, 781:92, February 2014. doi: 10.1088/0004-637X/781/2/92.

A. Veronig, M. Temmer, A. Hanslmeier, W. Otruba, and M. Messerotti. Temporal aspects and frequency distributions of solar soft X-ray flares. A&A, 382:1070–1080, February 2002. doi: 10.1051/0004-6361:20011694.

E. Verwichte, V. M. Nakariakov, and F. C. Cooper. Transverse waves in a post-flare supra-arcade. A&A, 430:L65–L68, January 2005. doi: 10.1051/0004-6361:200400133.

E. Verwichte, C. Foullon, and V. M. Nakariakov. Fast magnetoacoustic waves in curved coronal loops. II. Tunneling modes. A&A, 449:769–779, April 2006. doi: 10.1051/0004-6361:20054398.

J. F. Vesecky, S. K. Antiochos, and J. H. Underwood. Numerical modeling of quasi-static coronal loops. I - Uniform energy input. ApJ, 233:987–997, November 1979. doi: 10.1086/157462.

R. W. Walsh and J. Ireland. The heating of the solar corona. A&A Rev., 12:1–41, 2003. doi: 10.1007/s00159-003-0021-9.

M. S. Wheatland, P. A. Sturrock, and G. Roumeliotis. An Optimization Approach to Reconstructing Force-free Fields. ApJ, 540:1150–1155, September 2000. doi: 10.1086/309355.

R. S. White, E. Verwichte, and C. Foullon. First observation of a transverse vertical oscillation during the formation of a hot post-flare loop. A&A, 545:A129, September 2012. doi: 10.1051/0004-6361/201219856.

T. Wiegelmann. Optimization code with weighting function for the reconstruction of coronal magnetic fields. Sol. Phys., 219:87–108, January 2004. doi: 10.1023/B:SOLA.0000021799.39465.36.

T. Wiegelmann and B. Inhester. How to deal with measurement errors and lacking data in nonlinear force-free coronal magnetic field modelling? A&A, 516:A107, June 2010. doi: 10.1051/0004-6361/201014391.

T. Wiegelmann, B. Inhester, and T. Sakurai. Preprocessing of Vector Magnetograph Data for a Nonlinear Force-Free Magnetic Field Reconstruction. Sol. Phys., 233:215–232, February 2006. doi: 10.1007/s11207-006-2092-z.

T. Wiegelmann, J. K. Thalmann, B. Inhester, T. Tadesse, X. Sun, and J. T. Hoeksema. How Should One Optimize Nonlinear Force-Free Coronal Magnetic Field Extrapolations from SDO/HMI Vector Magnetograms? Sol. Phys., 281:37–51, November 2012. doi: 10.1007/s11207-012-9966-z.

A. R. Winebarger, H. P. Warren, and J. T. Mariska. Transition Region and Coronal Explorer and Soft X-Ray Telescope Active Region Loop Observations: Comparisons with Static Solutions of the Hydrodynamic Equations. ApJ, 587:439–449, April 2003. doi: 10.1086/368017.

G. L. Withbroe and R. W. Noyes. Mass and energy flow in the solar chromosphere and corona. ARA&A, 15:363–387, 1977. doi: 10.1146/annurev.aa.15.090177.002051.

S. Yashiro, S. Akiyama, N. Gopalswamy, and R. A. Howard. Different Power-Law Indices in the Frequency Distributions of Flares with and without Coronal Mass Ejections. ApJ, 650:L143–L146, October 2006. doi: 10.1086/508876.

V. V. Zaitsev and A. V. Stepanov. On the origin of fast drift absorption bursts. A&A, 45: 135–140, December 1975.

V. V. Zaitsev and A. V. Stepanov. On the Origin of the Hard X-Ray Pulsations during Solar Flares. *Soviet Astronomy Letters*, 8:132–134, April 1982.